Green's Function Analysis of Bunched Charged Particle Beams

by

Mark H. Hess

BS, Physics & Mathematics (1997)

University of Maryland at College Park

Submitted to the Department of Physics in Partial Fulfillment
of the Requirements for the degree of Doctor of Philosophy
in Physics at the Massachusetts Institute of Technology
June 2002

Signature of Author .....

Mark H. Hess
Department of Physics
May 17, 2002

Certified by .....

Richard Temkin
Senior Research Scientist, Department of Physics
Thesis Supervisor

Certified by ....

Chiping Chen
Principal Research Scientist, MIT Plasma Science and Fusion Center
Thesis Supervisor

Accepted by .....

Thomas J. Greytak
Chairman, Department Committee on Graduate Students

Green's Function Analysis of Bunched Charged Particle Beams

by

Mark H. Hess

Submitted to the Department of Physics
on May 17, 2002, in Partial Fulfillment of the
Requirements for the Degree of Doctor of Philosophy in
Physics

Abstract

In this thesis, we analyze the dynamics and equilibrium of bunched charged particle beams in the presence of perfectly conducting walls using a Green's function technique. Exact self-consistent electric and magnetic fields are obtained for charged particles in the vicinity of a conducting boundary with the use of Green's functions. We present three analytical models of bunched beams in a cylindrical conducting pipe which employ Green's functions, the Non-Relativistic Center-of-Mass (NRCM) model, the Relativistic Center-of-Mass (RCM) model, and the Relativistic Bunched Disk Beam (RBDB) model.

The NRCM model assumes that the bunches are periodic and represented as point charges propagating non-relativistically in the presence of a constant magnetic focusing field. We derive a maximum limit on the effective self-field parameter $2\omega_p^2/\omega_c^2$ necessary for confining the bunched beam, where ω_p is the effective plasma frequency and ω_c is the cyclotron frequency.

The RCM model extends the analysis of the NRCM model to incorporate relativistic motion of the bunches in the presence of a periodic solenoidal focusing field. We derive a maximum limit on $2\omega_p^2/\omega_{c,rms}^2$ for confinement, where $\omega_{c,rms}$ is the root-mean-square cyclotron frequency. We demonstrate how the self-field parameter limit can be used to predict a current limit in Periodic Permanent Magnet (PPM) klystrons. The 75 MW-XP PPM 11.4 GHz klystron designed by SLAC is found to be operating above this current limit, which may explain the observance of non-negligible beam loss in this experiment.

We model bunches with zero longitudinal thickness and azimuthally symmetric finite transverse distributions in the RBDB model. We derive a limit on $2\omega_p^2/\omega_c^2$, and apply this limit to bunched annular electron beams. The LANL 1.3 GHz relativistic klystron amplifier (RKA), a high-power microwave source using bunched annular electron beams, is found to be operating slightly above this limit, which may explain the observance of beam loss and anomalous beam halo formation.

Finally, we present preliminary results of a Green's function based code called PFB3D, which simulates the dynamics of bunched charged particle beams in a cylindrical conducting pipe. We utilize this code to simulate the dynamics of the LANL 1.3 GHz RKA experiment.

Thesis Supervisor: Richard Temkin
Title: Senior Research Scientist, Department of Physics

Thesis Supervisor: Chiping Chen
Title: Principal Research Scientist, MIT Plasma Science and Fusion Center

Acknowledgements

I am most grateful to my thesis advisors, Dr. Chiping Chen and Dr. Richard Temkin, for giving me the opportunity to be a part of the MIT experience. The have been wonderfully supportive of my work, and inspired, challenged, and polished my skills necessary for being a successful physicist. I would also like to thank them, as well as, Professor Miklos Porkolab and Professor Bruno Coppi for reading this thesis and providing helpful suggestions in improving its presentation.

I am also thankful to all of the other great people that I have worked with at MIT, such as James Anderson, Ronak Bhatt, Dr. Winthrop Brown, Professor John Davies, Dr. Douglas Denison, Professor Yoel Fink, Melissa Hornstein, Steve Korbly, Jagadishwar Sirigiri, Evgenya Smirnova, and Jing Zhou. I shared a lot of laughs, as well as, interesting physics discussions with all of them.

I wish to thank all of my friends and family for their love and support. I would especially, like to thank my best friends Adam Kane, Michael Watts, and Gregory Krasowski, for their wonderful friendship, since as long as I've known them. My sister Michelle deserves many thanks for all the love, support, and great times she has provided me over the many years.

Finally, none of my accomplishments throughout my entire life would have possible without the help of my parents. Aside from their unconditional love and support, they provided me the opportunities with which I fulfilled my dreams.

Contents

List of Figures

List of Tables

Chapter 1

Introduction

Charged particle beams, composed of electrons or ions, have numerous applications in modern science, technology, and medicine. Both ion and electron particle beams are accelerated to extremely high-energies in modern particle accelerators to test the fundamental laws of particle physics. Electrons have been accelerated to 10's GeV in linear colliders, and there are currently designs for advanced linear colliders capable of 100's GeV- 1 TeV energies (see, for example, Brinkmann, 1999; Raubenheimer, 1999). Ions have already been accelerated to energies of 100's GeV- 1 TeV (see, for example Holmes, 1999), and there accelerator designs which could increase the energy to well-beyond 10's TeV-100 TeV (see, for example, Evans, 1999; Dugan, 1999). Electron beams are used in many different types of high-power microwave (HPM) sources, such as klystrons (see, for example, Sprehn *et al.*, 2000; Fazio *et al.*, 1994; Gilmour, 1986, Chap. 9), traveling-wave tubes (TWTs) (see, for example, Wang *et al*, 1999; Shiffler *et al*, 1991; Pierce, 1950, Chap. 2), and free-electron lasers (FELs) (see, for example, Douglas, *et al.* 2001; Neil, *et al.*, 2000; Roberson and Sprangle, 1989), to produce radiation well-into the gigawatt regime in power and UV regime in wavelength. Heavy-ion beams are currently being pursued as a potential driver for inertial confinement fusion (see, for example, Chacon-Golcher, Baca, and Kwan, 2002; Liu, *et al.*, 1998). Electron and ion beams have many industrial applications such as, charged particle beam lithography (see, for example, Kaesmaier and Loschner, 2000; Pfeiffer, 2000) and ion implantation (see. for example, Nastasi, Moller, and Ensinger, 2000; Dearnaley, 1988). They also have wide applications in medicine, such as ion cyclotrons and synchrotrons for radiotherapy (see, for example, Haberer, 2001; Brahme and Lind, 2001).

1.1 Bunched Particle Beams

The first two applications that we just mentioned, namely high-energy accelerators and HPM sources, typically use a special type of beam called a bunched beam. In an unbunched beam, the density of charged particles is slowly varying along the direction of beam propagation, and the flow of the particles is approximately laminar (smooth). In a bunched beam, however, the density of charged particles may very rapidly, i.e. some parts of the beam have *high* densities, while other parts of the beam will have very *low* densities. The regions of the beam with high densities are referred to as *beam bunches.*

In high-energy accelerators, charged particle beams can be accelerated in a series of radio-frequency (rf) cavities using transverse-magnetic (TM) modes (see, for example Humphries, 1986, Chap. 14; Livingston and Blewett, 1962). Figure 1-1 shows a schematic of an accelerating structure with a TM mode present. The circles represent bunches of electrons moving to the right, and the arrows in each cavity denote the direction of E_z. To be more specific, Figure 1-1 shows the accelerating structure operating in π-mode, where the electric fields in adjacent cavities are in opposite phase. The phase velocity of the TM mode is chosen to equal the velocity of the bunch. Therefore, the beam is continually accelerated as it passes through each cavity. We note that if the beam in Fig. 1-1 is unbunched instead of bunched, then half of the particles will see an E_z, that is pointing in the wrong direction. Hence, there would be no net acceleration in accelerating structure.

High-power microwave sources use bunched beams to convert kinetic beam energy into high-power radiation (see, for example, Gold and Nusinovich, 1997; Benford and Swegle, 1992). Figure 1-2 shows a schematic of a relativistic klystron amplifier (RKA), which is an example of a HPM source. The RKA is capable of amplifying an input signal by several orders of magnitude. In the RKA, an unbunched electron beam, traveling with velocity $v_{z0}\hat{\mathbf{e}}_z$ passes through a cavity, which is connected to a radio-frequency input source.

If the cavity is operating in a TM mode, then the unbunched beam will experience a time-varying $E_z = E_{z0}\cos(\omega t)$, where E_{z0} is the maximum electric field and ω is the angular frequency of oscillation. For small E_{z0} and ω, the oscillating electric force

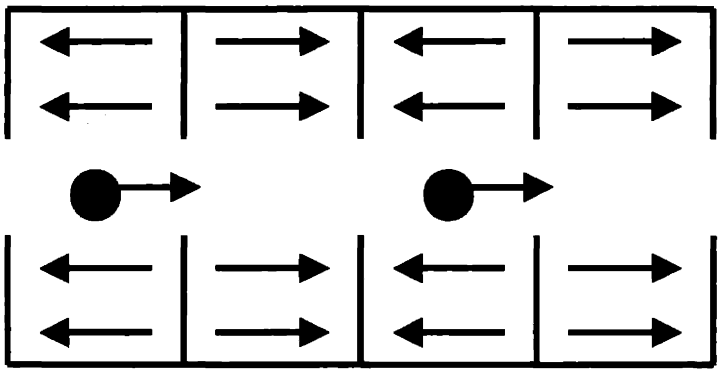

Figure 1-1: Schematic of an accelerating structure operating in π-mode. The arrows inside of each cavity represent the direction of E_z, and the circles represent bunches of electrons being accelerated to the right.

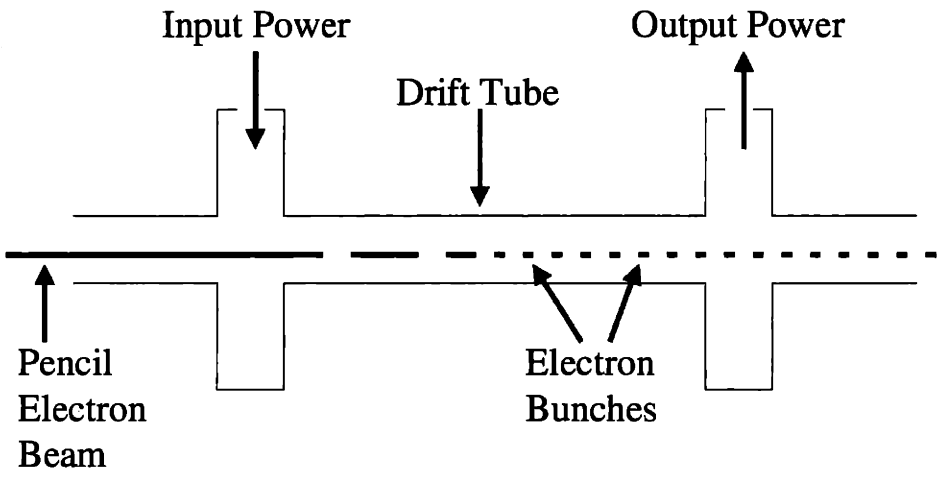

Figure 1-2: Schematic of a klystron amplifier, which shows an unbunched pencil thin electron beam interacting with an input cavity and forming electron bunches in a drift tube. The bunches then excite the output cavity, and generate radiation.

causes the beam to become velocity modulated, that is $v_z(t) = v_{z0} + v_{z1}\cos(\omega t)$, at the exit of cavity, where v_{z1} is the velocity perturbation. The beam will continue to transport through a long drift section, which typically has magnetic focusing, $\mathbf{B}$. The velocity modulation at the input cavity, will translate into a density modulation at the end of the drift section, $n(t) = n_0 + n_1\cos(\omega t)$, where n_0 is the unbunched beam density and n_1 is the density perturbation. The density modulated or "bunched" beam passes through and excites an output cavity with radiation power, P, that scales as $P \sim (\gamma_0 - 1)(\gamma_0^2 - 1)^{1/2}$ (Humphries, Jr., 1990, Chap. 15), where $\gamma_0 = 1/\sqrt{1 - v_{z0}^2/c^2}$.

In both HPM source and high-energy accelerators, the bunched beam will typically be transported near the vicinity of a conducting surface. An example of this surface in accelerators would be the accelerating structure shown in Fig. 1-1 and the drift section of the klystron in Figure 1-2, and for HPMs it would be the drift tube. When charged particles are near a conductor they induce surface charge on the conductor, which causes an attraction between it and the charge. Taking into account this effect is important for understanding the physics of the beam transport, and important for the performance of the accelerator or HPM source.

1.2 Existing Theory of Intense Bunched Beams

There has been much progress pertaining to the physics of unbunched beams, such as the theory of beam transport in focusing fields (Davidson, 1990; Reiser, 1994), the physics beam equilibrium and stability, and the physics of beam halo formation (Pakter and Chen, 2000; Chen and Pakter, 1999 and 2000). Unbunched beams are much simpler to model than bunched beams, since the longitudinal density variation of unbunched beams can typically be ignored. Due to the higher level of complexity, the theory of bunched beams has seen little attention.

The majority of papers written on the analytical theory of bunched beams make the assumption that the density of the bunch is given by a prescribed function. For example, in an early work by Sacherer (Sacherer, 1971), an rms envelope equation was derived for unbunched beams, and then generalized to bunched beams. The bunched beam density

was assumed to be ellipsoidal in nature, i.e. $n = n\left(x^2/a^2 + y^2/b^2 + z^2/c^2\right)$, where n is the beam density, and a, b, and c are characterisitic lengths defining the beam bunch. This ellipsoidal bunched beam density distribution was also employed in a paper by Barnard and Lund (Barnard and Lund, 1997), to compute the effect of longitudinal beam-halo formation. In a later article by Gluckstern *et al.* (Gluckstern *et al.*, 1998), 3-D halo formation was studied for bunched beams assuming the density distribution was spheroidal, $n = n\left(x^2/a^2 + y^2/a^2 + z^2/c^2\right)$.

We should also note that all of the bunched beam calculations that were just referenced, were performed for on beam bunches in free space (no conductor present). A small subset of papers on bunched beams include the effect of a nearby conducting wall. One such paper is by Allen and Reiser (Allen and Reiser, 1997), which generalizes the rms bunched beam envelope equation calculated by Sacherer for the case of an spheroidal bunch distribution in a perfectly conducting cylindrical pipe. They utilize a Green's function technique, as is done in this thesis, to self-consistently calculate the electric fields within the beam. However, in this paper they make a simplifying assumption that the beam bunch is centered on the pipe axis. This assumption dramatically simplifies the electric field calculations, since only azimuthally invariant components of the field need to be computed.

1.3 Main Contributions of the Thesis

This thesis will present various models of periodic bunched particle beams, both analytical and numerical, in the presence of conducting walls. All of these models will be related by the fact that they utilize a Green's function technique to self-consistently compute the electric fields.

Unlike the previous works just mentioned, we will present two models, the Non-Relativistic Center of Mass (NRCM) model and the Relativistic Center of Mass (RCM), which assume that the bunched beam is positioned off-axis from the center of a perfectly conducting pipe. Both models assume that the periodic bunches can be modeled as point charges, and a magnetic focusing field (constant for the NRCM model and periodic solenoidal for the RCM model) is assumed to be present to stabilize the beam bunch from the attractive beam-wall interaction. The assumption of off-axis beam propagation

allows us to derive a new fundamental bunched beam confinement criterion for each model. In Chapter 5, we will see how the confinement criterion derived for the RCM model can be applicable in predicting limits for the Periodic Permanent Magnet (PPM) klystrons at the Stanford Linear Accelerator Center (SLAC) (Sprehn, *et al.*, 1997; Sprehn, *et al.*, 2000; Scheitrum, 2000; Scheitrum *et al.*, 2000).

We will also present a periodic bunched beam model with an extended transverse charge distribution in cylindrical conducting pipe called the Relativistic Bunched Disk Beam (RBDB) model. This model assumes that the bunches are azimuthally symmetric and have zero longitudinal thickness, but arbitrary transverse density. We include uniform magnetic focusing, in order to provide a force balance against the self-consistent electric field inside of the bunch. A bunched beam equilibrium criterion on the minimum magnetic field necessary is derived for the RBDB model.

Within the RBDB model, we can analyze the properties of bunched annular beams, which have been used in numerous high-power microwave sources, such as relativistic klystron amplifiers (RKA). In Chapter 7, we demonstrate how to apply the equilibrium criterion to high-power bunched annular beam experiments, such as the 1.3 GHz RKA experiment at the Los Alamos National Laboratory (Fazio, *et al.*, 1994). To the best of our knowledge, this is the first self-consistent bunched annular beam analysis ever conducted.

Finally, we present preliminary results for the PFB3D (Periodic Focused Beam in 3-D) code, which uses Green's function techniques to simulate bunched beams of arbitrary shape that are propagating off-axis inside of a perfectly conducting pipe with periodic magnetic focusing present. The PFB3D code offers a general method for investigating the properties of bunched particle beams in a self-consistent manner.

1.4 Outline of the Thesis

In Chapter 2, we will discuss how to calculate the electric field due to an arbitrary distribution of charge in the presence of a perfect conductor of arbitrary shape using an electrostatic Green's function. At the end of Chapter 2, we specialize the Green's function technique to the case of a cylindrical conductor. The rest of the thesis focuses

on bunched beam models in the presence of a cylindrical conducting pipe, and makes use of the Green's function technique described in Chapter 2.

In Chapter 3, we present the Non-Relativistic Center of Mass (NRCM) model. The NRCM model assumes that the beam is periodically bunched in a cylindrical pipe, and each bunch can be represented as a point charge that is offset from the pipe axis. In the NRCM model, we will derive a fundamental bunched beam confinement criterion for the minimum magnetic field necessary to prevent the beam from being lost to the wall.

Chapter 4 discusses the Relativistic Center of Mass (RCM) model, which is a relativistic generalization of the NRCM model. We also generalize the magnetic field to be a periodic focusing field. A more generalized confinement criterion is derived for the RCM model.

In Chapter 5, we show how to apply the confinement criterion in the RCM model to model three Periodic Permanent Magnet (PPM) Klystrons developed at Stanford Linear Accelerator Center (SLAC), namely 50 MW XL-PPM (Sprehn, *et al.*, 1997; Sprehn, *et al.*, 2000), 75 MW XP (Sprehn, *et al.*, 1997; Sprehn, *et al.*, 2000), and the Klystrino (Scheitrum, 2000; Scheitrum *et al.*, 2000). An important result from Chapter 5 is that one of the three klystrons, 75 MW XP is operating of above the RCM confinement criterion. This is consistent with the observed beam loss in this device (Sprehn, *et al.*, 1997; Sprehn, *et al.*, 2000).

Chapter 6 gives a presentation of the Relativistic Bunched Disk Beam (RBDB) model. This model assumes that the bunches are azimuthally symmetric and have zero longitudinal thickness, but arbitrary transverse density. A uniform magnetic focusing field is present, to maintain force equilibrium with the self-consistent electric field inside of the bunch. We derive a criterion for bunched beam equilibrium to exist within the RBDB model.

In Chapter 7, we apply the bunched beam equilibrium criterion from the RBDB model to three annular high-power microwave experiments, the 1.3 GHz RKA experiment at Los Alamos National Laboratory, 1.3 GHz relativistic klystron oscillator (RKO) at the Air force Research Laboratory (Hendricks, *et al.*, 1998), and the 9.4 GHz backward wave oscillator at the University of New Mexico (Hegeler, *et al.*, 1998).

In Chapter 8, we show the development of an electrostatic Green's function based simulation code called PFB3D (Periodic Focused Beam in 3-D). The code is capable of self-consistently simulating macroparticle dynamics in the presence of a conducting cylinder and a magnetic focusing field.

Lastly, in Chapter 9 we will provide a discussion of the results presented in the thesis along with plans for future work.

Chapter 2

Description of Electrostatic Green's Function Technique

Typically, the electric fields for continuous charged particle beams may be calculated using simple symmetry properties combined with Maxwell's equations. These calculations, in general, are considerably more difficult when the beam becomes bunched and realistic boundary conditions are included; hence, simple techniques will not apply. The Green's function technique, which we will utilize throughout this entire thesis, is an exact method for calculating electrostatic fields due to any beam distribution, including bunched beams. In this Chapter, we describe the Green's function technique analytically. We will start with the general formulation of a three-dimensional electrostatic Green's function for an arbitrary conductor boundary. Since cylindrical conductors are the most widely used boundary in beam devices, we will calculate the Green's function for the special case of a cylindrical conductor wall.

2.1 General Formulation of a 3D Electrostatic Green's Function

Our Green's function formulation begins with the assumption that there are N point charges, each with charge, q, at rest in the vicinity of a perfectly conducting surface, S. The position of the i^{th} charge will be denoted by the vector $\mathbf{x}_i'$, and the index i is in the range $1 \le i \le N$. Our final goal is to calculate the electric field, $\mathbf{E}$, at a position $\mathbf{x}$ due to the point charges, including the effect of the nearby conductor. The Green's function technique, as we will now demonstrate, is an exact procedure for calculating $\mathbf{E}$.

We know that $\mathbf{E}$ may be calculated from Maxwell's equations by,

$$\nabla \cdot \mathbf{E} = 4\pi\rho, \tag{2.1}$$

where $\rho = q\sum_{i=1}^{N} \delta(\mathbf{x} - \mathbf{x}_i')$ is the total charge density, and $\delta(\mathbf{x})$ is the Dirac delta function. We also know from Maxwell's equations that

$$\nabla \times \mathbf{E} = -\frac{1}{c}\frac{\partial \mathbf{B}}{\partial t}, \tag{2.2}$$

where $\mathbf{B}$ is the magnetic field, and c is the speed of light in vacuum. However, since the charge is at rest with respect to the conductor, the system is completely time-independent. Hence, $\nabla \times \mathbf{E} = 0$, which implies that

$$\mathbf{E} = -\nabla\phi, \tag{2.3}$$

where ϕ is the electrostatic potential. Therefore, calculating ϕ is equivalent to calculating $\mathbf{E}$. At the end of this Chapter, we will discuss the effect of how the solution in (2.3) would be corrected for charges that are moving with velocities much smaller than c near the conductor. This effect is important, since the particles inside of a beam are never completely at rest with respect to the conductor. Plugging ϕ back into Eq. (2.1) yields the familiar result

$$\nabla^2\phi = -4\pi\rho = -4\pi q\sum_{i=1}^{N} \delta(\mathbf{x} - \mathbf{x}_i'). \tag{2.4a}$$

The solution of Eq. (2.4a) can only be obtained when boundary conditions are specified. In this system, the boundary surface is assumed to be perfectly conducting. Physically, this implies that the electric field inside of the conductor is precisely zero. In other words, the potential is a constant

$$\phi(\mathbf{x}) = \phi_0 \tag{2.4b}$$

inside of the conductor and at its boundary. Without loss of generality, we may assume that $\phi_0 = 0$ (Dirichlet Condition), since this is equivalent to shifting ϕ by a constant and does not affect $\mathbf{E}$.

A method for calculating ϕ in Eq. (2.4a) with the appropriate boundary conditions in Eq. (2.4b) is by using an electrostatic Green's function. Specifically, the electrostatic Green's function, $G(\mathbf{x};\mathbf{x}')$, in three dimensions is defined by the following equations

$$\nabla^2 G(\mathbf{x};\mathbf{x}') = -4\pi\delta(\mathbf{x}-\mathbf{x}'), \tag{2.5a}$$

$$G\big|_S = 0. \tag{2.5b}$$

For our system of N point charges, we immediately see that ϕ is given by the formula,

$$\phi = q\sum_{i=1}^{N} G(\mathbf{x};\mathbf{x}_i'). \tag{2.6}$$

For a general distribution of charges, discrete or continuous, i.e. $\rho = \rho(\mathbf{x}')$, Eq. (2.6) is modified to the following expression,

$$\phi = \int d^3x'\rho(\mathbf{x}')G(\mathbf{x};\mathbf{x}'). \tag{2.7}$$

One of the powerful aspects of the Green's function, as illustrated in Eqs. (2.6) and (2.7), is that it is independent of the charge distribution within the system. This property is especially useful for analyzing charged particle beams, which may come in a large variety of distribution types. In Chapter 3, 4, 5, and 8, we will make use of Eq. (2.6) when simulating a bunched beam with a finite number of macroparticles. In Chapter 6 and 7, we will model bunched continuous distributions, and use Eq. (2.7).

2.2 Methods for Solving the Green's Function

2.2.1 Eigenfunction Expansion Method

One technique for solving Eqs. (2.5a) and (2.5b) is the eigenfunction expansion method (see for example, Jackson, 1975, pp. 119-120). Essentially, the method converts the problem of solving an inhomogeneous Poisson equation into a homogeneous Helmholtz equation. There are known numerical methods for solving Helmholtz's equation with arbitrary boundary shapes, one of which is the Finite Element Method (FEM). An extensive theoretical discussion of the FEM and its' application to linear partial differential equations, including the Helmholtz equation is given by Schwarz (1988, Ch. 1-3).

We begin by finding eigenfunction solutions to the Helmholtz equation with the same boundary conditions applied to $G(\mathbf{x};\mathbf{x}')$, i.e.,

$$(\nabla^2 + \lambda_n)H_n(\mathbf{x}) = 0 \tag{2.8a}$$

$$H_n(\mathbf{x})\big|_S = 0, \tag{2.8b}$$

where $H_n(\mathbf{x})$ is the n^{th} eigenfunction with eigenvalue λ_n. It is assumed that the set of eigenfunctions form a complete set. Using well-known Green's Theorem,

$$\int d^3x\left(\chi\nabla^2\psi - \psi\nabla^2\chi\right) = \int dS\hat{\mathbf{n}}\cdot\left(\chi\nabla\psi - \psi\nabla\chi\right) \tag{2.9}$$

with $\chi = H_m^*(x)$ and $\psi = H_n(\mathbf{x})$, we can immediately conclude that the eigenvalues λ_n are real numbers, and, with proper normalization, $H_n(\mathbf{x})$ are a set of orthonormal functions, that is

$$\int d^3x H_m^*(\mathbf{x})H_n(\mathbf{x}) = \delta_{mn}\,, \tag{2.10}$$

where δ_{mn} is the Kronecker delta function.

Since the set of $\{H_n(\mathbf{x})\}$ is complete, and they each satisfy the same boundary condition as that for $G(\mathbf{x};\mathbf{x}')$, we can form the following expansion,

$$G(\mathbf{x};\mathbf{x}') = \sum_n g_n(\mathbf{x}')H_n(\mathbf{x}). \tag{2.11}$$

The coefficients $g_n(\mathbf{x}')$ are immediately determined by combining the orthonormality condition of Eq. (2.10) with the Green's function definition in Eq. (2.5a), i.e.,

$$g_n(\mathbf{x}') = -\frac{4\pi H_n(\mathbf{x}')}{\lambda_n}. \tag{2.12}$$

Therefore, the Green's function may be written as

$$G(\mathbf{x};\mathbf{x}') = -4\pi\sum_n \frac{H_n(\mathbf{x}')H_n(\mathbf{x})}{\lambda_n}. \tag{2.13}$$

The eigenfunction expansion method can be used to solve for $H_n(\mathbf{x})$ and $G(\mathbf{x};\mathbf{x}')$ explicitly in simple geometries, such as rectangles, circles, etc. In more complicated geometries, however Eqs. (2.8a) and (2.8b) must be solved numerically using a technique, such as FEM (Schwarz, 1988, Chs. 1-3).

2.2.2 Coordinate Expansion Method

When the conducting surface possesses, a high-degree of symmetry, e.g., cylindrical or spherical symmetry, the coordinate expansion method can be a very powerful tool for

calculating $G(\mathbf{x};\mathbf{x}')$ (see for example, Jackson 1975, pp. 116-118; Arfken and Weber, 1995 pp. 516-519). As we will illustrate, the coordinate expansion method assumes that the Green's function can be calculated through a separation of variables. The problem of solving the three-dimensional equation in Eq. (2.5) is then reduced to a lower dimensional problem.

We begin the coordinate expansion method by writing the delta function, $\delta(\mathbf{x}-\mathbf{x}')$, in its relevant coordinate system. For our special case of cylindrical coordinates, we know that

$$\delta(\mathbf{x}-\mathbf{x}')=\frac{1}{r}\delta(r-r')\delta(\theta-\theta')\delta(z-z'). \tag{2.14}$$

We now can transform angular and longitudinal parts of Eq. (2.14) into more useable functions. From the well-known Fourier series and transform identities (Arfken and Weber, 1995 pp. 827 and 858), $\delta(\theta-\theta')=\frac{1}{2\pi}\sum_{l=-\infty}^{\infty}e^{il(\theta-\theta')}$ and $\delta(z-z')=\frac{1}{2\pi}\int_{-\infty}^{\infty}d\lambda e^{i\lambda(z-z')}$, we can rewrite (2.14) as

$$\delta(\mathbf{x}-\mathbf{x}')=\frac{1}{4\pi^2 r}\delta(r-r')\sum_{l=-\infty}^{\infty}e^{il(\theta-\theta')}\int_{-\infty}^{\infty}d\lambda e^{i\lambda(z-z')}. \tag{2.15}$$

As a side note, for the case of spherical symmetry, the angular parts of $\delta(\mathbf{x}-\mathbf{x}')$ can be expanded in terms of the spherical harmonics.

If we choose the following form for $G(\mathbf{x};\mathbf{x}')$,

$$G(\mathbf{x};\mathbf{x}')=\frac{1}{4\pi^2}\sum_{l=-\infty}^{\infty}e^{il(\theta-\theta')}\int_{-\infty}^{\infty}d\lambda e^{i\lambda(z-z')}h_l(\lambda;r;r'), \tag{2.16}$$

then we obtain the following radial differential equation for h_l:

$$r\frac{d}{dr}\left(r\frac{dh_l}{dr}\right)-\left(l^2+\lambda^2r^2\right)h_l=-4\pi r\delta(r-r'). \tag{2.17}$$

Assuming that is possible to solve Eq. (2.17) with the appropriate Dirichlet boundary conditions, then we can reduce the three-dimensional Green's function problem into a one-dimensional problem. In the next section, we will solve Eq. (2.17) for a cylindrical conductor boundary. However, Eq. (2.17) could also be solved for other cylindrical systems such as a coaxial cylindrical geometry.

2.3 Green's Function for a Cylindrical Conductor

In Section 2.2, we discussed two methods for solving for the Green's function, the eigenfunction expansion method and the coordinate expansion. We now use the coordinate expansion formalism developed in Section 2.2.2 to derive $G(\mathbf{x};\mathbf{x}')$ for a cylindrical conductor boundary.

To solve Eq. (2.17) with the Dirichlet boundary condition at the conductor, let a denote the radius of the conductor. Then the boundary condition on Eq. (2.17) is

$$h_l(\lambda;a;r')=0. \tag{2.18}$$

The solution to the homogeneous part of Eq. (2.17) is given by $I_l(\lambda r)$ and $K_l(\lambda r)$, which are the l^{th} order modified Bessel functions of the first and second kind, respectively. Hence, we can construct a solution to Eq. (2.17) with linear combinations of $I_l(\lambda r)$ and $K_l(\lambda r)$. However, in order to handle the Delta function inhomogeneity in Eq. (2.17), we must require that $h_l(\lambda;r;r')$ is continuous, but not differentiable at $r=r'$. Therefore, we see that

$$h_l(\lambda;r;r')=\begin{cases} A_l I_l(\lambda r)+B_l K_l(\lambda r) & , \quad r\geq r', \\ C_l I_l(\lambda r)+D_l K_l(\lambda r) & , \quad r<r', \end{cases} \tag{2.19}$$

where A_l, B_l, C_l, and D_l are constants which we will now determine. Since, $K_l(\lambda r)$ diverges as $r\to 0$, we must require that $D_l=0$, in order to have physically relevant solutions. By enforcing Eq. (2.18), along with the continuity requirement, Eq. (2.19) simplifies to

$$h_l(\lambda;r;r')=\begin{cases} B_l\left[K_l(\lambda r)-\dfrac{I_l(\lambda r)K_l(\lambda a)}{I_l(\lambda a)}\right] & , \quad r\geq r', \\ B_l\left[K_l(\lambda r')-\dfrac{I_l(\lambda r')K_l(\lambda a)}{I_l(\lambda a)}\right]\dfrac{I_l(\lambda r)}{I_l(\lambda r')} & , \quad r'<r'. \end{cases} \tag{2.20}$$

The final solution is obtained by infinitesimally integrating both sides of Eq. (2.17) over r with the integration limits centered around r', in other words by taking the limit, $\lim_{\varepsilon\to 0}\int_{r'-\varepsilon}^{r'+\varepsilon} dr$. The second term in Eq. (2.17) will obviously go to zero upon integration.

After integrating by parts twice on the first term of Eq. (2.17) and integrating the right hand side as well, we obtain

$$\lim_{\varepsilon\to 0}\left\{\left[r^2\frac{\partial h_l}{\partial r}-rh_l\right]_{r'-\varepsilon}^{r'+\varepsilon}+\int_{r'-\varepsilon}^{r'+\varepsilon}drh_l\right\}=-4\pi r'. \tag{2.21}$$

The second term and third terms on the left-hand side of Eq. (2.21) go to zero. Combining Eq. (2.20) and Eq. (2.21), and using the Wronskian relation, $K_n(x)I_n'(x)-K_n'(x)I_n(x)=1/x$, we find that

$$h_l(\lambda;r;r')=\frac{4\pi I_l(\lambda r_<)}{I_l(\lambda a)}[I_l(\lambda a)K_l(\lambda r_>)-I_l(\lambda r_>)K_l(\lambda a)] \tag{2.22}$$

where $r_>(r_<)$ denotes the greater(lesser) of r and r'. Therefore, we may write the Green's function for cylinder as

$$G(\mathbf{x};\mathbf{x}')=\frac{1}{\pi}\sum_{l=-\infty}^{\infty}e^{il(\theta-\theta')}\int_{-\infty}^{\infty}d\lambda e^{i\lambda(z-z')}\frac{I_l(\lambda r_<)}{I_l(\lambda a)}[I_l(\lambda a)K_l(\lambda r_>)-I_l(\lambda r_>)K_l(\lambda a)] \tag{2.23}$$

We note that the Green's function in Eq. (2.23) for a cylinder has been previously derived in a variety of ways. For example, an analysis by Gray and Mathews (1952, Ch. 9) utilizes extensive properties of Bessel functions, originally developed by Dougall (Dougall, 1900) to calculate Green's functions for a wide range of conductor boundaries.

We can recover the free-space Green's function, $G_{free}(\mathbf{x};\mathbf{x}')$, by taking the limit of the conductor radius going to infinity ($a\to\infty$). Using the asymptotic limits of $I_l(x)$ and $K_l(x)$, we find that the second term in Eq. (2.23) goes to zero. Hence, we obtain

$$G_{free}(\mathbf{x};\mathbf{x}')=\frac{1}{\pi}\sum_{l=-\infty}^{\infty}e^{il(\theta-\theta')}\int_{-\infty}^{\infty}d\lambda e^{i\lambda(z-z')}I_l(\lambda r_<)K_l(\lambda r_>). \tag{2.24}$$

From electrostatics, we know that $G_{free}(\mathbf{x};\mathbf{x}')$ is given by (see for example, Gray and Mathews, 1952, p. 102)

$$G_{free}(\mathbf{x};\mathbf{x}')=\frac{1}{|\mathbf{x}-\mathbf{x}'|}, \tag{2.25}$$

which yields the important relation (Gray and Mathews, 1952, p. 103; Jackson, 1975, p. 118),

$$\frac{1}{|\mathbf{x}-\mathbf{x}'|}=\frac{1}{\pi}\sum_{l=-\infty}^{\infty}e^{il(\theta-\theta')}\int_{-\infty}^{\infty}d\lambda e^{i\lambda(z-z')}I_l(\lambda r_<)K_l(\lambda r_>). \tag{2.26}$$

Now that we have obtained the Green's function for a cylinder, we can use Eq. (2.23) in conjunction with Eqs. (2.6) and (2.7) to derive the electrostatic potential for any charge distribution. As we will see in later chapters, Eq. (2.23) will be an invaluable tool for analyzing bunched charged particle beams. Specifically, in chapter 9, we will show how to numerically simulate bunched beams from Eq. (2.23), and demonstrate how to improve the simulation by implementing the relation in Eq. (2.26).

2.4 Discussion

In Section 2.2, we assumed that the system of charges was at rest with respect to the conductor, in order to justify the electrostatic solution in Eq. (2.3). However, in an actual charged particle beam, the charges will not be completely at rest with respect to the conductor. Rather, the beam will be have a velocity distribution, and therefore, the right-hand side of Eq. (2.2) will not be zero.

Suppose, however, that the i^{th} particle is traveling with a uniform velocity $\mathbf{v}_i'$, such that $|\mathbf{v}_i'| << c$. It is well-known (see for example, Reitz *et al*, 1993, p. 551) that the magnetic field generated from the i^{th} particle is given by

$$\mathbf{B}_i=\frac{\mathbf{v}_i'}{c}\times\mathbf{E}_i, \tag{2.27}$$

where $\mathbf{E}_i$ is the electric field generated by the i^{th} particle. Since, $\mathbf{E}_i=\mathbf{E}_i(\mathbf{r}_i'(t)_i,\mathbf{v}_i')$, and

$$\frac{d\mathbf{r}_i'}{dt}=\mathbf{v}_i', \tag{2.28}$$

then the right-hand side Eq. (2.2) for the i^{th} particle is of the order,

$$\left|\frac{1}{c}\frac{\partial\mathbf{B}_i}{\partial t}\right|=\left|\frac{\mathbf{v}_i'}{c}\times\frac{\partial\mathbf{E}_i}{\partial t}\right|\sim\left|\frac{|\mathbf{v}_i'|^2}{c^2}\mathbf{E}_i\right|. \tag{2.29}$$

Hence, the correction to the electrostatic potential, ϕ, is of the order $|\mathbf{v}_i'|/c$. For a beam velocity distribution, in which the characteristic velocity of the distribution, such as

the thermal velocity, is much smaller than the speed of light, the electrostatic approximation is valid.

Chapter 3

Non-Relativistic Center-of-Mass (NRCM) Model with Uniform Focusing

In typical experiments, a bunched beam may have as many as 10^{10} particles per bunch. Calculating the beam-wall interaction would be an enormous task, if we tried to compute the electric field due to each of the particles in the presence of the conductor wall. The first bunched beam model presented in this text will be a major simplification of the many-particle problem. We refer to this model as the Non-Relativistic Center-of-Mass (NRCM) Model. It is based mainly on a paper by Hess and Chen (2000). In this model, we represent each bunch as a single particle located at the bunch's center-of-mass inside of a perfectly conducting cylinder with a uniform magnetic focusing field. This model, while seemingly simplistic, actually provides a very powerful condition on the self-field parameter of the beam necessary for confinement in the conductor. As we will show, this confinement limit is the bunched beam generalization of the well-known Brillouin density limit for continuous beams (Brillouin, 1945).

3.1 Description of the Model

The system we are analyzing consist of periodic space charge in an infinite perfectly conducting cylinder, which is grounded, as shown in Fig. 3-1(a). In particular, we investigate the dynamics of a collinear periodic distribution of charges, with charge Q, equally spaced by a distance, L. Each of the charges in this model represents an entire bunch in an actual beam. The charge is assumed to be located at the center-of-mass of each bunch. If the beam bunches in a real experiment were tightly bound, than this

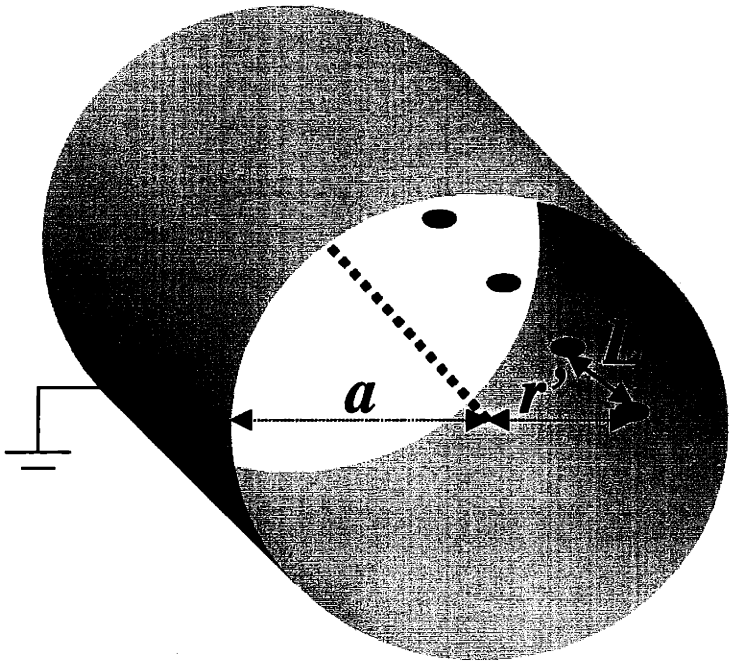

Fig. 3-1(a): Schematic of a periodic array of charges in a perfectly conducting cylinder.

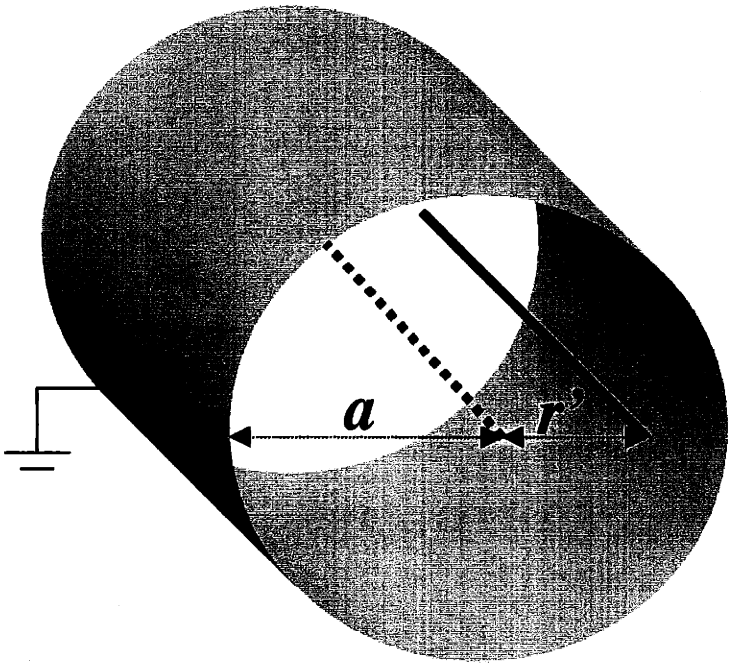

Fig. 3-1(b): Schematic of a line charge in a perfectly conducting cylinder.

model could be a very good approximation to the dynamics of each bunch. The radius of the cylinder is a, and the distance from the axis that the space charge is displaced is r'.

We assume that there exists an applied uniform magnetic field $\mathbf{B} = B\hat{\mathbf{e}}_z$, and $\hat{\mathbf{e}}_z$ denotes the unit vector parallel to the axis of the conductor. The charge density distribution for such a periodic bunched beam is expressed as

$$\rho(\mathbf{x}-\mathbf{x}') = \frac{Q}{r}\delta(r-r')\delta(\theta-\theta')\sum_{n=-\infty}^{\infty}\delta(z-z'-nL), \tag{3.1}$$

which satisfies the longitudinal periodicity property, $\rho(\mathbf{x}-\mathbf{x}') = \rho([\mathbf{x}+L\hat{\mathbf{e}}_z]-\mathbf{x}')$.

In the following analysis, we will compare the dynamics properties of this distribution with those of the 2-D rod distribution shown in Fig. 3-1(b). Physically, the 2-D case is recovered from the 3-D case by taking the limit $a/L \to \infty$ for a fixed line charge density with $\lambda_q = Q/L = \text{constant}$.

The presence of the periodic space charge induces a surface charge density, σ, on the surface of the conductor. The induced surface charge provides an electrostatic force on the space charge inside of the conductor. We assume that the transverse velocity of the space charge is sufficiently small compared to the speed of light, hence only the electrostatic force from the conducting wall and the applied magnetic force are non-negligible in the system.

By utilizing Eqs. (2.7), (2.23), (3.1), and the well-known relation $\sum_{n=-\infty}^{\infty}\delta(x-2\pi n) = \frac{1}{2\pi}\sum_{n=-\infty}^{\infty}e^{inx}$ (Arfken, 1995; p. 827), we can compute immediately the electrostatic potential inside of the conductor. This gives

$$\phi(\vec{r}) = \frac{2Q}{L}\sum_{n=-\infty}^{\infty}\sum_{l=-\infty}^{\infty}e^{in(\hat{z}-\hat{z}')}e^{il(\theta-\theta')}\frac{I_l(n\hat{r}_<)}{I_l(n\alpha)}[I_l(n\alpha)K_l(n\hat{r}_>) - I_l(n\hat{r}_>)K_l(n\alpha)], \tag{3.2}$$

where we have introduced the following normalized coordinates and parameter,

$$\hat{r} = \frac{2\pi r}{L}, \quad \hat{r}' = \frac{2\pi r'}{L}, \quad \hat{z} = \frac{2\pi z}{L}, \quad \hat{z}' = \frac{2\pi z'}{L}, \quad \alpha = \frac{2\pi a}{L}. \tag{3.3}$$

Simplification of the electrostatic potential in Eq. (3.2) is possible by first summing over the terms with $n = 0$, and then combining the terms with $n < 0$ with their positive counterparts yielding,

$$\phi = \frac{Q}{L}G_{2D} + \frac{4Q}{L}\sum_{n=1}^{\infty} cos[n(\hat{z}-\hat{z}')]\frac{I_0(n\hat{r}_<)}{I_0(n\alpha)}[I_0(n\alpha)K_0(n\hat{r}_>) - I_0(n\hat{r}_>)K_0(n\alpha)]$$
$$+\frac{8Q}{L}\sum_{n=1}^{\infty}\sum_{l=1}^{\infty} cos[n(\hat{z}-\hat{z}')]cos[l(\theta-\theta')]\frac{I_l(n\hat{r}_<)}{I_l(n\alpha)}[I_l(n\alpha)K_l(n\hat{r}_>) - I_l(n\hat{r}_>)K_l(n\alpha)], \tag{3.4}$$

where G_{2D} represents the solution of Eqs. (2.5a) and (2.5b) for a 2-D rod distribution [i.e. $\delta(\mathbf{x}-\mathbf{x}') = \frac{1}{r}\delta(r-r')\delta(\theta-\theta')$]. The 2-D Green's function, G_{2D}, is given by

$$G_{2D} = \ln\left[\frac{a^2 + (r_> r_</a)^2 - 2r_< r_> \cos(\theta-\theta')}{r_>^2 + r_<^2 - 2r_< r_> \cos(\theta-\theta')}\right] \tag{3.5}$$

which is well known (see for example, Barton, 1995, pp. 412-416).

Now that we have obtained the electrostatic potential inside of the conductor, we can readily calculate the electric field at the surface of the wall and the induced surface charge density, σ, using the relation

$$\sigma = \frac{\hat{\mathbf{n}}\cdot\mathbf{E}|_{surface}}{4\pi} = \frac{-\hat{\mathbf{n}}\cdot\nabla\phi|_{surface}}{4\pi} = \frac{1}{2L}\frac{\partial\phi}{\partial\hat{r}}\bigg|_{\hat{r}=\alpha}, \tag{3.6}$$

where $\hat{\mathbf{n}} = -\hat{\mathbf{e}}_r$ denotes the unit vector perpendicular to the surface, and $\mathbf{E}$ is the electric field.

For the 2-D case $L \to 0$ and $\lambda_q = Q/L = \text{constant}$, the induced surface charge is given by

$$\sigma_{2D} \equiv -\frac{\lambda_q}{2\pi a}\hat{\sigma}_{2D} = -\frac{\lambda_q}{2\pi a}\left[\frac{a^2 - r'^2}{a^2 + r'^2 - 2ar'\cos(\theta-\theta')}\right] \tag{3.7}$$

while for the 3-D case we have

$$\sigma_{3D} = -\frac{\hat{\sigma}_{2D}}{L^2\alpha} - \frac{2}{L^2\alpha}\sum_{n=1}^{\infty}\cos[n(\hat{z}-\hat{z}')]\frac{I_0(n\hat{r}')}{I_0(n\alpha)}$$
$$-\frac{4}{L^2\alpha}\sum_{n=1}^{\infty}\sum_{l=1}^{\infty}\cos[n(\hat{z}-\hat{z}')]\cos[l(\theta-\theta')]\frac{I_l(n\hat{r}')}{I_l(n\alpha)}. \tag{3.8}$$

In deriving Eq. (3.8) use has been made of the Wronskian $I_l(x)K_l'(x) - I_l'(x)K_l(x) = -1/x$.

We are now in a position to compute the electric field, $\mathbf{E}^{self}$, which is exerted on the charge distribution inside the conductor by the induced surface charge. Because of the

system's symmetry in the $\hat{\mathbf{e}}_\theta$ and $\hat{\mathbf{e}}_z$ directions, the electric field at the charge distribution can only be in the $\hat{\mathbf{e}}_r$ direction. Since the sign of the surface charge is opposite to that of the internal charges, the force must be attractive. The self-electric field $\mathbf{E}^{self}$ can be obtained by integrating the differential electric field vector, evaluated at the charge distribution location, over the entire conductor,

$$\mathbf{E}^{self}(\mathbf{r}') = \oint_{surface} dS \frac{(\mathbf{r}' - \mathbf{r}_s)\sigma(\mathbf{r}_s)}{|\mathbf{r}' - \mathbf{r}_s|^3}. \tag{3.9}$$

where $\mathbf{r}_s$ is the vector measured from the central axis of the conductor to the point of the differential charge. As will be demonstrated in Appendix A,

$$\mathbf{E}_{2D}^{self}(\mathbf{r}') = 2\lambda_q \left(\frac{r'}{a^2 - r'^2} \right) \hat{\mathbf{e}}_r \tag{3.10}$$

for the 2-D case, and $\mathbf{E}_{3D}^{self}(\mathbf{r}') = E_{3D}^{self} \hat{\mathbf{e}}_r$,

$$\begin{aligned} E_{3D}^{self} = & \frac{4\pi Q}{L^2} \left(\frac{\hat{r}'}{\alpha^2 - \hat{r}'^2} \right) + \frac{8\pi Q}{L^2} \sum_{n=1}^{\infty} \frac{n I_0(n\hat{r}') I_0'(n\hat{r}') K_0(n\alpha)}{I_0(n\alpha)} \\ & + \frac{16\pi Q}{L^2} \sum_{n=1}^{\infty} \sum_{l=1}^{\infty} \frac{n I_l(n\hat{r}') I_l'(n\hat{r}') K_l(n\alpha)}{I_l(n\alpha)} \end{aligned} \tag{3.11}$$

for the 3-D system.

Figure 3-2 shows a plot of $E_{3D}^{self}\left(4\pi Q/L^2\right)^{-1}$ (dashed line) versus r/a for $\alpha = 1.0$. As a comparison, we also plot the first term of $E_{3D}^{self}\left(4\pi Q/L^2\right)^{-1}$ (solid line), that is the 2-D unbunched term $\hat{r}/\left(\alpha^2 - \hat{r}^2\right)$, also for $\alpha = 1.0$. Notice that $E_{3D}^{self}\left(4\pi Q/L^2\right)^{-1}$ can be significantly larger than $\hat{r}/\left(\alpha^2 - \hat{r}^2\right)$, which illustrates that the interaction of a bunched charged particle beam and a cylindrical conductor wall can be much stronger than for an unbunched charged particle beam.

3.2 Canonical Analysis of the Center-of-Mass Motion

3.2.1 Hamiltonian Formulation

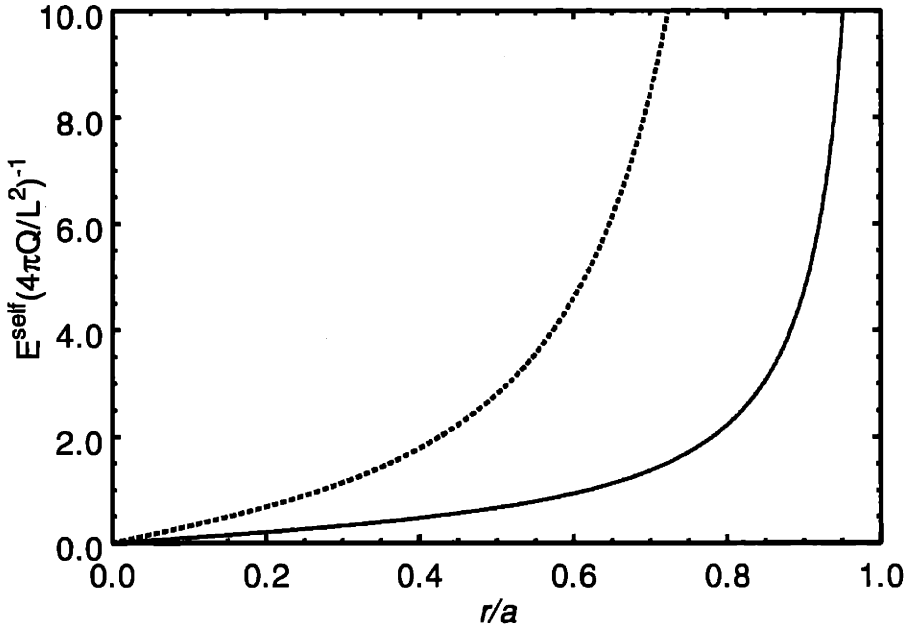

Figure 3-2: Plots of $E_{3D}^{self}\left(4\pi Q/L^2\right)^{-1}$ (dashed line) and the first term of $E_{3D}^{self}\left(4\pi Q/L^2\right)^{-1}$ (solid line), that is the 2-D unbunched term $\hat{r}/\left(\alpha^2-\hat{r}^2\right)$, versus r/a for $\alpha=1.0$.

We can investigate the radial dynamics of one rod of charge (2-D) or one string of charges (3-D) interacting with its self-field and a constant applied magnetic field, $\mathbf{B} = B\hat{\mathbf{e}}_z$. In either system, there are no forces in the longitudinal direction. Therefore, we may describe all of the dynamics using a Hamiltonian in the radial and azimuthal directions and set the longitudinal velocity to zero ($V_z = 0$) without loss of generality. In particular, the Hamiltonian for tranverse motion is given by

$$H = \frac{1}{2M}\left[\left(P_r - \frac{QA_r}{c}\right)^2 + \frac{1}{r^2}\left(P_\theta - \frac{rQA_\theta}{c}\right)^2\right] + Q\phi_{eff}^{self}, \tag{3.12}$$

where $\mathbf{P}$ is the canonical momentum, $\mathbf{A} = \frac{rB}{2}\hat{\mathbf{e}}_\theta$ is the vector potential, and

$$\phi_{eff}^{self} = -\int_0^r E^{self}\, dr. \tag{3.13}$$

It should be noted that the self-electric field defined in Eq. (3.9) is purely due to the induced surface charge on the conductor, while the self-electric field associated with the potential defined in Eq. (3.2), includes both the effect of the charge bunches and the induced surface charge. In the analysis of the center-of-mass motion of the charge bunches, the net internal force is zero. Therefore, it is sufficient to consider only the self-field potential ϕ_{eff}^{self} due to the induced surface charges as defined in Eq. (3.13).

When analyzing the 2-D system, we can set $M = \lambda_m L$ where λ_m is the line mass density of the rod, and $Q = \lambda L$. Dividing by L on both sides of Eq. (3.12) yields a Hamiltonian per unit length, which correctly describes the 2-D dynamics. Applying Hamilton's equations to Eq. (3.12) gives the following set of normalized equations:

$$\begin{aligned}
\frac{d\hat{r}}{d\tau} &= \hat{P}_r, \\
\frac{d\hat{P}_r}{d\tau} &= \frac{\hat{P}_\theta^2}{\hat{r}^3} - \hat{r} + \xi\hat{E}^{self}, \\
\frac{d\theta}{d\tau} &= \frac{\hat{P}_\theta}{\hat{r}^2} - 1, \\
\frac{d\hat{P}_\theta}{d\tau} &= 0,
\end{aligned} \tag{3.14}$$

where normalized variables and parameters are defined by

$$\begin{aligned}
\tau &= \omega_L t, \\
\hat{P}_r &= \frac{2\pi P_r}{ML\omega_L}, \\
\hat{P}_\theta &= \left(\frac{2\pi}{L}\right)^2 \frac{P_\theta}{M\omega_L}, \\
\xi &= \frac{32\pi^2 Mc^2}{L^3 B^2}, \\
\hat{E}^{self} &= \frac{L^2 E^{self}}{4\pi Q}, \\
\omega_L &= \frac{QB}{2Mc},
\end{aligned} \tag{3.15}$$

and ω_L represents the Larmor frequency. From Eq. (3.14), it is obvious that the canonical angular momentum is conserved. Combining the first two equations in Eq. (3.14), and denoting initial conditions with a subscript 0, we can find an expression relating the canonical radial momentum with the radial position,

$$\hat{P}_r = \pm\sqrt{\hat{P}_{r0}^2 + F(\hat{r}_0) - F(\hat{r})} \tag{3.16}$$

where F represents an effective potential energy, and is given by

$$F(\hat{r}) = \frac{\hat{P}_\theta^2}{\hat{r}^2} + \hat{r}^2 + \xi \ln\left(1 - \frac{\hat{r}^2}{\alpha^2}\right) \tag{3.17}$$

for the 2-D case, and

$$F(\hat{r}) = \frac{\hat{P}_\theta^2}{\hat{r}^2} + \hat{r}^2 + \xi ln\left(1 - \frac{\hat{r}^2}{\alpha^2}\right) - 2\xi\sum_{n=1}^{\infty}\frac{K_0(n\alpha)}{I_0(n\alpha)} I_0^2(n\hat{r}) - 4\xi\sum_{n=1}^{\infty}\sum_{l=1}^{\infty}\frac{K_l(n\alpha)}{I_l(n\alpha)} I_l^2(n\hat{r}) \tag{3.18}$$

for the 3-D case. Making use of the asymptotic properties of the modified Bessel functions, it is readily shown that in the limit $a/L \to \infty$, $F(\hat{r})$ in Eq. (3.18) for the 3-D case approaches to $F(\hat{r})$ in Eq. (3.17) for the 2-D case. Therefore, the analysis of confinement in the 2-D system will be fully recovered in the 3-D analysis in the $a/L \to \infty$ limit.

3.2.2 Numerical Results for 2-D System

Figures 3-3(a) and 3-3(b) show $F(\hat{r})$ plotted for two different sets of values of $(\xi, \hat{P}_\theta)$ for the 2-D system. There are two possible behaviors for this function to have. In Fig. 3-3(a), there is a kink (i.e., the function has one local minimum and one local maximum), while for Fig. 3-3(b) the function is monotonically decreasing. A function, $F(\hat{r})$, with a kink leads to a radial phase space $(\hat{r}, \hat{P}_r)$, as is illustrated in Fig. 3-4(a), which contains both trapped and untrapped particle orbits. An untrapped particle orbit will result in the particle eventually being lost to the conductor wall, whereas a trapped orbit corresponds to a particle confined inside of the perfectly conducting cylinder. A monotonically decreasing function as in Fig. 3-3(b), will produce a phase space such as Fig. 3-4(b), which only contains untrapped particle orbits.

3.2.3. Numerical Results for the 3-D System

To illustrate the 3-D effects (i.e., effects of beam bunching), we compare the phase space for the 3-D case in Figs. 3-5(a) and 3-5(b) with the 2-D case shown in Fig. 3-4. In particular, 3-5(a), which has only untrapped orbits, has the same ξ and $\hat{P}_\theta$ values as Fig. 3-4(a), illustrating the added effect of the electric field in the 3-D regime. However, trapped particle orbits do exist at lower values of ξ such as for the value of ξ shown in Fig. 3-5(a).

3.3 Confinement Criterion for NRCM Model

The complete criterion for trapped particle orbits is threefold: a) $F(\hat{r})$ must have a kink; b) the initial particle radius must be chosen between the local maximum of $F(\hat{r})$ and the other point on $F(\hat{r})$ corresponding to the same value; and c) the initial radial momentum must be sufficiently small, such that

$$\hat{P}_{r0}^2 \leq F(\hat{r}_0) - F(\hat{r})\big|_{min}. \tag{3.19}$$

The most important of the three criteria for trapped particle orbits is the first. We therefore determine the region in parameter space $(\alpha, \xi, \hat{P}_\theta)$ space for both the 2-D and

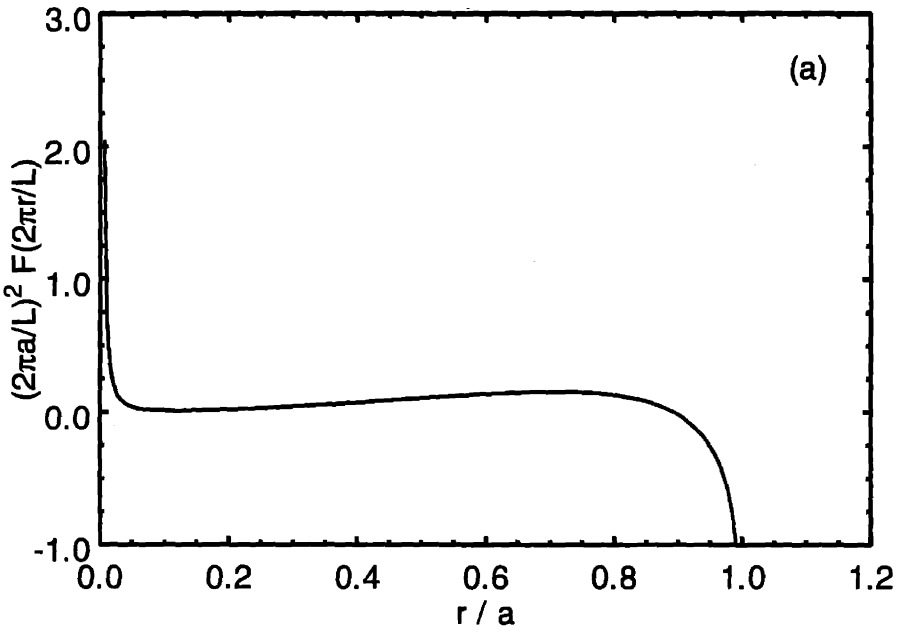

Figure 3-3(a): Plot of the effective potential $F(\hat{r})$ vs. $\hat{r}$ in the 2-D system for the choices of system parameters corresponding to $\xi/\alpha^2 = 0.5$ and $\hat{P}_\theta/\alpha^2 = 0.01$.

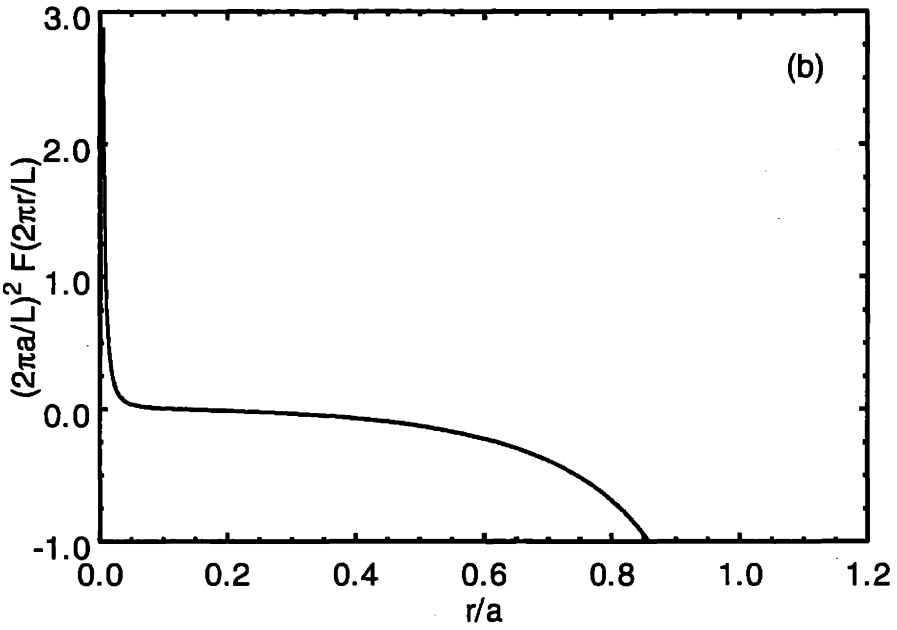

Figure 3-3(b): Plot of the effective potential $F(\hat{r})$ vs. $\hat{r}$ in the 2-D system for the choices of system parameters corresponding to $\xi/\alpha^2 = 3.0$ and $\hat{P}_\theta/\alpha^2 = 0.01$.

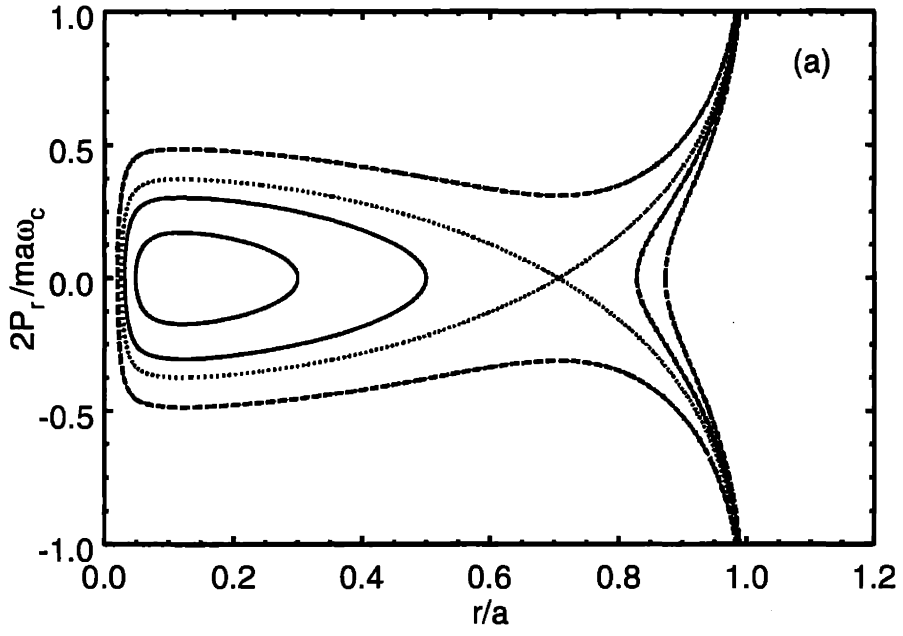

Figure 3-4(a): Plot of the radial phase space in the 2-D system for the case with the same choice of system parameters as those shown in Fig. 3-3(a).

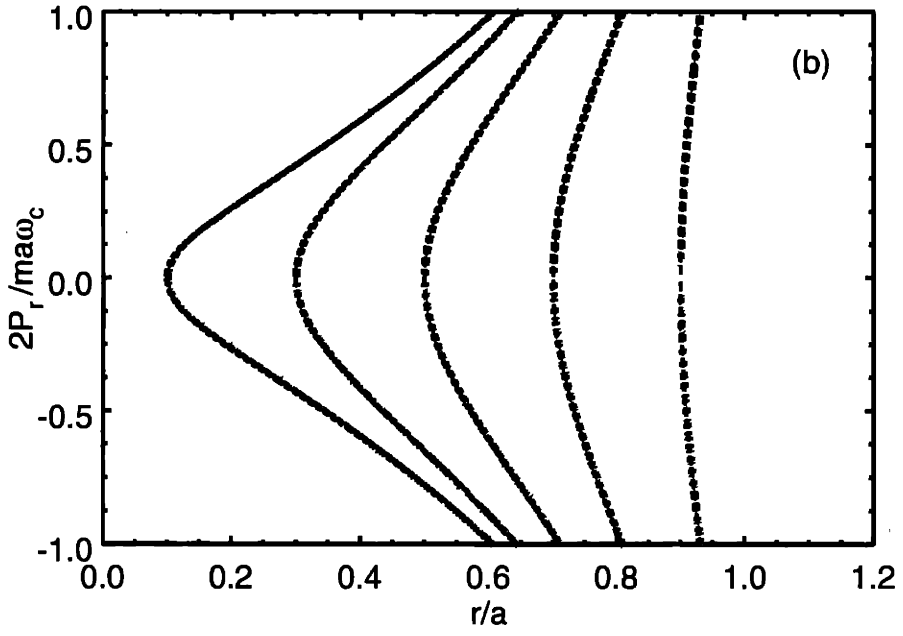

Figure 3-4(b): Plot of the radial phase space in the 2-D system for the case with the same choice of system parameters as those shown in Fig. 3-3(b).

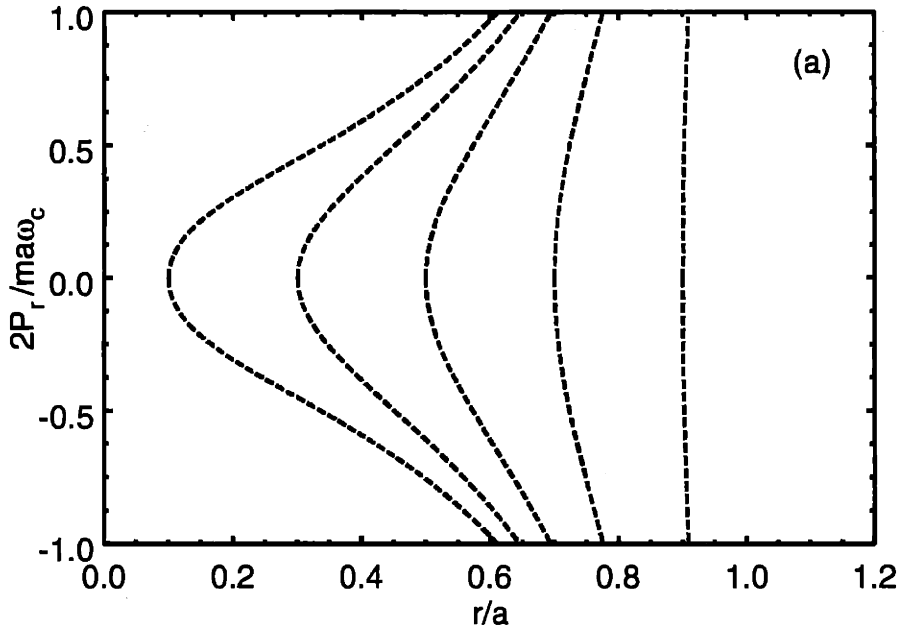

Figure 3-5(a): Plots of the radial phase space in the 3-D system for the choices of system parameters corresponding to $\xi/\alpha^2 = 0.5$, $\hat{P}_\theta/\alpha^2 = 0.01$ and $\alpha = 1.0$.

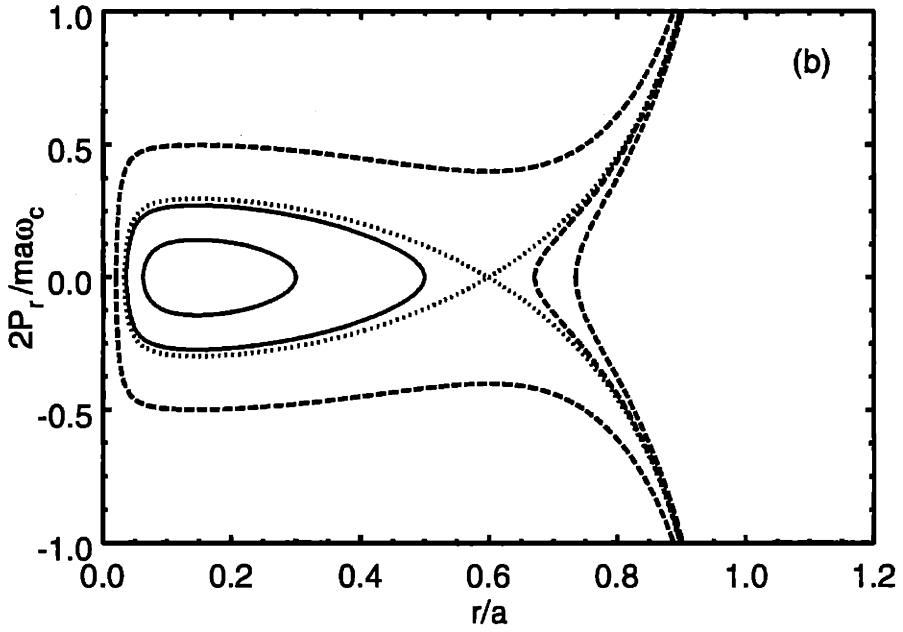

Figure 3-5(b): Plots of the radial phase space in the 3-D system for the choices of system parameters corresponding to $\xi/\alpha^2 = 0.1$, $\hat{P}_\theta/\alpha^2 = 0.01$ and $\alpha = 1.0$.

3-D systems, such that $F(\hat{r})$ has a kink. In order to find this criterion for $F(\hat{r})$, i.e., that trapped particle orbits may exist, we must look for the conditions such that $F'(\hat{r}) = F''(\hat{r}) = 0$, where $F'(\hat{r}) = dF(\hat{r})/d\hat{r}$ and $F''(\hat{r}) = d^2F(\hat{r})/d\hat{r}^2$. This represents that transition point between $F(\hat{r})$ being monotonic and non-monotonic.

3.3.1 Confinement Criterion for 2-D System

It is evident in Eq. (3.17) that the only increasing term in $F(\hat{r})$ is the $\hat{r}^2$ term and all other terms are decreasing. When $\xi = 0$, applying the transition condition $F'(\hat{r}) = F''(\hat{r}) = 0$ yields $\left|\hat{P}_\theta\right| = \alpha^2$ at $\hat{r} = \alpha$ for both systems. However, when $\hat{P}_\theta = 0$, it follows from Eq. (3.17) that $F(\hat{r}) = \hat{r}^2 + \xi \ln\left(1 - \hat{r}^2/\alpha^2\right)$. Expanding $F(\hat{r})$ near $\hat{r} = 0$ yields $F(\hat{r}) \cong \hat{r}^2\left(1 - \xi/\alpha^2\right)$. So $F(\hat{r})$ will not be monotonic at $\hat{r} = 0$ for sufficiently small $\hat{P}_\theta$ when the coefficient of the quadratic term is positive (i.e., when $\xi/\alpha^2 < 1$). Therefore, the necessary conditions for $F(\hat{r})$ to have a kink are $\left|\hat{P}_\theta\right| < \alpha^2$ and $\xi/\alpha^2 < 1$.

Manipulating the equation $F'(\hat{r}) = 0$ and letting $y = \alpha\hat{r}$, we find that

$$y^6 + (\nu - 1)y^4 + \left(1 - y^2\right)\mu^2 = 0, \tag{3.20}$$

where $\mu = \hat{P}_\theta/\alpha^2$ and $\nu = \xi/\alpha^2$. Because $0 < y < 1$ $(0 < \hat{r} < \alpha)$, we can further simplify Eq. (3.20) by letting $z = y^2$, and obtain

$$W(z) \equiv z^3 + (\nu - 1)z^2 + (1 - z)\mu^2 = 0, \tag{3.21}$$

where $0 < y < 1$. Note that $W(0) = \mu^2 > 0$ and $W(1) = \xi > 0$.

It is straightforward to show that $W(z)$ has precisely one zero when the transition point occurs. This statement is equivalent to stating that the minimum of $W(z)$ must be equal to zero, and that the minimum must occur between 0 and 1 for trapping to occur. These conditions yield

$$3z_{min}^2 + 2(\nu - 1)z_{min} - \mu^2 = 0, \tag{3.22}$$

$$0 < z_{min} = \frac{(1 - \nu) + \sqrt{(1 - \nu)^2 + 3\mu^2}}{3} < 1, \tag{3.23}$$

$$z_{min}^3 + (\nu - 1)z_{min}^2 + (1 - z_{min})\mu^2 = 0, \tag{3.24}$$

where z_{min} is the minimum of W.

Substituting Eq. (3.23) into Eq. (3.24) and solving for μ with the aid of Eq. (3.22) yields two possible solutions,

$$\mu^2 = \mu_+^2 \quad \text{and} \quad \mu^2 = \mu_-^2, \tag{3.25}$$

where

$$8\mu_\pm^2 = 27 - 18(1-\nu) - (1-\nu)^2 \pm \sqrt{\left(27 - 18(1-\nu) - (1-\nu)^2\right)^2 - 64(1-\nu)^3}\,. \tag{3.26}$$

However, the inequality Eq. (3.23) yields, $\mu^2 < 2\nu + 1$, and by graphical inspection from Figure 3-6, only $\mu^2 < \mu_-^2$ is possible. We find that for the 2-D system, the following inequality must be satisfied for trapped particle orbits to occur

$$8\mu^2 \le 27 - 18(1-\nu) - (1-\nu)^2 \pm \sqrt{\left(27 - 18(1-\nu) - (1-\nu)^2\right)^2 - 64(1-\nu)^3}\,. \tag{3.27}$$

Note that since μ and ν are both independent of L, Eq. (3.27) is also independent of L. Equation (3.27) is plotted later in Fig. 3-7 in terms of normalized P_θ and the effective plasma frequency, as we compare the 2-D case with the 3-D case.

Since the effective density of particles for both systems is given by $n = N/\pi a^2 L$, we can relate ξ/α^2 to the effective plasma frequency $\omega_p = \left(4\pi n q^2/m\right)^{1/2}$ (where $Q = \lambda L = Nq$, and N is the number of particles per bunch), and the cyclotron frequency $\omega_c = qB/mc$ by $\xi/\alpha^2 = 2\omega_p^2/\omega_c^2$, which is the familiar self-field parameter. As shown in Fig. 3-6, the maximum of the self-field parameter occurs at $\left|\hat{P}_\theta\right| = 0$, and the maximum value is $2\omega_p^2/\omega_c^2 = 1$. Therefore, the criterion for the confinement is:

$$2\omega_p^2/\omega_c^2 \le 1. \tag{3.28}$$

Note that $\omega_p^2 = \omega_c^2/2$ corresponds to the Brillouin density limit (Brillouin, 1945; Davidson, 1990, Ch. 8, p. 42).

3.3.2 Confinement Criterion for 3-D System

For the 3-D system when $\hat{P}_\theta = 0$, we can expand Eq. (3.18) near $\hat{P}_\theta = 0$ and find that

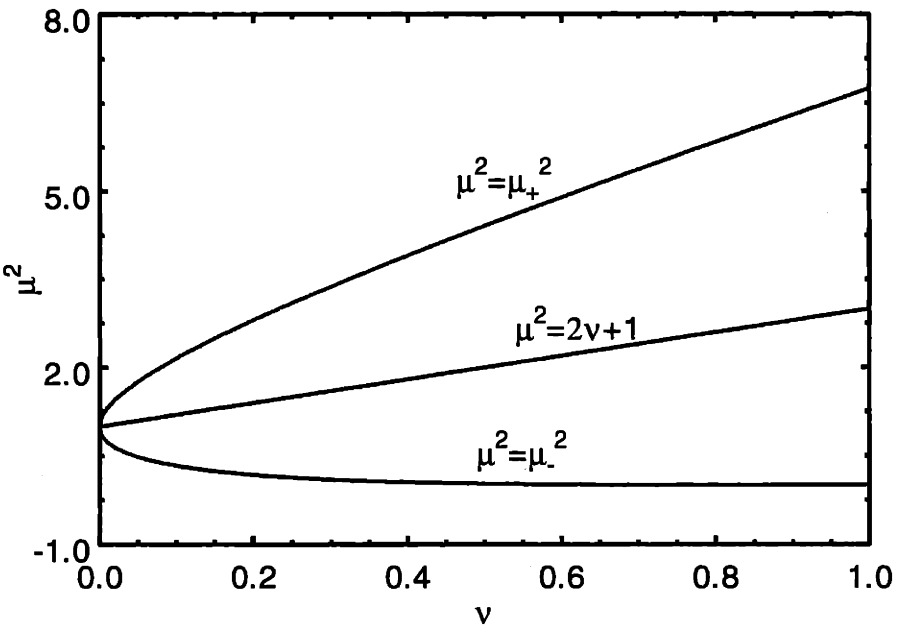

Figure 3-6: Plot of the two branches of solutions $\mu^2 = \mu_+^2$ and $\mu^2 = \mu_-^2$ as a function of ν for the critical transition point along with the curve $\mu^2 = 2\nu + 1$. Note that since $\mu^2 < 2\nu + 1$, the lower branch $\mu^2 = \mu_-^2$ is the only possible solution at the transition point.

the lowest order non-constant term, the quadratic term, will be positive when

$$1-\xi/\alpha^2-\xi\sum_{n=1}^{\infty}n^2\left[\frac{K_0(n\alpha)}{I_0(n\alpha)}+\frac{K_1(n\alpha)}{I_1(n\alpha)}\right]\geq 0. \tag{3.29}$$

By utilizing a formula related to the Wronskian, $I_m(z)K_{m+1}(z)+K_m(z)I_{m+1}(z)=1/z$, we can simplify Eq. (3.29) to

$$\xi\leq\frac{\alpha^2}{1+\sum_{n=1}^{\infty}\frac{n\alpha}{I_0(n\alpha)I_1(n\alpha)}}. \tag{3.30}$$

The upper bound on the self-field parameter for the 3-D system also occurs at $\left|\hat{P}_\theta\right|=0$; hence, the criterion for confinement is

$$\frac{2\omega_p^2}{\omega_c^2}\leq\frac{1}{1+\sum_{n=1}^{\infty}\frac{n\alpha}{I_0(n\alpha)I_1(n\alpha)}}. \tag{3.31}$$

Figure 3-7 illustrates a few of the critical transition curves in a normalized P_θ and $2\omega_p^2/\omega_c^2$ space. In obtaining the results in Fig. 3-6, we use Newton's method to simultaneously solve the equations, $F'(\hat{r})=F''(\hat{r})=0$ for fixed values of $\hat{r}$ and α. Seed values are given to ξ and $\hat{P}_\theta$, and convergence of these values typically occurs within five iterations. Because the 2-D system corresponds to the limit $a/L\to\infty$ as discussed in Sec. 3.2, the transition curve for $a/L=\infty$ is identical to the results predicted by Eq. (3.27).

Fig. 3-8 shows a plot of the upper bounds for transition to occur in the 2-D and 3-D systems. The upper bounds are precisely the intersections of the curves in Fig. 3-7 with the $P_\theta=0$ axis. Before concluding this section, we consider the following two limits of Eq. (3.31). Expanding Eq. (3.31) in the limit $\alpha>>1$ (i.e. a nearly unbunched beam) and $I_0(n\alpha)\approx I_1(n\alpha)\approx e^{n\alpha}/(2\pi n\alpha)^{1/2}$, we obtain

$$\frac{2\omega_p^2}{\omega_c^2}\cong 1-2\pi\alpha^2e^{-2\alpha}=1-\frac{8\pi^3a^2}{L^2}e^{-4\pi a/L} \tag{3.32}$$

which shows that the system asymptotically approaches the 2-D system's Brillouin flow

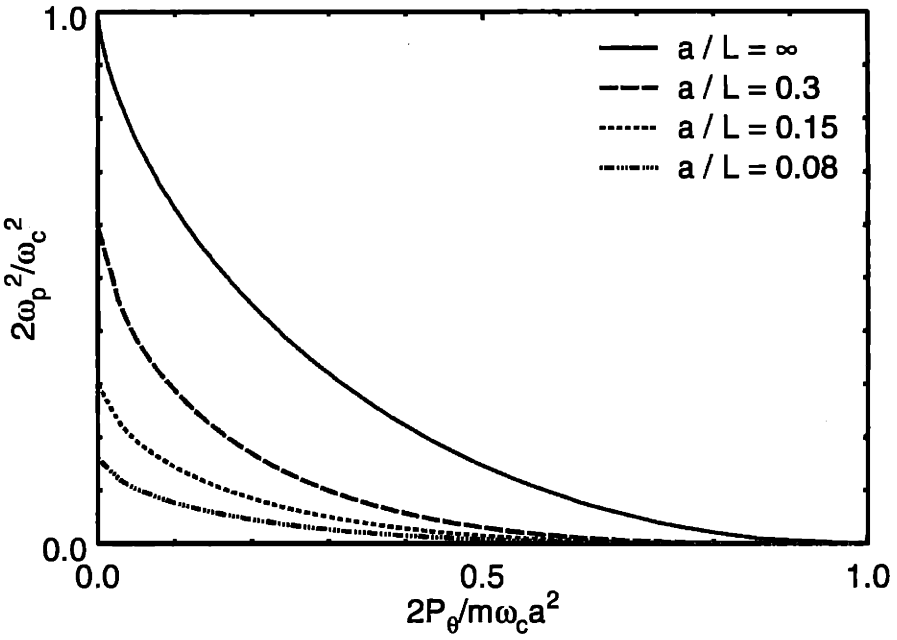

Figure 3-7: Plots of the maximum value of the self-field parameter $\xi/\alpha^2 = 2\omega_p^2/\omega_c^2$ for confinement as a function of normalized canonical angular momentum $\nu = 2P_\theta/m\omega_c a^2$ for several values of the aspect ratio a/L in the 3-D system. Note that the 2-D system corresponds to the limit $a/L = \infty$, and the curve with $a/L = \infty$ is obtained from Eq. (3.27).

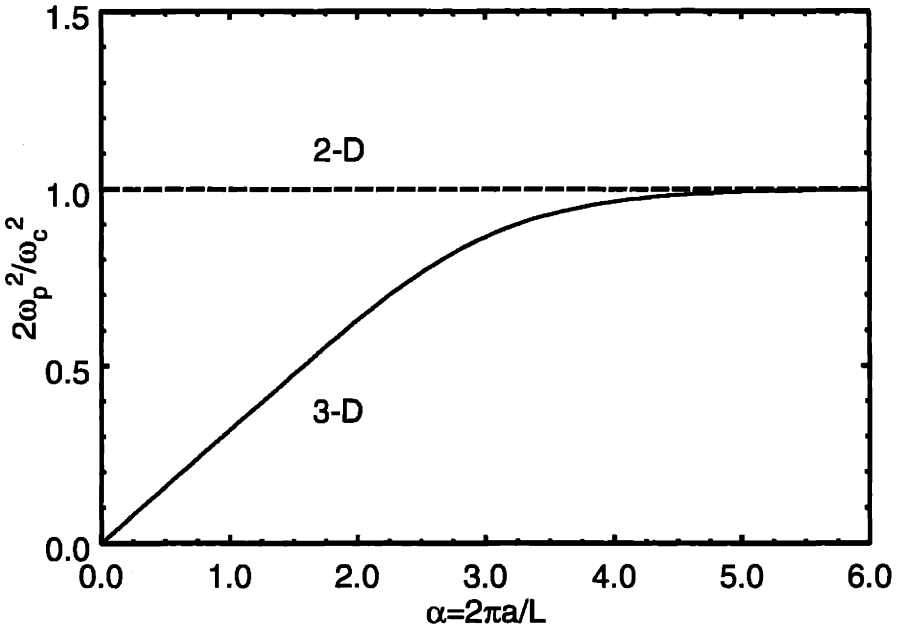

Figure 3-8: Plots of the maximum value of the self-field parameter $2\omega_p^2/\omega_c^2$ for confinement as a function of the aspect ratio a/L for $P_\theta = 0$ in both the 2-D and 3-D systems.

limit for large a/L. The other important limit of Eq. (3.31) with $\alpha << 1$ (i.e. a strongly bunched beam), is readily shown numerically to yield

$$\frac{2\omega_p^2}{\omega_c^2} \cong \frac{\alpha}{\pi} = \frac{2a}{L} \tag{3.33}$$

which is significantly lower than the Brillouin density limit (Brillouin, 1945; Davidson, 1990, Ch. 8, p. 42). It turns out that the approximation in Eq. (3.33) is accurate for $\alpha = 2\pi a/L \leq 2$, as shown in Fig. 3.8.

3.4 Discussion

We have ignored the realistic effect of a finite bunch size in our present model. Incorporating such an effect would reduce the stringent beam confinement criterion placed on the self-field parameter. Qualitatively, both the beam space charge and the induced surface charges would be less dense, and therefore the beam would experience a reduced electric field force from the conducting wall and the other bunches.

A separate effect for a finite charge bunch would be the evolution of the bunch shape. In order to evaluate the importance of such an effect relative to the beam loss mechanism just described, it is necessary to compare their time scales. We will now give an order of magnitude estimate for the escape time (i.e. the time needed for a particle to escape to the wall).

For simplicity, assume that the particle has no canonical angular momentum ($\hat{P}_\theta = 1$), and the particle is initially at the center of the conductor ($\hat{r} = 0$). We will assume that the initial radial momentum is nonzero, but relatively small ($0 < \hat{P}_{r0}^2 < \alpha^2 << \xi$). Using Eq. (3.14) and ignoring the 3-D correction terms $F(\hat{r})$ we obtain

$$\tau = \int_0^\alpha \frac{d\hat{r}}{\hat{P}_r} = \int_0^1 \frac{d\chi}{\left[\hat{P}_{r0}^2/\alpha^2 - \chi^2 - \xi/\alpha^2 \ln(1-\chi^2)\right]^{1/2}} \tag{3.34}$$

where $\chi = \hat{r}/\alpha$. Therefore, the escape time is $t = \tau/\omega_L \sim \left(\xi/\alpha^2\right)^{-1/2}/\omega_L \sim \omega_p^{-1}$.

We can obtain an order of magnitude for the evolution time, by considering the dynamics of only one uniform spherical bunch of radius, R, charge, Q, and mass, M, with no conductor present. Using Coulomb's Law and the Lorentz Force Law, we find that

$$\frac{d^2R}{dt^2} = \frac{Q^2}{MR^2}. \tag{3.35}$$

Equation (3.35) implies that the evolution time scale is of the order $\left(MR^3/Q^2\right)^{1/2}$. Assuming the density is of the order $\left(4\pi R^3/3\right)^{-1}$, then the evolution time is of the order ω_p^{-1}. Hence, the effect of the bunch shape evolution is, in general, not negligible compared to the beam loss mechanism. Therefore, a detailed investigation of the effect of finite bunch size is required to quantify the confinement of moderately bunched beams.

Chapter 4

Relativistic Center-of-Mass (RCM) Model with Periodic Focusing

In Chapter 3, we described a simple model, NRCM, for non-relativistic pencil thin bunched beams in a constant magnetic field. This model utilized the Green's function formalism in Chapter 2 to calculate the electrostatic interaction of the beam and the surrounding conducting wall, and predicted an upper bound on the self-field parameter Eq. (3.31) necessary for beam confinement. A more general model, called the Relativistic Center of Mass (RCM) Model, which was extensively analyzed in a paper by Hess and Chen [Hess and Chen, 2002(a)], and which we will develop in this Chapter, includes relativistic bunch motion through a periodic magnetic focusing field. This model will prove valuable when we model beam confinement in devices with periodic magnetic fields, such as the periodic permanent magnet (PPM) focusing klystrons. A comparison of the predictions of this model with actual PPM focusing klystron experimental results will be presented in Chapter 5.

We will start with a description of the model in Section 4.1, and then generalize the canonical analysis in Section 4.2 to include both the periodic magnetic focusing field and an rf field. Due to the longitudinal variation of the magnetic field, the full dynamics of the system derived in Section 4.2 is four-dimensional, (r, P_r, z, P_z). However, in Section 4.3, we describe a longitudinal averaging technique, which simplifies the dynamics back to two-dimensional (r, P_r). Lastly, in Section 4.4, we derive a confinement criterion for relativistic bunches of charge in a periodic magnetic field based on the averaging technique of Section 4.3.

4.1 Description of Model

The system for which we are analyzing in this Chapter is very similar to the system shown in Figure 3-1. We assume that there exists periodic bunches of charge, $Q = Nq$, spaced by a distance, L, in the laboratory frame. Assuming that the beam is strongly bunched longitudinally by an rf-field, and has a negligibly small transverse size, we approximate the beam bunches by periodic point charges. The bunches are inside of an infinite conducting cylinder with radius a.

There are three main differences between the current model and the one described in Chapter 3. The first difference is that now we assume each bunch of charge is moving with a relativistic longitudinal speed, v_b, as opposed to remaining in the rest frame of the beam. The longitudinal motion of the beam will generate a current flowing along the surface of the conductor. This current will generate a non-negligible magnetic field, by which the beam may couple.

Secondly, instead of the externally applied constant magnetic focusing field in the NRCM model, we assume the presence of a general periodic magnetic solenoidal field,

$$\mathbf{B}^{ext}(z) = B(z)\hat{\mathbf{e}}_z - \frac{1}{2}B'(z)\left(x\hat{\mathbf{e}}_x + y\hat{\mathbf{e}}_y\right), \tag{4.1}$$

where

$$B(z) = B_0\cos(k_0 z). \tag{4.2}$$

where k_0 is the wave number associated with the focusing field. The external magnetic field may be written in terms of its vector potential by, $\mathbf{B}^{ext} = \nabla \times \mathbf{A}^{ext}$, where the vector potential is given by

$$\mathbf{A}^{ext} = \frac{rB_0}{2}cos(k_0 z)\hat{\mathbf{e}}_\theta . \tag{4.3}$$

This longitudinal variation in the magnetic field implies that v_b will no longer be constant in the system, rather the longitudinal motion of the beam will be coupled to its transverse motion.

Lastly, we assume that an rf-field is present, $E\cos(kz - \omega t + \varphi)\hat{\mathbf{e}}_z$, which is traveling along with the beam (i.e. $v_b = \omega/k$), where the parameters $k = 2\pi/L$, $\omega = 2\pi f$, and φ

are the wave number, angular frequency, and the relative phase of the rf field with respect to the periodic magnetic field.

4.2 Hamiltonian Formulation

Since the electron bunches are collinear and periodic, we only need to specify the coordinates of the center of mass of one electron bunch in the Hamiltonian. The relativistic single bunch Hamiltonian, which includes the beam-wall interaction, external magnetic focusing, and the interaction of the beam with an rf-field is given by

$$H=\sqrt{M^2c^4+c^2P_r^2+\left(cP_z-QA_z^{self}\right)^2+\left(\frac{cP_\theta}{r}-QA_\theta^{ext}\right)^2}+Q\phi^{self}-\frac{QE}{k}sin(kz-\omega t+\varphi), \quad (4.4)$$

where $Q=-Ne$ is the total charge of an electron bunch, $M=Nm_e$ is the total mass of the electron bunch, N is the number of electrons per bunch, $-e$ and m_e are the electron charge and rest mass, respectively, $\mathbf{P}$ is the canonical momentum of the electron bunch, ϕ^{self} and $\mathbf{A}^{self}$ are the scalar and vector potentials associated with the charge and current on the conductor wall induced by the beam itself, respectively, and c is the speed of light in vacuum.

In expressing Eq. (4.4), we have implicitly assumed that $v_b >> |v_\theta|$ and $v_b >> |v_r|$, which is consistent with the fact that the axial motion remains relativistic, and the usual assumption that the effective Budker parameter is small, or more specifically, $Ne^2/m_ec^2L << a/L$. Consequently, $\mathbf{A}^{self} \cong A_z^{self}\hat{\mathbf{e}}_z$. It will be shown shortly that $A_z^{self} \cong \beta_b\phi^{self}$, which is consistent with the assumptions $v_b >> |v_\theta|$ and $v_b >> |v_r|$.

In order to find the self-field potentials, A_z^{self} and ϕ^{self}, it is useful to momentarily transform to the rest frame of the beam, using the property that the scalar and vector potentials form 4-vectors, $\left(\phi_{rest}^{self}, \mathbf{A}_{rest}^{self}\right)$ and $\left(\phi^{self}, \mathbf{A}^{self}\right)$, in the rest and laboratory frames, respectively. Since there is no longitudinally induced current on the conductor surface in the rest frame, $\mathbf{A}_{rest}^{self}=0$. The beam-wall interaction becomes purely electrostatic in the rest frame, and ϕ_{rest}^{self} may be calculated by solving Poisson's equation.

In Section 3.2, we computed the electrostatic potential ϕ_{rest}^{self} based on the Green's function technique. The result is given by [see Eqs. (3.11) and (3.13)]

$$\phi_{rest}^{self}(r) = \frac{Q}{L_{rest}}\left[ln\left(\alpha^2 - \hat{r}^2\right) - 2\sum_{n=1}^{\infty}\frac{K_0(n\alpha)I_0^2(n\hat{r})}{I_0(n\alpha)} - 4\sum_{n=1}^{\infty}\sum_{l=1}^{\infty}\frac{K_l(n\alpha)I_l^2(n\hat{r})}{I_l(n\alpha)}\right]. \quad (4.5)$$

Here, $L_{rest} = \gamma_b L$ is the rest-frame bunch spacing, $\gamma_b = \left(1-\beta_b^2\right)^{-1/2}$, $\hat{r} = 2\pi r/L_{rest}$, and $\alpha = 2\pi a/L_{rest}$. Using the Lorentz transformation, we find that $\phi^{self} = \gamma_b\phi_{rest}^{self}$ and $\mathbf{A}^{self} = \gamma_b\beta_b\phi_{rest}^{self}\hat{\mathbf{e}}_z = \beta_b\phi^{self}\hat{\mathbf{e}}_z$.

From the Hamiltonian in Eq. (4.4), we can immediately derive the following equations of motion for the center of mass of the bunch in normalized coordinates:

$$\begin{aligned}
\frac{d\hat{r}}{d\tau} &= \frac{\hat{P}_r}{\gamma}, \\
\frac{d\hat{P}_r}{d\tau} &= \frac{-\left(\hat{P}_z - \chi\hat{\phi}_{rest}^{self}\right)\chi\hat{E}_{rest}^{self} + \hat{P}_\theta^2/\hat{r}^3 - \hat{r}\hat{B}_0^2\cos^2(\psi_0\hat{z})}{\gamma} + \frac{2\alpha\gamma_b\hat{E}_{rest}^{self}}{\hat{B}_0\sqrt{\gamma_b^2-1}}, \\
\frac{d\theta}{d\tau} &= \frac{\left(\hat{P}_\theta/\hat{r}^2 - \hat{B}_0\cos(\psi_0\hat{z})\right)}{\gamma}, \\
\frac{d\hat{P}_\theta}{d\tau} &= 0, \\
\frac{d\hat{z}}{d\tau} &= \frac{\hat{P}_z - \chi\hat{\phi}_{rest}^{self}}{\gamma}, \\
\frac{d\hat{P}_z}{d\tau} &= \frac{-\left(\hat{P}_\theta/\hat{r} - \hat{r}\hat{B}_0\cos(\psi_0\hat{z})\right)\hat{B}_0\sin(\psi_0\hat{z})}{\gamma} + \hat{E}_{rf}\cos(\psi\hat{z} - \hat{\omega}\tau + \varphi).
\end{aligned} \quad (4.6)$$

In Eq. (4.6),

$$\hat{r} = \frac{2\pi r}{\gamma_b L}, \quad \hat{P}_r = \frac{2\pi P_r}{\gamma_b ML\omega_L}, \quad \hat{z} = \frac{2\pi z}{\gamma_b L}, \quad \hat{P}_z = \frac{2\pi P_z}{\gamma_b ML\omega_L}, \quad \tau = \omega_L t,$$

are the normalized variables and $\omega_L = QB/2Mc$. The normalized constants associated with the beam, conductor, and magnetic focusing are given by

$$\hat{P}_\theta = \left(\frac{2\pi}{\gamma_b L}\right)^2\frac{P_\theta}{M\omega_L}, \quad \alpha = \frac{2\pi a}{\gamma_b L}, \quad \psi_0 = \frac{k_0\gamma_b L}{2\pi}, \quad \chi = \frac{2\pi Q^2\sqrt{\gamma_b^2-1}}{Mc\gamma_b^2 L^2\omega_L}, \quad \hat{B}_0 = \frac{QB_0 a}{Mc^2}.$$

The normalized constants associated with the rf-field are

$$\psi = \frac{k\gamma_b L}{2\pi}, \quad \hat{\omega} = \frac{\omega}{\omega_L}, \quad \hat{E}_{rf} = \frac{2\pi Q E_{rf}}{M\omega_L^2 \gamma_b L}.$$

The normalized functions associated with the beam-wall interaction are

$$\hat{\phi}_{rest}^{self} = \frac{L_{rest}\phi_{rest}^{self}}{Q}, \quad \hat{E}_{rest}^{self} = -\frac{d\hat{\phi}_{rest}^{self}}{d\hat{r}}.$$

Lastly, the dynamical relativistic kinetic energy factor can be written in terms of normalized coordinates as

$$\gamma = \sqrt{1 + \frac{\hat{P}_r^2 \hat{B}_0^2}{4\alpha^2} + \frac{\left(\hat{P}_z - \chi\hat{\phi}_{rest}^{self}\right)^2 \hat{B}_0^2}{4\alpha^2} + \frac{\left(\hat{P}_\theta/\hat{r} - \hat{r}\hat{B}_0 cos(\psi_0 \hat{z})\right)^2 \hat{B}_0^2}{4\alpha^2}}.$$

We should note that the constant relativistic energy factor γ_b is normally set equal to γ during the initialization of Eq. (4.6), i.e., $\gamma_b = \gamma(\tau = 0)$.

The six dynamical variables in Eq. (4.6) can immediately be reduced to four $(\hat{r}, \hat{P}_r, \hat{z}, \hat{P}_z)$ since the canonical angular momentum, $\hat{P}_\theta$, is a constant and the azimuthal angle θ is a slave variable to the other four variables. Despite the reduction in phase space, the longitudinal and radial motions are still nonlinearly coupled to each other through the periodic focusing term.

In the next section, we will develop longitudinally averaged equations of motion from Eq. (4.6). We will show numerical simulations of the averaged equations and compare it to numerical simulationsof the full bunch dynamics in Eq. (4.6).

4.3 Averaging Technique

4.3.1 Averaged Dynamics

In the analysis of the radial confinement of the orbit of an electron bunch, we perform the canonical transformation $z' = z - v_{ph}t + \varphi/k = \partial F_2/\partial P_{z'}$, $P_{z'} = P_z = \partial F_2/\partial z$, and $H' = H + \partial F_2/\partial t$ with the generating function $F_2(z; P_{z'}, t) = (z - v_{ph}t + \varphi/k)P_{z'}$, where $v_{ph} = \omega/k$ is the phase velocity of the rf field. Expanding the new Hamiltonian H' with small transverse energy, we separate the nonrelativistic transverse motion from the relativistic longitudinal motion, i.e.,

$$H' = H'_{\parallel} + H'_{\perp}, \tag{4.7}$$

$$H'_{\parallel}(z', P_{z'}) = \gamma(P_{z'})Mc^2 - v_{ph}P_{z'} - \frac{QE}{k}sin(kz'), \tag{4.8}$$

$$H'_{\perp} = \frac{1}{2\gamma(P_{z'})M}\left[P_r^2 + \left(\frac{P_\theta}{r} - \frac{Q}{c}A_\theta^{ext}\right)^2\right] + \frac{Q}{\gamma^2(P_{z'})}\phi^{self} \quad , \tag{4.9}$$

where $\gamma(P_{z'}) = \left(1 + P_{z'}^2/M^2c^2\right)^{1/2}$, $A_\theta^{ext} = (rB_0/2)cos\left[k_0(z' + v_{ph}t)\right]$, and use has been made of $A_z^{self} = (P_{z'}/\gamma Mc)\phi^{self}$ for an electron bunch deeply trapped in the rf wave field.

The longitudinal dynamics described by $H'_{\parallel}$ in Eq. (4.8) is readily determined. In particular, the bounce frequency is $\omega_B = \left(EkQ/\gamma_b^3 M\right)^{1/2}$ for an electron bunch deeply trapped in the rf wave field at $kz' = (4n+1)\pi/2$ with $v_z = v_b = v_{ph}$, where n is an integer. Typically, the bounce frequency is comparable to the operating rf frequency.

For the deeply trapped electron bunch, the transverse motion occurs on a time scale that is long compared with the beam transit time through one period of the PPM focusing field. The Hamiltonian $H'_{\perp}$ for the transverse motion can be further simplified by averaging over one period of the PPM focusing field. This gives

$$\langle H'_{\perp}\rangle(r, P_r, P_\theta) = \frac{1}{2\gamma_b M}\left(P_r^2 + \frac{P_\theta^2}{r^2} + \frac{Q^2B_{rms}^2}{4c^2}r^2\right) + \frac{Q}{\gamma_b^2}\phi^{self} \quad , \tag{4.10}$$

where $\langle H'_{\perp}\rangle = (2\pi)^{-1}\int_0^{2\pi/k_0} k_0 dz H'_{\perp}$, $B_{rms} = B_0/\sqrt{2}$ is the rms value of the PPM focusing field, and use has been made of $P_{z'} = \gamma_b\beta_b Mc$. It follows from Eq. (4.10) that the radial equations of motion for the deeply trapped electron bunch averaged over one period of the PPM focusing field are

$$\frac{dr}{dt} = \frac{P_r}{\gamma_b M}, \tag{4.11}$$

$$\frac{dP_r}{dt} = \frac{1}{\gamma_b}\left[\frac{P_\theta^2}{Mr^3} - \frac{Q^2B_{rms}^2 r}{4Mc^2} - \frac{Q}{\gamma_b}\frac{\partial\phi^{self}}{\partial r}\right]. \tag{4.12}$$

Because $\langle H_\perp' \rangle = const.$, we have $P_r^2 = P_{r0}^2 + F(r_0) - F(r)$, where the subscript zero denotes the initial conditions, and $F(r) = P_\theta^2 / Mr^2 + Q^2 B_{rms}^2 r^2 / 4Mc^2 + 2MQ\phi_{rest}^{self}$ is an effective radial potential.

4.3.2 Comparison of Averaged Dynamics with Full Dynamics

In order to validate the use of averaged dynamics for analyzing the radial phase space in PPM focusing, we provide a comparison of the averaged dynamics with the full dynamics. We will demonstrate a close similarity between the phase space orbits of the two cases, and thereby, conclude that the averaging technique is justified. We numerically solve the exact equations of motion (4.6) in four-dimensional phase space, (r, P_r, z, P_z), for the bunched beam in PPM focusing.

We compare the effects of the full PPM focusing and the averaged PPM focusing by assigning $A_\theta^{ext} = rB_0 \cos(k_0 z)/2$ for the full PPM dynamics and $A_\theta^{ext} = rB_{rms}/2$ for the averaged dynamics where $B_{rms} = B_0/\sqrt{2}$. The relativistic mass factor γ dynamically varies in our simulations, since the total kinetic energy of the beam is not constant in the presence of the PPM focusing field.

In our simulations, we use the initial condition $t = z = 0$ and, hence, we choose $\varphi = \pi/2$ in order to satisfy the deeply trapped condition. We numerically integrated the phase space equations with a fourth-order Runge-Kutta scheme, and chose the constants of the system to coincide with the parameters of the SLAC 50 MW PPM klystron (Sprehn, *et al.*, 1997; Sprehn, *et al.*, 2000). The relevant parameters for the 50 MW PPM klystron are listed in Table 1 in Chapter 5, which we will discuss in further detail.

Figure 4-1(a) shows a plot of the normalized radial momentum, $2\pi P_r / \gamma_b mL\omega_L$, versus r/a for the case of no rf-field $(E_{rf} = 0)$. In producing Fig. 4-1(a), we utilize the parameters of the SLAC 50 MW PPM klystron from Table 1 in Chapter 5 and the fact that $k_0 = 2.38\, cm^{-1}$ ($\gamma_b = 1.83$, $\alpha = 0.75$, $\hat{B}_0 = 0.79$, $\chi = 0.022$, $\psi_0 = 1.52$). The normalized canonical angular momentum is a free parameter in the system, which we assign to be $\hat{P}_\theta = 0.001$. The solid curves show phase space orbits using the averaging

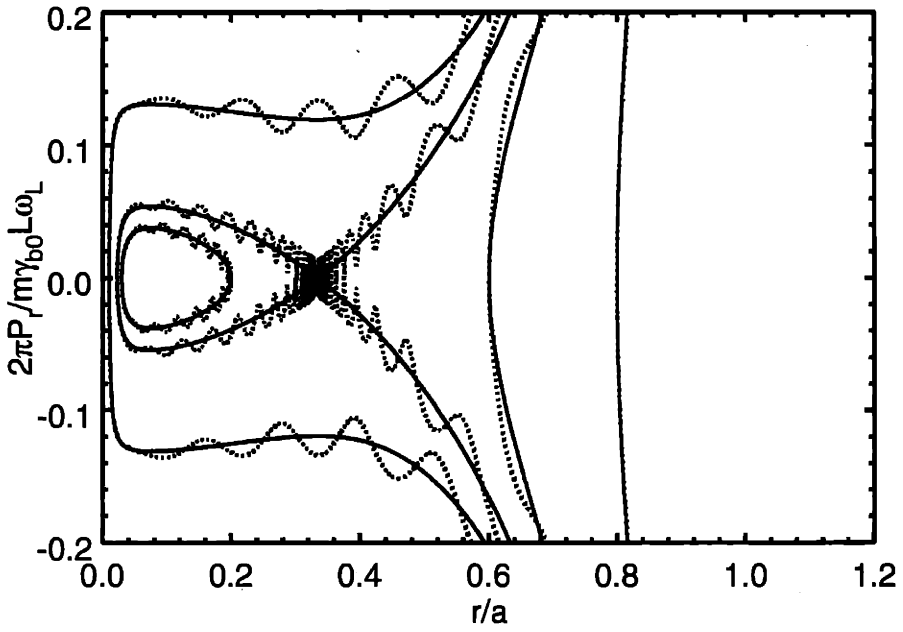

Fig. 4-1(a): Plot of the radial phase space with no rf-field present $(E_{rf} = 0)$ $\gamma_b = 1.83$, $\alpha = 0.75$, and $\hat{P}_\theta = 0.001$ for the case $\chi = 0.022$. The solid curves are computed from the averaged PPM dynamics, and the dotted curves are computed from the full dynamics with $k_0 = 2.38\ cm^{-1}$.

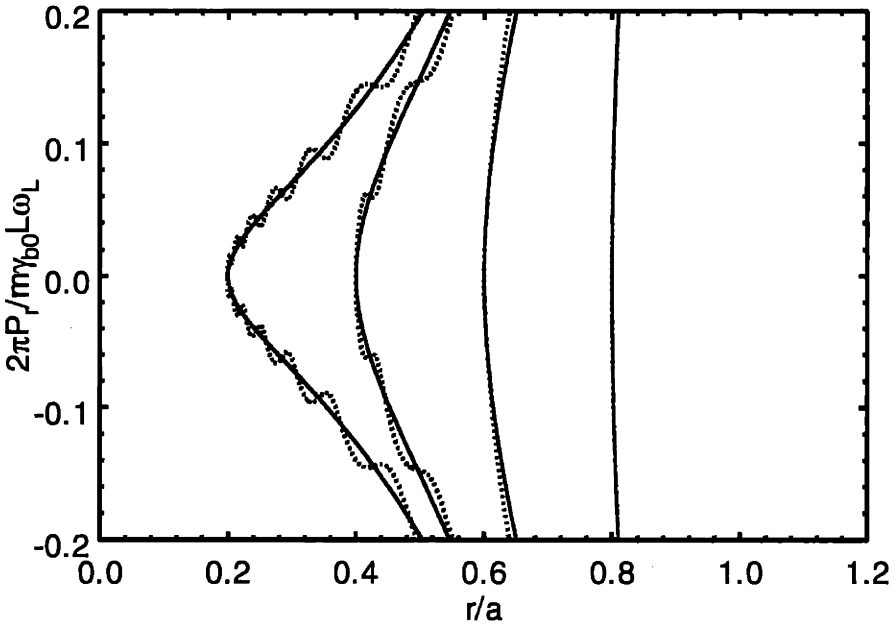

Fig. 4-1(b): Plot of the radial phase space with no rf-field present $(E_{rf} = 0)$ $\gamma_b = 1.83$, $\alpha = 0.75$, and $\hat{P}_\theta = 0.001$ for the case $\chi = 0.028$. The solid curves are computed from the averaged PPM dynamics, and the dotted curves are computed from the full dynamics with $k_0 = 2.38\ cm^{-1}$.

technique developed in Sec. 4.3.1. The dotted curves are the phase space orbits using the full PPM focusing dynamics. We can see that there exists orbits which are confined permanently, as well, orbits which escape to the conductor wall $(r/a=1)$. The most important feature of Fig. 4-1(a) is that the full dynamical phase space curves closely follow their averaged counterparts. We should note, however, that the phase space curves incorporating the full dynamics behave chaotically near the separatrix curve found from the averaging theory. In Fig. 4-1(b), $E_{rf}=0$ as in Fig. 4-1(a), but we decreased the magnetic field such that $\chi=0.028$. From Fig. 4-1(b), we see that all of the phase space curves are unconfined, but again as in Fig. 4-1(a) the full PPM dynamics curves follow the averaged curves. Therefore, Figs. 4-1(a) and 4-1(b) give justification for the averaging technique when no rf-field is present.

In Figs. 4-2(a) and 4-2(b) we show phase plots with the rf-field included, while keeping the other parameters from Figs. 4-1(a) and 4-1(b) fixed. Although, we fix k such that the rf-field is traveling with the beam at the initialization, $dz/dt\big|_{t=0}=\omega/k$, there is freedom in choosing the other parameters associated with the rf-field term, namely E_{rf} and ω. We estimate the rf-field frequency to be the klystron frequency, $\omega\approx 2\pi f$, since the rf-field would be caused by the slow-wave space charge oscillations inside of the klystron. In the case of the SLAC 50 MW PPM klystron (Sprehn, *et al.*, 1997; Sprehn, *et al.*, 2000), $f=11.4\,GHz$, hence $\omega\approx 7.2\times10^{10}\,rad/s$. The design of the SLAC 50 MW PPM klystron allows for a maximum electric field gradient of $E_{rf}\le 70\,MeV/m$. In the simulations corresponding to Figs. 4-2(a) and 4-2(b), we set the electric field equal to and use $E_{rf}=70\,MeV/m$. The solid curves are computed from the averaging dynamical system with no rf-field, while the dotted curves are computed from the full dynamical system with the rf-field. We have performed simulations for a wide range of E_{rf} values ($E_{rf}\le 350\,MeV/m$), and have found only a negligible difference in the actual radial phase space orbits. This can be attributed to the fact that the bunch is deeply trapped by the rf-field, which has phase velocity at nearly the same velocity as the bunch.

The differences in the full dynamics curves with and without the rf-field are typically

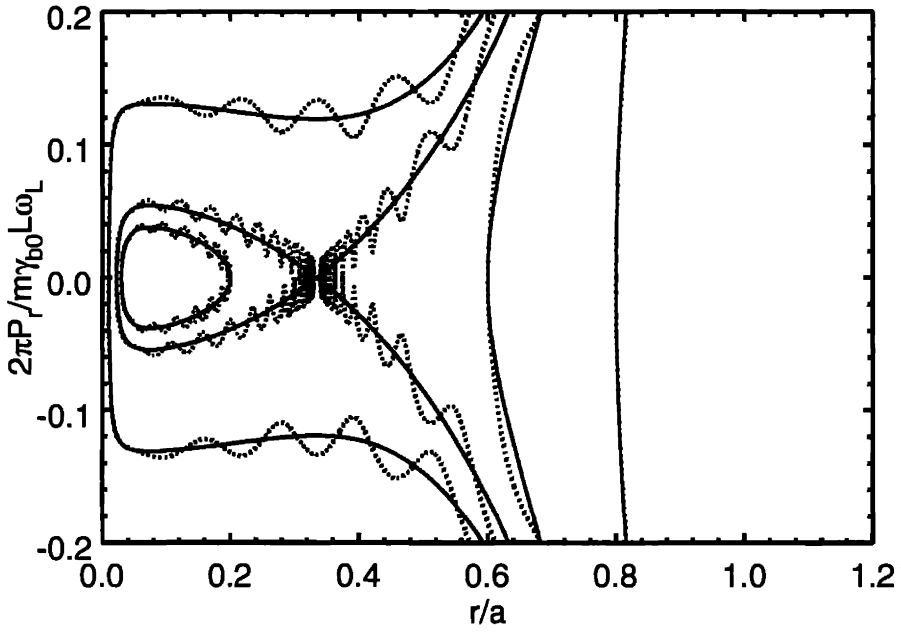

Fig. 4-2(a): Plot of the radial phase space with the rf-field present and keeping the non-rf-field parameters from Figs. 4-1(a) $\omega = 7.2\times10^{10}\ rad/s$ and $E_{rf} = 70\ MeV/m$. Note that $dz/dt\big|_{t=0} = \omega/k$, the solid curves are computed from the averaged PPM dynamics, while the dotted curves are computed from the full dynamics.

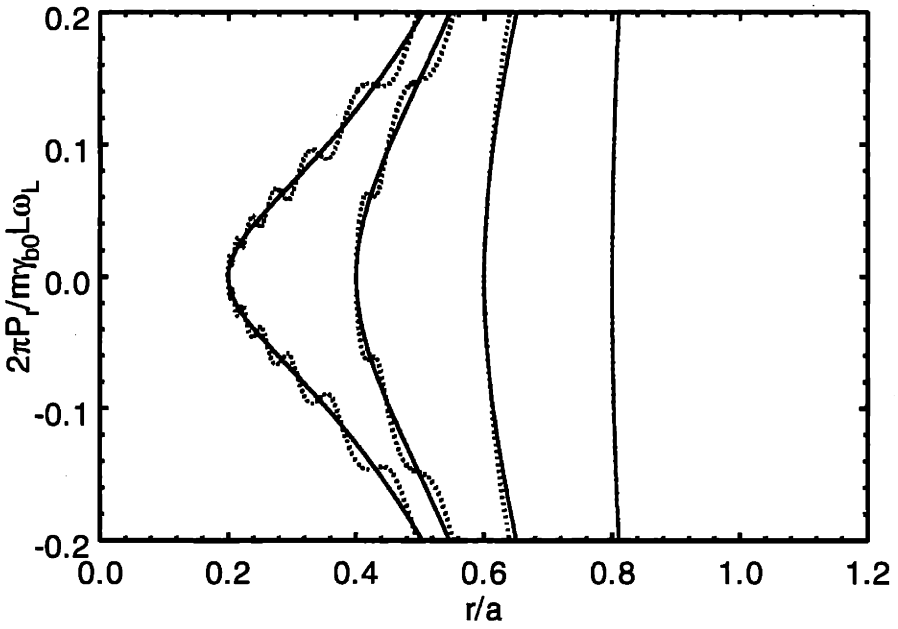

Fig. 4-2(b): Plot of the radial phase space with the rf-field present and keeping the non-rf-field parameters from Fig. 4-1(b) constant for $\omega = 7.2\times10^{10}\ rad/s$ and $E_{rf} = 70\ MeV/m$. Note that $dz/dt|_{r=0} = \omega/k$, the solid curves are computed from the averaged PPM dynamics, while the dotted curves are computed from the full dynamics.

small for sufficiently small time durations $\left(t < 10\omega_L^{-1}\right)$. The reason for the slight differences between these two cases is due to the fact that γ may only change by a fraction of 1% within a small time duration. Hence, the bunch has nearly constant longitudinal velocity and stays deeply trapped in the rf-potential well. The good agreement of the phase space curves in Figs. 4-2(a) and 4-2(b) with those of the averaged system indicate that the averaging technique is also valid when the bunch is deeply trapped by an rf-field. This good agreement of the averaged PPM dynamics with the full dynamics including the rf-field is true for a wide range of values for E and ω, and is not a consequence of the values chosen.

4.4 Confinement Criterion for RCM Model

Now that we have obtained the averaged equations of motion, Eqs. (4.11) and (4.12), we can establish a confinement criterion in a very similar manner as was done for the NRCM model in Section 3.3. In order to determine the condition for radial confinement, we are only interested in orbits near the center of the conductor, i.e. where the beam-wall interaction is weakest. Therefore, by taking the limit of the effective radial potential $F(r)$ as $r \to 0$ $(P_\theta = 0)$ and finding the criterion that $F(r)$ is increasing, we obtain the space charge limit for radially confined orbits,

$$\frac{2\omega_p^2}{\omega_{c,rms}^2} \le \left[1 + \sum_{n=1}^{\infty} \frac{n\alpha}{I_0(n\alpha) I_1(n\alpha)}\right]^{-1}, \tag{4.13}$$

where $\omega_p^2 = \left(4\pi e^2 / m_e\right)\left(N/\pi a^2 L_{rest}\right)$ is the effective plasma frequency squared, $\omega_{c,rms} = eB_{rms}/m_e c$ is the root-mean-square cyclotron frequency, and $\alpha = 2\pi a / L_{rest}$. This self-field parameter limit is similar to the limit in Eq. (3.31) computed for a uniform-focusing magnetic field, $\mathbf{B}^{ext} = B\hat{\mathbf{e}}_z$ (Hess and Chen, 2000). The only difference is that the rms magnetic field on the left-hand side of Eq. (4.13) should be replaced by B.

As previously mentioned in Chapter 3, the limit where the bunch spacing is small compared to the pipe radius, i.e. $\alpha >> 1$, the system resembles a continuous beam. Equation (4.13) becomes $2\omega_p^2 / \omega_{c,rms}^2 \le 1 - 8\pi^3 a^2 \gamma_b^{-2} L^{-2} e^{-4\pi a/\gamma_b L}$, and recovers the Brillouin density limit for PPM focusing. However, as we will see in the next Chapter

the more relevant limit for high-power klystrons is when the bunch spacing is much larger than the pipe radius, i.e., $\alpha < 1$. Numerical analysis shows that equation (4.13) becomes $2\omega_p^2 / \omega_{c,rms}^2 \leq 2a/\gamma_b L$, which is much less than the Brillouin density limit (Brillouin, 1945) This criterion will put significant constraints on the minimum magnetic focusing necessary to confine the beam.

4.5 Discussion

The problem of realistic finite bunch size is a limitation of the RCM model, much like it is a limitation for the NRCM model. There will be a correction of the electric field force acting on the center of mass of the bunch, as well as a correction to the confinement limit in Eq. (4.13), due to the effect of finite transverse bunch size. However, for pencil thin beams this correction will be small compared to the point charge estimate.

As in the NRCM model, there will also be the problem of internal bunch forces, which cause the bunch to expand. The time scale for such an expansion will be of the same order as the escape time, $t \sim \omega_p^{-1}$. Hence, this phenomenon may be important when modeling a actual bunched beam, but unfortunately, such a correction is beyond the scope of this model.

One issue of concern which exist in the RCM model, but is not present in the NRCM model is the finite conductivity, σ_{pipe}, of the conductor pipe. A high energy beam can drive a relatively large current on the surface of the wall. The finite conductivity of the conductor pipe will cause the beam to lose energy due to the thermal energy loss in the pipe with the currents present. This problem may be viewed as an effective electric field, $\mathbf{E}_{eff} = E_{eff,z}\hat{\mathbf{e}}_z$, acting on the bunch in such a way as to slow the beam longitudinally. This effect has been studied in beam physics (see, for example, Chao, 1993, Chap. 5), and in certain scenarios may lead to the well-known resistive wall instability. We can estimate the magnitude of $E_{eff,z}$ with the formula (see for example, Schachter, 1996, Ch.2)

$$\left|E_{eff,z}\right| \sim \left(\frac{Q}{a^2}\right)\left(\frac{(\gamma_b^2-1)^{3/2}c}{16\pi\sigma_{pipe}a}\right)^{1/2} \sim \left|E_r^{self}\right|\left(\frac{(\gamma_b^2-1)^{3/2}c}{16\pi\sigma_{pipe}a\gamma_b^2}\right)^{1/2}. \qquad (4.14)$$

For a copper conductor pipe, $\sigma_{pipe} \approx 1.8\times10^{17}\, s^{-1}$ in CGS units. A typical pipe radius is $a = 1\, cm$, and for HPM sources, a typical beam energy is $\gamma_b \cong 2$. Hence, $\left|E_{eff,z}\right| \sim \left(7\times10^{-5}\right)\left|E_r^{self}\right|$. Therefore, the effect of finite conductivity is relatively small effect in the RCM model.

Another effect that the RCM model does not address, is the finite energy spread of the beam, which would lead to debunching. It also brings into question the validity of the rest-frame transformation, since no frame would exist in which all of the particles in the bunch are at rest. In a real high-power microwave source, such as a klystron, there will be a finite energy spread. However, the only way to develop a model such a beam is to perform a fully 3-D electromagnetic analysis, which, in general, is extremely difficult. In order to obtain a simple electrostatic model like the RCM model, we have to sacrifice the higher-order electromagnetic effects.

Lastly, the rf-field, $E\cos(kz - \omega t + \varphi)\hat{e}_z$, added to the Hamiltonian does not explicitly satisfy Maxwell's equation. There exists a time-dependent magnetic field, which is traveling with the same phase velocity as the electric rf-field, and both fields would have a radial dependence due to the presence of the conductor. However, these effects would be small when deriving the confinement criterion in Eq. (4.13), since the force from both of the fields would scale as $\hat{r}^2$ as $\hat{r} \to 0$. All of the other forces, i.e. the electrostatic self-field force and the magnetic focusing force, scale as $\hat{r}$ as $\hat{r} \to 0$.

Despite the limitations discussed above, the RCM model provides the simplest description of a tightly bunched beam and enabled us to derive a simple beam confinement criterion, which, we will show in Chapter 5, agrees with the experimental observations in several state-of-the-art PPM focusing klystron experiments.

Chapter 5

Application of RCM Model: Current Limit for PPM Focusing Klystrons

In Chapter 4, we presented the RCM theory for examining the relativistic dynamics of a bunch's center of mass in the presence of a periodic magnetic focusing field. The RCM model predicted a self-field parameter limit in Eq. (4.13) based on a longitudinal averaging technique. As we will show in this Chapter, the self-field parameter limit can be powerfully applied to state-of-the-art high-power periodic permanent magnet (PPM) klystrons, which are currently being developed. In particular, the self-field parameter limit can be reinterpreted as a current limit, in which an experiment would have beam loss if it is operating above the limit. In this Chapter, we will focus on applying this model to three PPM klystrons developed at the Stanford Linear Accelerator Center, namely the 11.4 GHz 50 MW XL-PPM (Sprehn *et al.*, 1997, p. 689; Sprehn *et al.*, 2000, p. 132), 11.4 GHz 75 MW XP (Sprehn *et al.*, 1997, p. 689; Sprehn *et al.*, 2000, p. 132), and the 95 GHz Klystrino (Scheitrum, 2000; Scheitrum *et al.*, 2000). The experimental applicability of the RCM model to these devices was first demonstrated in a paper by Hess and Chen [Hess and Chen, 2002(a)].

In Section 5.1, we will provide a brief description of each of the three PPM klystron experiments. In Section 5.2, we will discuss how to apply the self-field parameter limit in Eq. (4.13) to these experiments. Lastly, we will provide concluding remarks and a discussion of the applicability of the RCM model to real experiments in Section 5.3

5.1 Recent PPM Focusing Klystron Experiments

5.1.1 SLAC 11.4 GHz 50 MW XL-PPM and 75 MW XP Klystrons

High-power rf systems are necessary for the next generation of TeV linear accelerators. The Next Linear Collider (NLC) (Tenenbaum, 2000), which is sponsored by SLAC, and the Japanese Linear Collider (JLC) (Chin, 2001), which is sponsored by KEK, are two of the main linear accelerator proposals currently under consideration by the particle and accelerator physics communities. Both of these systems are designed to operate in the X-band regime at f=11.4 GHz, and would need high-power microwave sources, such as klystrons, capable of producing at least 50 MW for 1.5 μs. With this type of power output, 9,000-10,000 of these devices would be necessary for the collider to operate.

Due to the close similarities of the NLC and JLC experiments, SLAC and KEK have formed a collaboration to jointly research and develop the rf system components, including the klystrons. Their research teams are trying to push the performance envelope of the klystrons even further to 75 MW for 3 μs, which would cut the required number of klystrons down to 3,000-4,000.

Originally, the klystron tubes developed at SLAC and KEK utilized constant focusing solenoid magnets. However, in the mid-1990's PPM klystrons were under serious study as alternative to the solenoid klystrons. Figure 5-1 shows a diagram of the SLAC 75 MW XP klystron (Sprehn, *et al.*, 2000). The 50 MW XL-PPM klystron (Sprehn, *et al.*, 1997; Sprehn, *et al.*, 2000) is not shown, but has a very similar design to the 75 MW klystron (Sprehn, *et al.*, 1997; Sprehn, *et al.*, 2000).

The PPM magnets are typically constructed from rare earth elements, such as Samarium-Cobalt. The magnet pole pieces are arranged in alternate polarity, which maximizes the focusing field in the region of the electron beam. The PPM klystrons would effectively reduce the power consumption of the entire accelerator by a factor of two, because the amount of power required for the solenoid magnets is about half of the total power necessary to operate the klystron. Hence, PPM klystrons would offer enormous savings in the entire accelerator budget, compared to their solenoid counterparts.

Unfortunately, the economical savings with the PPM option comes at the price of decreasing the magnetic focusing field. The solenoid magnets are capable of reaching fields in excess of 1 T, whereas a PPM stack typically only reach 0.3-0.4 T. The decrease

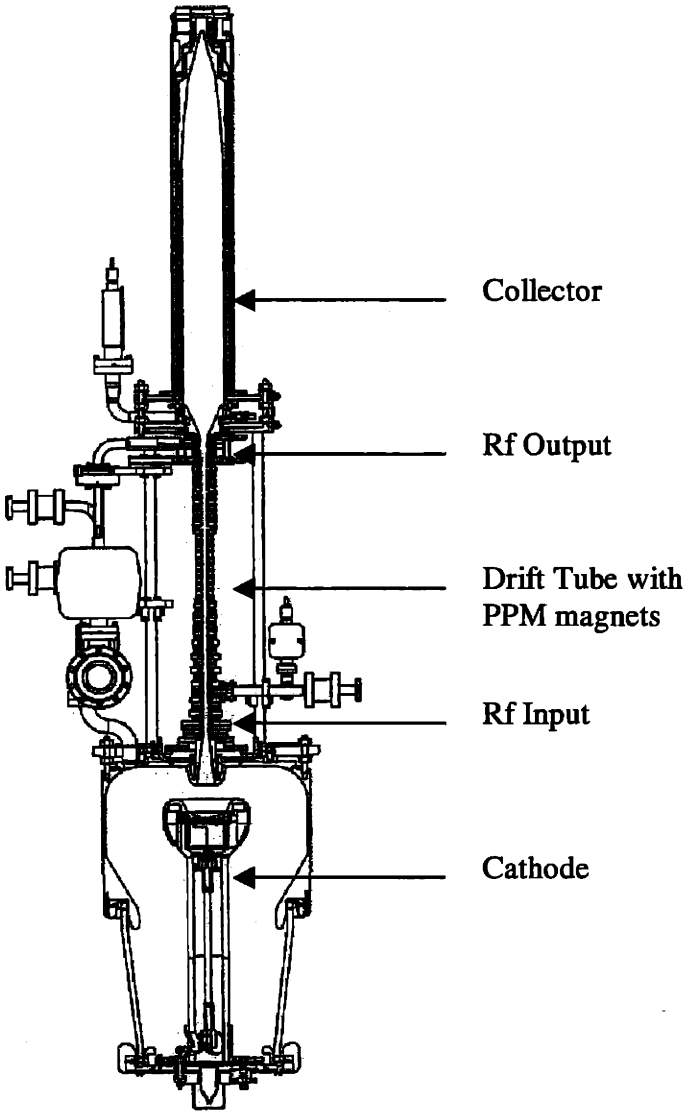

Figure 5-1: Schematic of the SLAC 75 MW Relativistic Klystron Amplifier (from Sprehn *et al*, 2000, p. 132).

Table 5-1: Parameters for SLAC PPM Focusing Klystrons

PARAMETER	50 MW XL-PPM	75 MW XP	KLYSTRINO
f (GHz)	11.4	11.4	95
I_b (A)	190	257	2.4
γ_b	1.83	1.96	1.22
B_{rms} (T)	0.20	0.16	0.29
a (cm)	0.48	0.54	0.04
α	0.75	0.77	1.15
$\left.\frac{8c^2 I_b}{\omega_{c,rms}^2 a^2 I_A}\right\|_{exp}$	0.19	0.28	0.35
$\left.\frac{8c^2 I_b}{\omega_{c,rms}^2 a^2 I_A}\right\|_{cr}$	0.238	0.244	0.365

in magnetic focusing can cause instabilities, such as beam loss due to the beam-wall interaction described in this thesis.

Table 5-1 lists parameters for the 11.4 GHz 50 MW and 75 MW klystrons (Sprehn, *et al.*, 1997; Sprehn, *et al.*, 2000), as well as the 95 GHz Klystrino (Scheitrum, 2000; Scheitrum *et al.*, 2000), which we will describe in the next section. The first five parameters in Table 5-1 are experimentally measured and are relevant for applying the RCM theory. The last three parameters are calculated from the first five, and will be described in Section 5-2.

5.1.2 SLAC 95 GHz Klystrino

The SLAC klystron group has extended its research to include W-band klystrons, one of which is the f=95 GHz Klystrino (Scheitrum, 2000; Scheitrum *et al.*, 2000). The Klystrino, as its name implies, is a small version of its megawatt counterparts. It is designed to be a lightweight, high-power, sub-millimeter radar amplifier. The third column of Table 5-1 lists the important parameters for the Klystrino.

In order to operate at such high frequencies, its components, such as the drift tube, must have sub-millimeter sizes, as well. SLAC has used a specialized lithographic process to fabricate all of the parts. The PPM stack is also constructed from Samarium-Cobalt pole pieces like the 11.4 GHz 50 MW and 75 MW klystrons. Figure 5-2 shows one half of a cut-away diagram of the lithographed components for the Klystrino. In Figure 5-2, the uppermost part of the cut-away, shows the 1 mm thick copper structure with the PPM slots, intermediate cavity slots, and the final beam collector slot. The copper structure is then mounted onto a copper base (middle part), which also houses the PPM stack and a water cooling system (lower part).

Each beam in the Klystrino is designed to produce 100 kW of peak power and 1 kW of average power. The Klystrino will be packaged as a four beam assembly, and therefore will quadruple the peak and average power to 400 kW and 4 kW, respectively. Currently, the Klystrino is under a testing phase. The device has experienced initial problems, such as only having 96-97% of beam transmission without the rf field present. This may be due to beam alignment problems or possibly magnet errors.

Since, the drift tube radius is extremely small, i.e. a=0.4 mm, the problem of internal

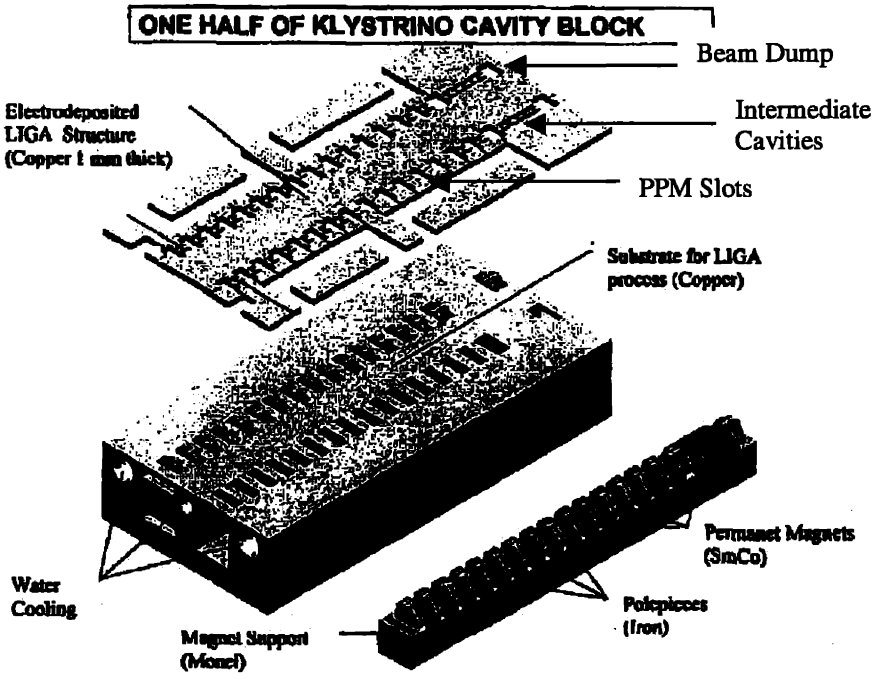

Figure 5-2: Cut-away picture of one-half of the Klystrino device. The uppermost copper structure has slots for the various elements of the beam line listed above. It is mounted on the copper base (middle part), which houses the PPM stack and a water cooling system (lower part) (Scheitrum *et al.*, 2000).

heating is a major concern for the operation of this device. Any beam loss could rapidly heat the structure, and be quite detrimental to the Klystrino's performance. As we will see later, the confinement criterion of Chapter 4 predicts that the beam is only marginally stable to the beam-wall interaction.

5.2 Comparison Between Klystron Experiments and Theoretical Current Limit

We now demonstrate how to relate the first five experimental parameters of Table 5-1 with the confinement criterion in Eq. (4.13). Since there exists only one bunch for every oscillation period of the device, the bunch spacing in the rest frame of the beam is given by $L_{rest} = \gamma_b \beta_b c / f$. Therefore, we obtain

$$\alpha = \frac{2\pi a f}{\gamma_b \beta_b c}. \tag{5.1}$$

We can relate the average beam current (in amperes) with the number of particles per bunch as $I_b = N_b e f$. Hence, we can rewrite the self-field parameter as,

$$\frac{2\omega_p^2}{\omega_{c,rms}^2} = \frac{8c^2 I_b}{\omega_{c,rms}^2 a^2 I_A}, \tag{5.2}$$

where $I_A = \gamma_b \beta_b m_e c^3 / e \equiv \gamma_b \beta_b \times 17\,\text{kA}$ is the electron Alfven current. Then Eq. (4.13) can be rewritten in terms of the parameters in Table 5-1,

$$\frac{8c^2 I_b}{\omega_{c,rms}^2 a^2 I_A} \le \left[1 + \sum_{n=1}^{\infty} \frac{n\alpha}{I_0(n\alpha) I_1(n\alpha)} \right]^{-1}. \tag{5.3}$$

Finally, we apply the beam confinement condition in Eq. (5.13) to the three PPM focusing klystron experiments at SLAC, which we have just discussed. In Table 5-1, we list the α parameter for each of the devices, as well as the experimental self-field parameter, $8c^2 I_b / \omega_{c,rms}^2 a^2 I_A \big|_{exp}$ and the critical self-field parameter, $8c^2 I_b / \omega_{c,rms}^2 a^2 I_A \big|_{crit}$, calculated from Eq. (5.3) using the experimental value for α.

The confinement criterion in Eq. (5.3) is plotted in Figure 5-3, and the operating points for the three klystrons are marked with the letters a, b and c, respectively. As

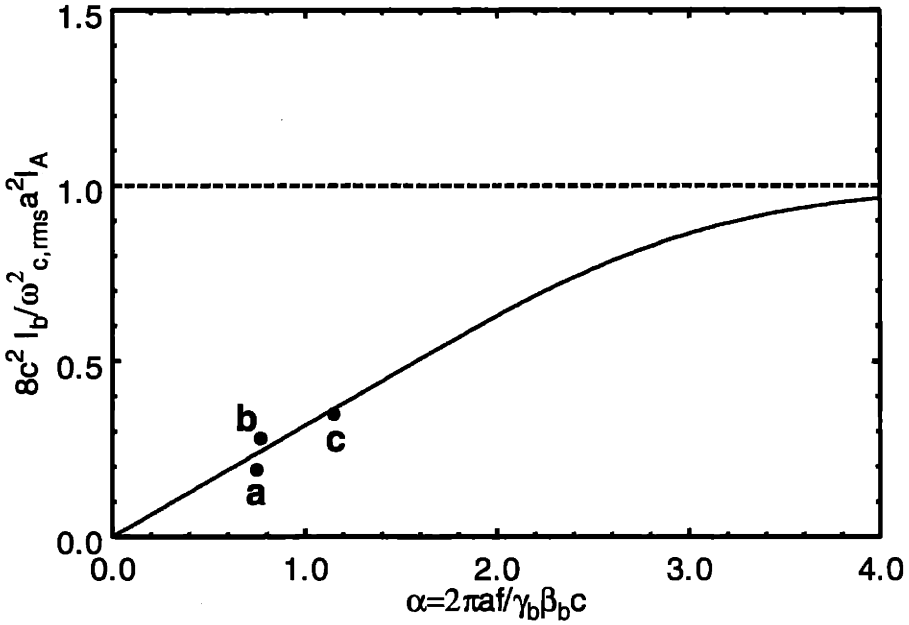

Figure 5-3: Plot of the maximum value of the self-field parameter (solid curve), $8c^2 I_b / \omega_{c,rms}^2 a^2 I_A$, for bunched beam confinement as a function of the parameter $\alpha = 2\pi af / \gamma_b \beta_b c$. Shown in letters are the operating points for three PPM focusing klystrons: a) 50 MW XL-PPM, b) 75 MW XP, and c) Klystrino. The dashed line denotes the Brillouin density limit for an unbunched beam.

shown in Fig. 5-3 and Table 5-1, all three klystrons operate in the regime of $\alpha \cong 1$ and near the self-field parameter limit in Eq. (5.3).

Since the 50 MW klystron operates slightly below the confinement limit, the RCM model does not predict beam loss. However, a mild beam loss still occurs in this device (Sprehn, *et al.*, 1997) through beam halo formation as reported previously [Chen and Pakter, 2000(a) and 2000(b)]. The 75-MW XP is operating outside of the confinement limit. This suggests that the 75 MW klystron has greater beam loss than its 50 MW counterpart, which is consistent with more pronounced X-ray emissions measured at the output section of the device (Sprehn, *et al.*, 2000). The Klystrino design parameters fall just inside of the theoretical limit, suggesting a marginally stable beam-wall interaction.

Notice that all three of the PPM klystrons operate in the regime where $8c^2 I_b / \omega_{c,rms}^2 a^2 I_A \big|_{crit}$ is linearly proportional to α. Since α and $8c^2 I_b / \omega_{c,rms}^2 a^2 I_A$ are both inversely proportional to $\gamma_b \beta_b$, Eq. (5.3) is approximately energy invariant. Therefore, the most important parameters in the RCM model which determine if a system is unstable to beam loss from are I_b, B_{rms}, a, and f.

5.3 Discussion

We should note that, in our model of the klystron beam-wall interaction, we have made a few simplifying assumptions in order to obtain the readily useable result of Eq. (5.3), which we have discussed in Chapter 4. One assumption is the tight bunching approximation, which models the beam bunches as point charges. An actual klystron will have beam bunches of finite transverse and longitudinal size, and hence, the electric force acting on the center-of-mass of each bunch may be modified by a form factor due to the geometry of the beam. Likewise, the tight bunching approximation includes the implicit assumption that space-charge repulsion forces and the beam losses associated with them may be ignored.

We also recognize that real klystron bunches will contain a spatial dependence in the velocity profile, which brings into question the validity of the Lorentz transformation to the rest frame of the beam for calculating the self-fields. However, in order to be

consistent with the tight bunch approximation when calculating the electric self-fields, the beam energy spread must be assumed to be zero.

Finally, we have also made the assumption that the rf-field due to the interacting space-charge wave may be approximated by the final term, $-QE\sin(kz-\omega t)/k$, in Eq. (4.4). This term does not explicitly satisfy Maxwell's equations, since it must have a radial dependence. A radially dependent term would contribute to the tranverse Hamiltonian, Eq. (4.9), and hence would effect the confinement criterion in Eq. (5.3). However, for typical parameters of the PPM klystrons, one can show that the strength of this term is about 1% of the beam-wall interaction term in the radial momentum equation. Hence, the rf-field only has significance in the longitudinal direction and may be ignored in the transverse direction.

Chapter 6

Relativistic Bunched Disk Beam (RBDB) Model

In Chapters 3 and 4, we developed two models, NRCM and RCM, to describe the center of mass dynamics for bunched thin pencil beams with a magnetic focusing field present. Both of these models addressed the beam-wall interaction by using point charges to represent the beam bunches. This approach works well for modeling pencil beams, but for extended bunch charge distributions, such as annular beams, a new model must be developed in order to correctly handle in the beam-wall interaction. We call this new theory the Relativistic Bunched Disk Beam (RBDB) model. The RBDB model was first developed in a paper by Hess and Chen [Hess and Chen, 2002(b)]. In the RBDB model, the bunches are assumed to be thin disks of fluid with arbitrary transverse charge density immersed in a constant magnetic focusing field. It uses the Green's function formalism in Chapter 2 to self-consistently calculate the electric field. The RBDB model includes the beam-wall interaction correction due to a finite size beam, as well as the internal electric field forces within the bunch.

In Section 6.1, we will provide a general description of the system, and then derive a traveling-wave equilibrium solution for the bunches in Section 6.2. From the equilibrium theory, we will also derive a limit on the self-field parameter for the system. In Section 6.3, we will perform numerical examples with different charge distributions to show how to apply the RBDB model. In Section 6.4, we will discuss the formalism and special case solutions, the 2-D rod system and the 3-D large beam, for the rigid-rotor bunched beam equilibrium problem. In Section 6.5, we will develop a local radial stability analysis, which can provide an even lower self-field parameter limit than the equilibrium model in Section 6.2. Lastly, in Section 6.6 we will discuss of the limitations of the RBDB model.

6.1 Description of Model

In general, modeling a bunched beam self-consistently with finite thickness requires a fully three-dimensional numerical calculation, which as mentioned previously can be a very difficult task. In order to incorporate the bunching phenomenon into a partial analytical model, we will simplify the system by treating the annular bunched relativistic electron beam to be a series of charged disks spaced by a distance, L, with zero longitudinal thickness. Each disk represents a bunch of charge that has an equilibrium fluid velocity,

$$\mathbf{V}(\mathbf{r},t) = V_r(r)\hat{\mathbf{e}}_r + V_\theta(r)\hat{\mathbf{e}}_\theta + V_z\hat{\mathbf{e}}_z, \tag{6.1}$$

inside of a grounded perfectly conducting cylindrical pipe of radius, a. The z-axis is chosen to be the axis of the cylinder, and we only analyze azimuthally invariant charge distributions. The azimuthally invariant assumption is a major simplification of the present fluid analysis that still allows for an equilibrium distribution in the beam. Although azimuthal variations in annular intense relativistic electron beams that lead to beam-breakup instabilities are known to exist (see, for example, Davidson, 1990, Ch. 6), for simplicity, we ignore these types of variations in our analysis. We include a constant external magnetic field, $\mathbf{B} = B_0\hat{\mathbf{e}}_z$, for beam focusing. Figure 6-1 illustrates the model.

In general, the bunch distribution has radial dependence, and can be written as

$$n(\mathbf{r},t) = N_b\sigma(r)\sum_{k=-\infty}^{\infty}\delta(z - V_z t - kL), \tag{6.2}$$

where N_b is the number of particles in a bunch, σ contains the radial dependence in the bunch density, and δ is the Dirac delta function. Equation (6.2) immediately yields the following normalization, $2\pi\int_0^a dr\,r\sigma(r) = 1$. An additional assumption in our model is that the effect of finite temperature in the system may be ignored, so that the cold-fluid approximation can be made.

While in any actual HPM device there is a z-dependent velocity spread in the bunch, we have ignored this dependence in Eq. (6.1) to make the problem more tractable. This together with the assumption in Eq. (6.2) describes a tightly bunched beam during the full power operation of the HPM device.

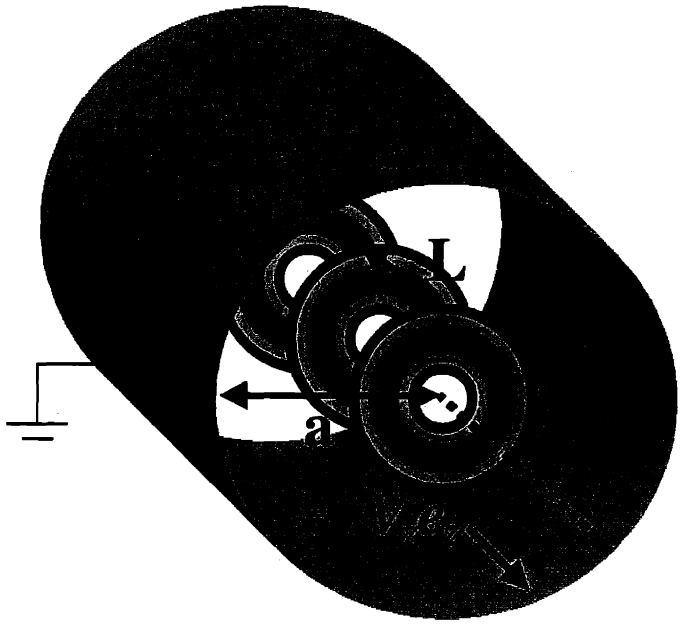

Fig. 6-1: Schematic of periodic bunched annular disks inside of a perfectly conducting drift tube.

Since the transverse charge distribution, σ, will be a sufficiently well-behaved function, i.e., piecewise continuous in the region $0 \le r \le a$, it may be expanded in terms of a Fourier-Bessel series,

$$\sigma(r) = \sum_{m=1}^{\infty} \sigma_m J_0(j_{0m} r/a), \tag{6.3}$$

where $J_l(x)$ is the lth order Bessel function of the first kind, j_{lm} is the mth positive zero of $J_l(x)$, and $\{\sigma_m\}$ is the set of expansion coefficients.

6.2 Traveling-Wave Relativistic Equilibrium

6.2.1 General Equilibrium Solution

We now develop a traveling-wave equilibrium solution from fluid theory, and the prescribed velocity and density profiles defined in Eqs. (6.1) and (6.2). It is readily shown from the continuity equation,

$$\frac{\partial n(\mathbf{r},t)}{\partial t} + \nabla \cdot (n(\mathbf{r},t)\mathbf{V}(\mathbf{r},t)) = 0, \tag{6.4}$$

that $\partial(r\sigma V_r)/\partial r = 0$. Therefore, $r\sigma V_r$ is a constant. Since $r\sigma V_r\big|_{r=a} = 0$, we have $r\sigma V_r = 0$, which implies that

$$V_r = 0 \tag{6.5}$$

everywhere.

In the paraxial approximation, the equilibrium force balance equation is expressed as

$$\gamma_b (\mathbf{V}\cdot\nabla)\mathbf{V} = -\frac{e}{m_e}\left[\mathbf{E}^{self} + \frac{\mathbf{V}}{c}\times\left(\mathbf{B}^{ext} + \mathbf{B}^{self}\right)\right], \tag{6.6}$$

where $\mathbf{E}^{self}$ is the self-consistent electric field due to the charge bunches and the induced charges on the conductor wall, $\mathbf{B}^{ext} = B_0\hat{\mathbf{e}}_z$ is the external focusing magnetic field, and $\mathbf{B}^{self}$ is the magnetic field associated with the longitudinal motion of the beam. Likewise, $-e$ denotes the charge of an electron, m_e is the rest mass of an electron, and c is the speed of light in a vacuum. The relativistic beam mass factor is given by $\gamma_b \cong (1 - V_z^2)^{-1/2}$, since the motion in the transverse direction is small compared to the

longitudinal motion in the paraxial approximation. Note that we are implicitly assuming that the magnetic field due to the transverse motion of the beam is much smaller than the applied field. By enforcing azimuthal symmetry, we find that $\mathbf{E}^{self} = E^{self}(r)\hat{\mathbf{e}}_r$ and $\mathbf{B} = B_0\hat{\mathbf{e}}_z + B^{self}(r)\hat{\mathbf{e}}_\theta$, where E^{self} and B^{self} will be derived in Appendix B and are given by

$$E^{self} = -2\pi N_b e\gamma_b \sum_{m=1}^{\infty} \sigma_m J_1(j_{0m}r/a)\coth(j_{0m}\gamma_b L/2a), \tag{6.7}$$

$$B^{self} = \frac{V_z}{c} E^{self}. \tag{6.8}$$

A non-trivial solution to the equilibrium force equation is V_z = constant in the beam and $V_\theta = V_\theta(r) = r\omega_b(r)$ satisfying the equation

$$\omega_b(r) = \frac{\omega_c}{2\gamma_b}\left[1 \pm \sqrt{1 + \frac{4eE^{self}}{\gamma_b \omega_c^2 m_e r}}\right], \tag{6.9}$$

where $\omega_c = eB_0/m_e c$ is the non-relativistic electron cyclotron frequency.

6.2.2 Equilibrium Space-Charge Limit

Since the argument under the square root in Eq. (6.9) must be positive, we can establish a lower bound on the internal electric field inside the beam,

$$E^{self} \geq -\gamma_b \omega_c^2 m_e r/4e, \tag{6.10}$$

which must be satisfied everywhere $\sigma(r) \neq 0$. It proves useful to introduce the following dimensionless self-electric field

$$\Gamma(r) \equiv -LE^{self}(r)a^2/2rN_b e. \tag{6.11}$$

From Eq. (6.7), we immediately find that

$$\Gamma(r) = \frac{2\pi^2 a^3}{\alpha r} \sum_{k=1}^{\infty} \sigma_m J_1(j_{0m}r/a)\coth(\pi j_{0m}/\alpha), \tag{6.12}$$

where $\alpha = 2\pi a/\gamma_b L$. In order for Eq. (6.10) to be satisfied throughout the beam density profile, a maximum of the function $\Gamma(r)$, which we shall denote as Γ_{max}, must exists.

In general, we can establish an equilibrium space-charge limit on the beam, i.e., an upper bound on the self-field parameter, $2\omega_p^2/\omega_c^2$, where $\omega_p = \left(4\pi N_b e^2 n_b/m_e\right)^{1/2}$ and $n_b = \left(\pi a^2 \gamma_b L\right)^{-1}$ are, respectively, the effective plasma frequency and effective bunch density in the rest frame of the beam. Note that when we Lorentz boost to the rest frame of the beam, the bunch spacing becomes $L_{rest} = \gamma_b L$. Using Eq. (6.10), we can express the equilibrium space-charge limit in terms of the self-field parameter as

$$\frac{2\omega_p^2}{\omega_c^2} \le \frac{1}{\Gamma_{\max}}. \tag{6.13}$$

In the following sections, we will use Eq. (6.13) to uncover equilibrium space-charge limits on strongly bunched annular beams. Once the value of $2\omega_p^2/\omega_c^2$ is chosen in the model, such that it satisfies Eq. (6.13), the fast and slow angular velocity profiles of the beam may be expressed as,

$$\omega_b(r) = \frac{\omega_c}{2\gamma_b}\left[1 \pm \sqrt{1 - \frac{2\omega_p^2}{\omega_c^2}\Gamma(r)}\right], \tag{6.14}$$

where the plus (minus) sign denotes the fast (slow) solution to the angular velocity profile. Physically, $\omega_b(r)$ is only needed in the region where the beam density is non-zero. However, for reasonable choices of $\sigma(r)$, $\Gamma(r)$ will achieve its maximum inside the beam. Combining the density and angular velocity profiles in Eqs. (6.2) and (6.14), along with chosen values for α and $2\omega_p^2/\omega_c^2$, provides a closed model for a traveling-wave equilibrium beam for a bunched annular beam.

6.3 Numerical Calculation of Equilibrium Space-Charge Limit for Bunched Annular Beams

Bunched annular beam distributions form a special class of solutions which self-consistently solve the fluid theory discussed in the previous section. We define the geometry of an annular beam bunch by an inner radius, r_i and an outer radius, r_o. Further, we assume that the beam density is zero for $r \le r_i$ and $r \ge r_o$. It is important

that the radial density goes to zero sufficiently fast at the inner and outer radii, since the electric field defined by Eq. (6.7) will otherwise diverge near the beam edges. In order for the electric field to be finite at the edges, σ must go to zero at least as fast as $\left|\ln|r-r_e|\right|^{-1}$ where r_e is either r_i or r_o. Therefore, the fluid theory does not allow the simple waterbag distribution ($\sigma =$ constant for $r_i \le r \le r_o$) as a solution.

In order to calculate numerically the electric field associated with a bunched annular beam, we must specify a radial density distribution. The choice of a radial density distribution, $\sigma(r)$, for an annular electron beam needs only to satisfy the requirements of being zero at the edges and piecewise continuous. We will demonstrate numerically that the space charge limit will vary only slightly by choosing a different density function.

The two density trial functions, a quadratic function and a tent function, with which we compare the equilibrium space-charge limits are given by

$$\sigma(r) = f_1(r) = \begin{cases} 0, & r \le r_i, \\ 3(r_o - r)(r - r_i)/\pi \bar{r} \delta^3, & r_i \le r \le r_o, \\ 0, & r_o \le r, \end{cases} \tag{6.15}$$

and

$$\sigma(r) = f_2(r) = \begin{cases} 0, & r \le r_i, \\ 2(r - r_i)/\pi \bar{r} \delta^2, & r_i \le r \le \bar{r}, \\ 2(r_o - r)/\pi \bar{r} \delta^2, & \bar{r} \le r \le r_o, \\ 0, & r_o \le r, \end{cases} \tag{6.16}$$

where $\bar{r} = (r_o + r_i)/2$ is an average beam radius and $\delta = r_o - r_i$ is the beam width.

In Figs. 6-2 and 6-3, we summarize our numerical results for the case of the quadratic function. Figure 6-2(a) is a plot of $f_1 a^2$ versus r/a for $\bar{r}/a = 0.8$ and $\delta/a = 0.12$, which corresponds to $r_i/a = 0.74$ and $r_o/a = 0.86$. In Fig. 6-2(a), f_1 has been reconstructed from 200 modes of the Bessel function expansion given by in Eqs. (6.3) and (6.15). The justification for the high number of modes used in this calculation is due to the convergence rate of σ. The beam edges are locations of large numerical fluctuations and slower convergence, when expanding in Bessel functions. Near the

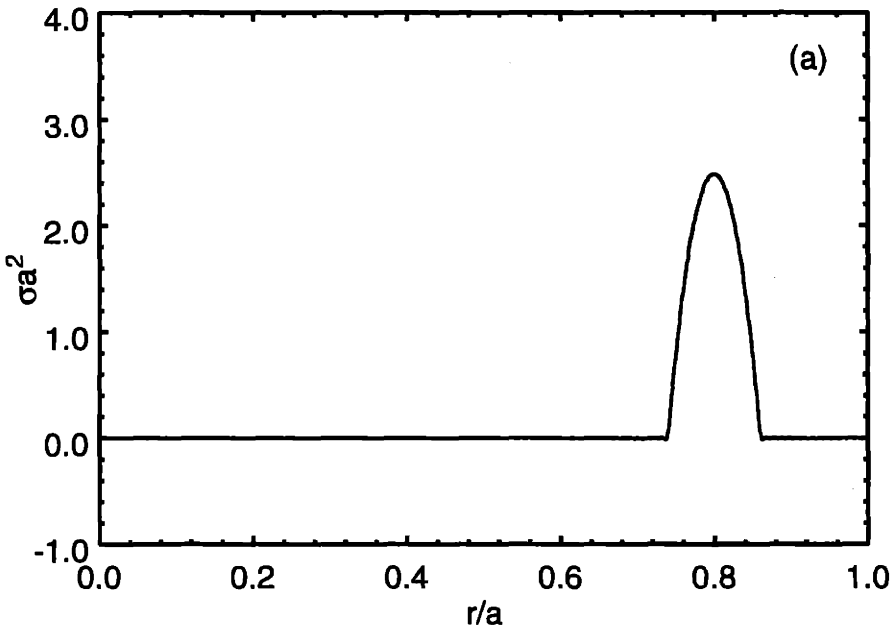

Fig. 6-2(a): Plot of quadratic beam density function versus normalized radius for an annular beam centered at *r/a=0.8*. Here, 200 eigenmodes are used in the calculation.

beam's inner and outer radii, the electric field, given in Eq. (6.7), reaches its maximum and minimum, respectively. Hence, we need enough modes to sufficiently resolve Γ near the outer radius, where Γ_{max} occurs. By choosing $\alpha = 1.0$, we plot Γ in Fig. 6-2(b), as obtained numerically with 200 modes.

Notice that the maximum of Γ occurs slightly less than the outer radius of the beam $(r/a \approx 0.848)$, and its value is approximately $\Gamma_{max} \approx 49.1$. From Eq. (6.13), we immediately conclude that our choice in the self-field parameter must satisfy, $2\omega_p^2/\omega_c^2 \leq 0.0204$. If we only use 20 modes, the value of Γ_{max} is about 10% below $\Gamma_{max} \approx 49.1$, which is obtained with the 200 modes. In general, we find that the numerical results converge with 100 or more modes.

We should also note two facts about the function $\Gamma(r)$. First, as σ approaches a flattop distribution near the outer radius, the maximum of Γ inside the beam will approach r_o and $\Gamma_{max} \to \infty$. Secondly, the fluctuations in Γ near $r/a = 0$ are caused by the mode expansion, and are irrelevant for the current problem, since we are only physically interested in the regime $r_i \leq r \leq r_o$.

Using the 200 mode expansion of $\Gamma(r)$ from Fig. 6-2(b) and Eq. (6.14), we plot the fast and slow branch solutions for $\omega_b(r)$ in Fig. 6-3 as a function of r/a for $2\omega_p^2/\omega_c^2 =$ 0.01, 0.015, 0.019, and $1/\Gamma_{max}$. The function $\omega_b(r)$ is plotted only in the region $r_i \leq r \leq r_o$. Note that the slow branch solution of $\omega_b(r)$ will undergo a sign reversal within the beam, whereas the fast branch will always remain positive. Also, note that at the critical value $2\omega_p^2/\omega_c^2 = 1/\Gamma_{max}$, the fast and slow branches will intersect at one point within the beam, although it is not shown explicitly in Fig. 6-3.

In order to gain further confidence that the model is able to predict the critical self-field parameters for confinement when comparing to experiments, Eq. (6.13) should be approximately invariant for choice of $\sigma(r)$. Hence, we compare the predicted critical self-field parameters for the two trial functions, f_1 and f_2 in Eqs. (6.15) and (6.16). Figures 6-4(a) and 6-4(b) show plots of the exact f_1 and f_2 functions, respectively, for $\bar{r}/a = 0.8$ and various values $\delta/a =$ 0.08, 0.12, 0.16, and 0.2. Figure 6-5 shows a plot of

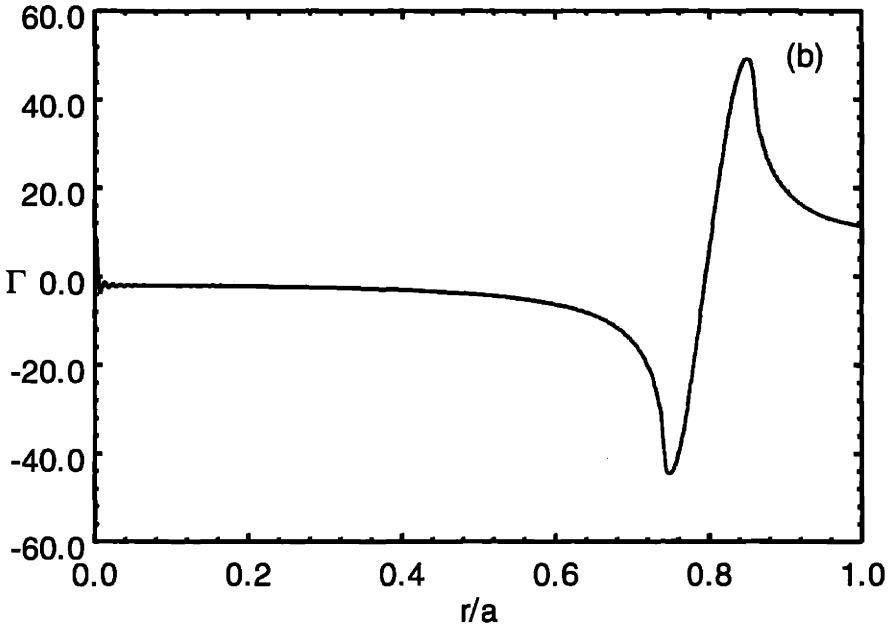

Fig. 6-2(b): Plot of Γ versus normalized radius for the annular beam in Fig. 6-2(a). Here, 200 eigenmodes are used in the calculation.

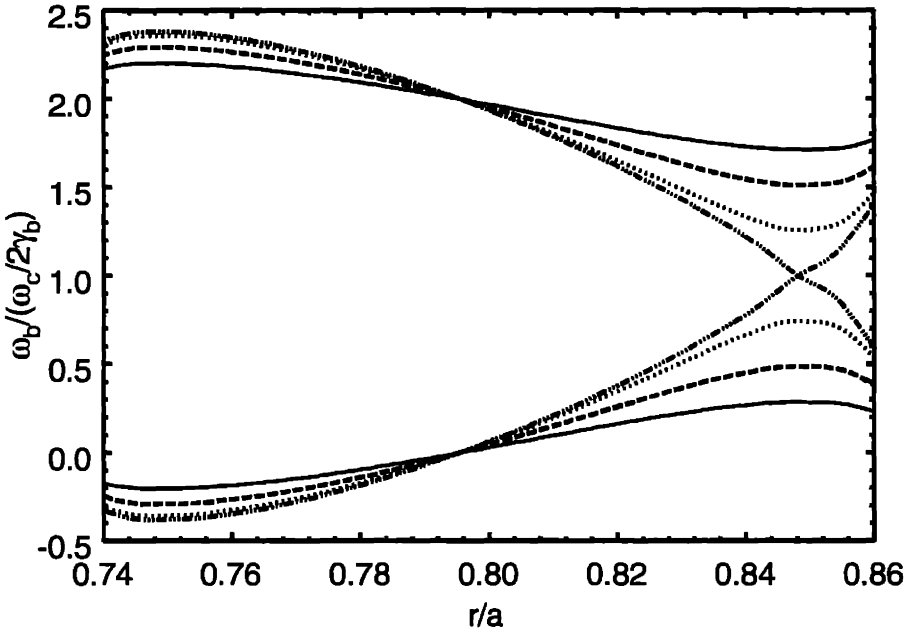

Fig. 6-3: The fast (top of graph) and slow (bottom of graph) branches of $\omega_b(r)$ in the region $r_i \le r \le r_o$ corresponding to the 200 mode expansion of $\Gamma(r)$ in Fig. 6-2(b) for three different values of $2\omega_p^2/\omega_c^2 = 0.01$ (solid lines), 0.015 (dashed lines), 0.019 (dotted lines), and $1/\Gamma_{max}$ (dashed and dotted).

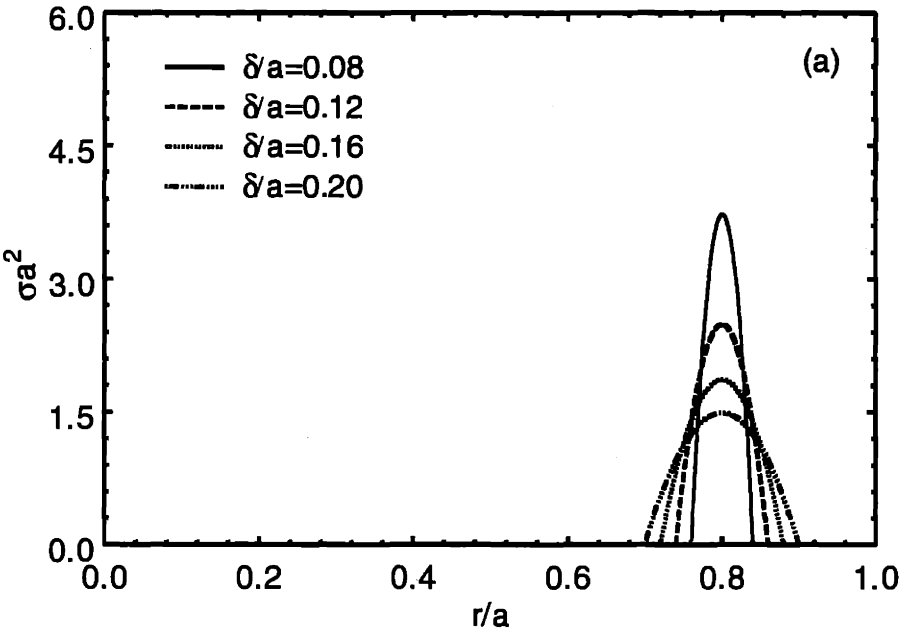

Fig. 6-4(a): Plots of quadratic versus normalized radius for several bunched annular beams centered at *r/a=0.8*.

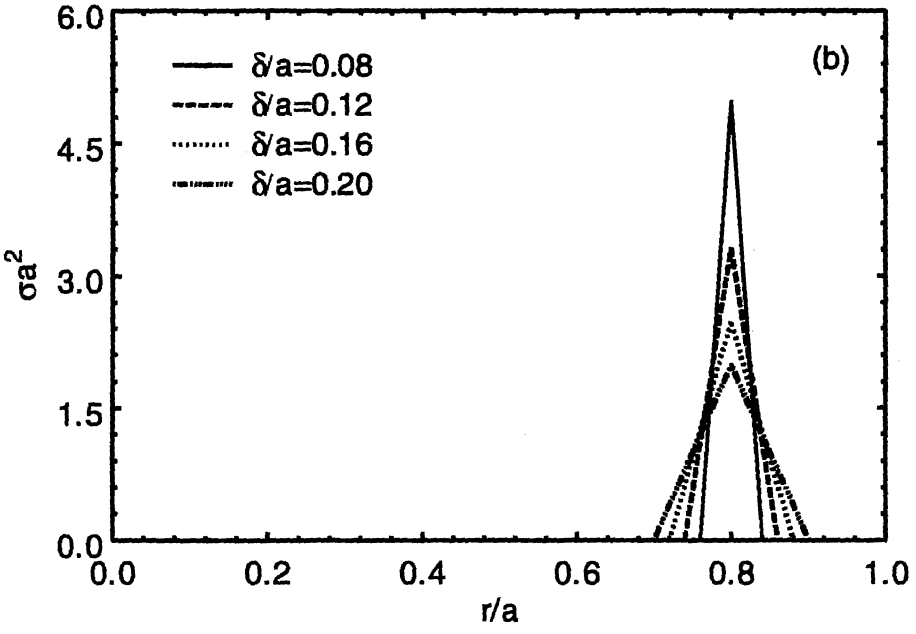

Fig. 6-4(b): Plots of tent beam density functions versus normalized radius for several bunched annular beams centered at *r/a=0.8*.

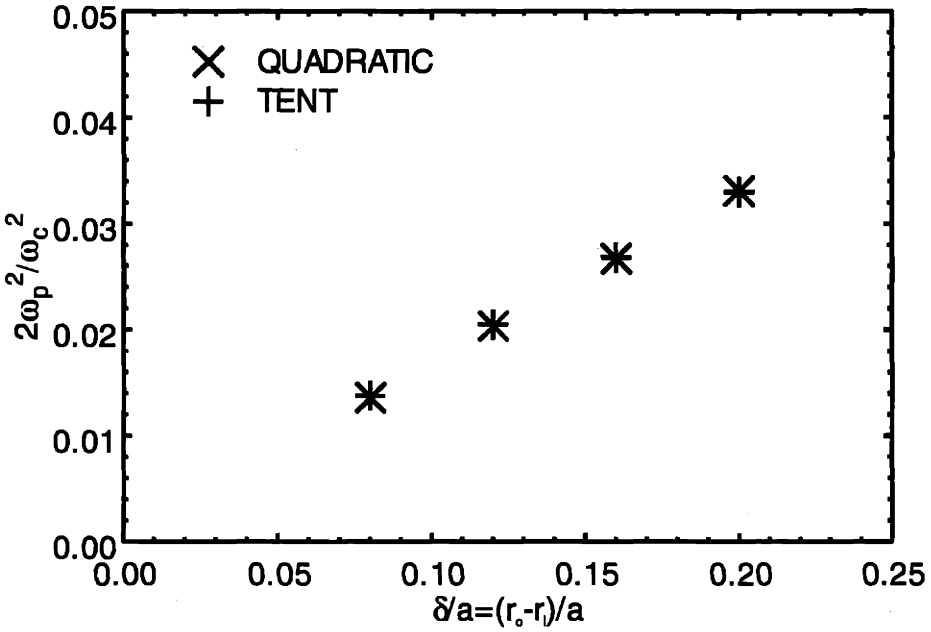

Fig. 6-5: Plots of $2\omega_p^2/\omega_c^2$ versus normalized annular beam width for quadratic and tent density functions centered at *r/a=0.8*.

the critical self-field parameter $2\omega_p^2/\omega_c^2 = 1/\Gamma_{max}$ versus δ/a for f_1 and f_2. In Fig. 6-5, we chose $\bar{r}/a = 0.8$ and $\alpha = 2\pi a/\gamma_b L = 1.0$. The calculated self-field parameters for the two different trial functions are nearly identical as shown in Fig. 6-5. The difference between the self-field parameters of the quadratic functions and their equivalent tent functions is about 1%. Notice that the critical self-field parameter for both functions decreases as δ/a decreases. This behavior is intuitively obvious, since the bunches of charge are radially compressed while keeping N_b fixed; hence, the electric field will rise due to the increase in radial beam density.

6.4 Rigid-Rotor Equilibrium

6.4.1 General Formulation

In the traveling-wave equilibrium model developed in Section 6.2, we specified the transverse density profile, $\sigma(r)$, and then calculated the self-consistent electric field, E^{self}, from Eq. (6.7). The angular velocity $\omega_b(r)$ was immediately determined from E^{self} by Eq. (6.9). In this Section, we will formulate the more difficult inverse problem of finding $\sigma(r)$ given $\omega_b(r)$, for the special case of rigid-rotor flow $\omega_b(r) = \omega_{b0} = \text{constant}$.

Rigid-rotor equilibrium is a well-known distribution, which has been studied in many different problems in beam physics (see, for example, Davidson, 1990, Chap. 3). This equilibrium has been experimentally verified for strongly focused electron clouds in traps (Driscoll, Malmberg, and Fine, 1988). In the case of an unbunched beam, $\alpha = \infty$, in a perfectly conducting pipe with a solenoidal magnetic focusing field, the rigid-rotor equilibrium is known to be a uniform density distribution (see, for example, Davidson, 1990, Chap. 3).

From Eq. (6.9), it is immediately clear that rigid-rotor flow is possible for the bunched beam equilibrium, if and only if the electric field inside of the beam is given by

$$E^{self} = -\tilde{E}r/a, \tag{6.17}$$

where $\tilde{E}$ is an unspecified electric field constant. In other the words, the electric field force, and hence, the magnetic field force, must be linear functions of r. This is the requirement imposed by the well-known Kapchinsky-Vladimirsky (K-V) distribution (Kapchinsky and Vladimirsky, 1959) for unbunched beams. Hence, the rigid-rotor equilibrium distribution developed in this section can be interpreted as the bunched beam generalization of the K-V distribution.

We should note that a density distribution, which satisfies (6.17), will have an outer radius but not an inner radius, such as the annular distributions of Section 6.3. This is obvious when we examine the plot of $\Gamma(r)$ in Fig. 6-2(b) for the annular beam distribution in Fig. 6-2(a). We note that $\Gamma(r)$, and hence, $E^{self}(r)$, reverses sign within the beam. Therefore, Eq. (6.17) could never be satisfied with an annular beam distribution.

Due to the lower bound limit on the electric field inside of the beam from Eq. (6.10), we obtain that

$$\left|\tilde{E}\right| \le \gamma_b \omega_c^2 m_e a/4e. \tag{6.18}$$

For a beam of radius r_b, i.e., for a beam with $\sigma(r)=0$ when $r_b \le r \le a$, the electric field profile must satisfy

$$E^{self} = \begin{cases} \tilde{E}\mu, & 0 \le \mu \le r_b/a, \\ \tilde{E}\eta(\mu), & r_b/a \le \mu \le 1, \end{cases} \tag{6.19}$$

where $\eta(\mu)$ is an unknown function which is defined outside of the beam and $\mu = r/a$, is the normalized radius. In order to have a physically relevant solution, we require that the electric field be continuous across the beam radius, $\eta(r_b/a)=1$.

From Eq. (6.7), we know that the electric field may be written as

$$E^{self}(\mu) = \sum_{m=1}^{\infty} E_m^{self} J_1(j_{0m}\mu) \tag{6.20}$$

where

$$E_m^{self} = -2\pi N_b e \gamma_b \sigma_m \coth(\pi j_{0m}/\alpha). \tag{6.21}$$

To proceed, we need to exploit the properties of the Dini series (see, for example, Watson, 1980, Chap. 18), which is a generalized form of the Fourier-Bessel series. For

example, when using the zeroes $\{j_{0m}\}$ as an argument of an expansion, the Fourier-Bessel series only allows expansion functions of the form $J_0(j_{0m}\mu)$. However, the Dini series allows one to expand in terms of $J_0(j_{0m}\mu)$, as well as, $J_1(j_{0m}\mu)$. The electric field coefficients E_m^{self} may be calculated from the Dini series (see, for example, Watson, 1980, Chap. 18) by

$$E_m^{self} = \frac{2}{J_1^2(j_{0m})}\int_0^1 d\mu\mu E^{self} J_1(j_{j0m}\mu). \tag{6.22}$$

Using Eqs. (6.19), (6.21), (6.22) and the well-known Bessel function relation series $\int_0^1 dx x^2 J_1(yx) = J_2(y)/y$ (see, for example, Watson, 1980, p. 132), we obtain the density coefficients for the rigid-rotor solution

$$\hat{\sigma}_m = \left|\frac{4e\tilde{E}}{\gamma_b\omega_c^2 m_e a}\right| \frac{\alpha\tanh(\pi j_{om}/\alpha)}{\pi^2 J_1^2(j_{om})}\left(\frac{\omega_c^2}{2\omega_p^2}\right)\left[\left(\frac{r_b}{a}\right)^2 \frac{J_2(j_{om}r_b/a)}{j_{om}} + \int_{r_b/a}^1 d\mu\mu\eta(\mu)J_1(j_{0m}\mu)\right], \tag{6.23}$$

where $\hat{\sigma}_m = \sigma_m a^2$.

As seen from Eq. (6.23), the density profile is dependent on two parameters, α and r_b/a. The self-field parameter $\left(2\omega_p^2/\omega_c^2\right)\left|\gamma_b\omega_c^2 m_e a/4e\tilde{E}\right|$ is then uniquely determined by the normalization constraint $2\pi\int_0^a dr r\sigma(r) = 1$.

The general solution to Eq. (6.23) for arbitrary α and r_b/a is unknown. The main difficulty in solving Eq. (6.23) is that $\eta(\mu)$, which is the normalized electric field outside of the beam, is unknown. Nevertheless, various numerical attempts have been made to solve Eq. (6.23), and we will now briefly describe one of them.

One such attempt starts by choosing α and r_b/a, and then expanding $\eta(\mu)$ in terms of polynomials,

$$\eta(\mu) = \eta_0 + \eta_1\mu + \eta_2\mu^2 + \ldots + \eta_K\mu^K, \tag{6.24}$$

where K is an integer and the coefficients $\{\eta_k\}$ are initially guessed. The density function is then computed from Eq. (6.23). For arbitrary coefficients $\{\eta_k\}$, one would find that the

solution to this density function would be unphysical, that is, there would be regions where $\sigma(r) < 0$. The coefficients would then be corrected in order to find a density, which minimizes the $\sigma(r) < 0$ regions. The problem with this technique is that finding a general method for calculating $\{\eta_k\}$ in a manner such that the system converges, is not known. The density profile tends to be very sensitive to changes in $\{\eta_k\}$, and hence, converging solutions are difficult to find.

While the general bunched beam rigid-rotor solution is unknown, we are still able to derive analytically two special cases solutions. We end this section with two solutions to the rigid-rotor problem: the 2-D unbunched beam and the 3-D large beam ($r_b/a = 1$).

6.4.2 Special Case: 2D Unbunched Beam

One of the special case rigid-rotor solutions, which can be solved from our formalism is the unbunched beam ($L \to 0$, $\alpha \to \infty$) case for arbitrary r_b/a. As we mentioned earlier, it is known that the rigid-rotor solution for this system is given by the uniform density function:

$$\sigma = \begin{cases} 1/\pi r_b^2 & 0 \le \mu \le r_b/a \\ 0 & r_b/a \le \mu \le 1 \end{cases}. \tag{6.25}$$

We will now demonstrate how our formalism can recover this result.

Using the asymptotic limit $\coth x \to 1/x$ when $x \to 0$, we can write the unbunched beam limit for the electric field in Eq. (6.7) as

$$E^{self} \to \frac{-4\pi N_b e a}{L} \sum_{m=1}^{\infty} \frac{\sigma_m J_1(j_{0m} r/a)}{j_{0m}}, \tag{6.26}$$

where the charge per unit length, $\lambda = -N_b e/L$, is assumed to be finite. By employing the well-known Bessel integral (see, for example, Watson, 1980, p. 132), $\int_0^1 dx x J_0(bx) = J_1(b)/b$, Eq. (6.26) becomes

$$E^{self} \to \frac{-4\pi N_b e a}{L} \left(\frac{a}{r}\right) \sum_{m=1}^{\infty} \sigma_m \int_0^{r/a} dx x J_0(j_{0m} x). \tag{6.27}$$

The final step involves using Eq. (6.3) to reduce Eq. (6.27) to the form

$$E^{self} \rightarrow \frac{-4\pi N_b e a}{L}\left(\frac{a}{r}\right)\int_0^{r/a} dx x\sigma(x). \tag{6.28}$$

We can find immediately from Eq. (6.28) that the only possible solution for $\sigma(r)$, which gives a linear radial dependence in E^{self}, is $\sigma(r) = \text{constant}$. After normalization, we recover the form in Eq. (6.25).

6.4.3 Special Case: 3-D Large Beam

A second rigid-rotor case, that is possible to solve analytically, is the 3-D large beam case, which corresponds to arbitrary α but with the beam radius equal to the conductor radius, $r_b/a = 1$. In the large beam limit, the integral on the right-hand side is precisely zero. Therefore, Eq. (6.23) becomes

$$\hat{\sigma}_m = \left|\frac{4e\tilde{E}}{\gamma_b \omega_c^2 m_e a}\right| \frac{\alpha \tanh(\pi j_{om}/\alpha)}{\pi^2}\left(\frac{\omega_c^2}{2\omega_p^2}\right)\frac{J_2(j_{om})}{J_1^2(j_{om}) j_{om}}. \tag{6.29}$$

Eq. (6.29) combined with Eq. (6.3) gives the exact density profile for the 3-D large beam rigid-rotor equilibrium.

We can obtain the self-field parameter, as mentioned before from the normalization criterion, $2\pi\int_0^a dr r\sigma(r) = 1$. Using the recurrence relation (see, for example, Watson, 1980, p. 17), $J_2(j_{0m}) = 2J_1(j_{0m})/j_{0m}$, and the previous Bessel integral relation, we find that

$$\left|\frac{\gamma_b \omega_c^2 m_e a}{4e\tilde{E}}\right| \frac{2\omega_p^2}{\omega_c^2} = \frac{4\alpha}{\pi}\sum_{m=1}^{\infty}\frac{tanh[\pi j_{0m}/\alpha]}{j_{0m}^3}. \tag{6.30}$$

By combining Eqs. (6.18) and (6.30), we find that

$$\frac{2\omega_p^2}{\omega_c^2} \le \frac{4\alpha}{\pi}\sum_{m=1}^{\infty}\frac{tanh[\pi j_{0m}/\alpha]}{j_{0m}^3}. \tag{6.31}$$

In the limit of an unbunched beam, $\alpha \rightarrow \infty$, and

$$\frac{2\omega_p^2}{\omega_c^2} \le 4\sum_{m=1}^{\infty}\frac{1}{j_{0m}^2} = 1 \tag{6.32}$$

which is the well-known Brillouin density limit (Brillouin, 1945) that we discussed in Chapter 3. In the limit of a strongly bunched beam, $\alpha \to 0$, we obtain the self-field parameter limit

$$\frac{2\omega_p^2}{\omega_c^2} \le \frac{4\alpha}{\pi}\sum_{m=1}^{\infty}\frac{1}{j_{0m}^3} \cong 0.103\alpha . \tag{6.33}$$

Notice that this self-field parameter is a factor about a factor of 3 smaller than the bunched beam limit in Eq. (3.33) in the NRCM model. This is attributed mainly to the inclusion of the internal space charge forces within the bunch.

The density coefficients in Eq. (6.29) can be rewritten with the help of Eq. (6.30) as

$$\hat{\sigma}_m = \frac{1}{2\pi}\frac{\tanh(\pi j_{om}/\alpha)}{J_1(j_{om})j_{0m}^2}\left(\sum_{m=1}^{\infty}\frac{tanh[\pi j_{0m}/\alpha]}{j_{0m}^3}\right)^{-1} . \tag{6.34}$$

In Fig. 6-6, we plot the large bunched beam rigid-rotor density distributions given by Eqs. (6.3) and (6.34) for four different values of α: a) $\alpha = 0.0$, b) $\alpha = 10.0$, c) $\alpha = 20.0$, and d) $\alpha = \infty$, which is the unbunched beam limit. Figure 6-7 shows a plot of the maximum value for the self-field parameter $2\omega_p^2/\omega_c^2$ versus α corresponding to Eq. (6.31). Also plotted is the 2-D unbunched beam limit given in Eq. (6.32).

6.5 Discussion

Unlike the NRCM and RCM models, which ignore the internal bunch forces, the RBDB model incorporates these forces in the transverse direction to establish a fluid equilibrium in the presence of a uniform magnetic focusing field. The RBDB model is an attempt to include finite bunch size effects in the bunched beam model, while maintaining enough simplicity to be an analytical and numerical tool. Although, the RBDB model is more advanced than the preceding models, it also has limitations which may prevent it from being a realistic model of a bunched beam.

One difficulty with the RBDB model, which also occurred in the NRCM and the RCM models, is that the longitudinal width of each bunch is assumed to be zero. In all three models this assumption will effect the self-field parameter limit, namely, it will decrease what the actual limit should be with finite bunch size. However, since the RBDB model includes the effect of the internal bunch forces, the zero longitudinal width

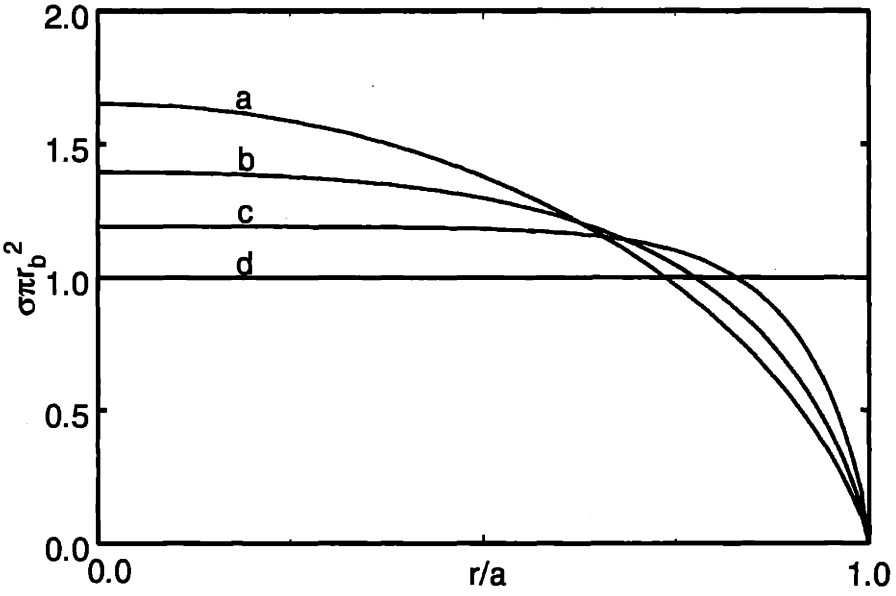

Figure 6-6: Plots of the large bunched beam ($r_b = a$) rigid-rotor density distributions given by Eqs. (6.3) and (6.34) for four different values of α: a) $\alpha = 0.0$, b) $\alpha = 10.0$, c) $\alpha = 20.0$, and d) $\alpha = \infty$, which is the unbunched beam limit.

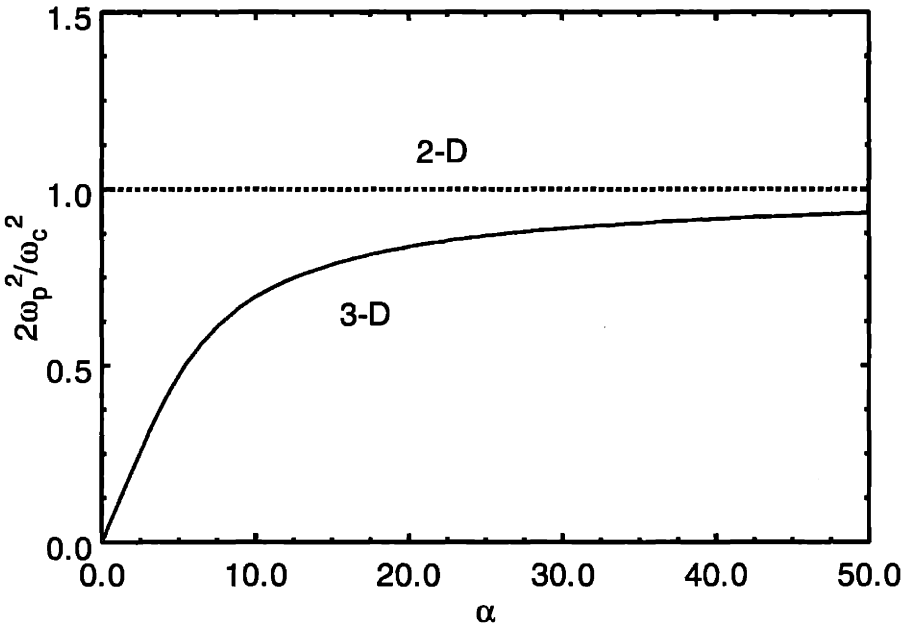

Figure 6-7: Plot of the maximum self-field parameter $2\omega_p^2/\omega_c^2$ (solid) for the large bunched beam rigid-rotor equilibrium as a function of $\alpha = 2\pi a/\gamma_b L$. Also shown is the Brillouin density limit $2\omega_p^2/\omega_c^2 = 1$ (dashed), which corresponds precisely to the unbunched rigid-rotor limit.

assumption will probably effect this model considerably more than the NRCM and the RCM models. Therefore, we should interpret the self-field parameter limit in Eq. (6.13), as a lower bound for what the actual limit would be when the longitudinal bunch size is considered to be non-negligible.

Another limitation of the RBDB model is that the beam bunches are assumed to be in radially symmetric equilibrium. This assumption allowed us to exploit the fact that all of the unknown functions, such as ω_b and E^{self}, are only functions of r. However, observations (Kyhl and Webster, 1956) on unbunched beams have shown that theoretical calculations (see, for example, Davidson, 1990, Chap. 6) and experimental azimuthally dependent instabilities, such as the diocotron instability, can exist. Radial and azimuthal stability analyses of the RBDB model could lead to a more stringent limit on the self-field parameter than the limit in Eq. (6.13). This is one possible area of further investigation with the RBDB model.

Chapter 7

Application of RBDB Model: Annular Beam HPM Experiments

In Chapter 6, we presented the RBDB model for the equilibrium and confinement of bunched annular beams. This model predicted the limit in Eq. (6.13) on the self-field parameter necessary for equilibrium and confinement. As in Chapter 5, we can reinterpret this limit as a current limit, and then apply this theory to actual annular electron beam experiments. In particular, we will apply the limit in Eq. (6.13) to three annular beam experiments, namely, the 1.3 GHz relativistic klystron amplifier (RKA) experiment at LANL (Fazio, *et al.*, 1994), the 1.3 GHz relativistic klystron oscillator (RKO) experiment at AFRL (Hendricks, *et al.*, 1998), and the 9.4 GHz backward wave oscillator (BWO) experiment at the University of New Mexico (Hegeler, Grabowski, and Schamiloglu, 1998).

All of the klystrons discussed in Chapter 5 utilized a pencil electron beam to produce high-power microwaves. However, klystrons and other sources may be designed to utilize an annular electron beam instead. One of the main reasons for going to such an alternative is to reduce the effect of the space charge limiting current (see, for example, Davidson, 1990, Ch. 9). It is well-known that for an unbunched thin annular electron beam in an infinite axial magnetic guide field, the maximum continuous current, or the space charge limiting current, which can propagate in a conductor pipe is given by (see, for example, Davidson, 1990, Ch. 9)

$$I_{SCL} = \frac{17kA}{2\ln[2a/(r_o + r_i)]}\left(\gamma_b^{2/3} - 1\right)^{3/2}, \tag{7.1}$$

where $\gamma_b = \gamma_{inj}$, the relativistic factor at injection and r_i (r_o) represents the inner (outer) radius of the annular beam.

Any residual current sent into the conductor which is above the space-charge limiting current, I_{SCL}, will be reflected in the opposite direction. Due to the geometric factor in Eq. (7.1), we note that $I_{SCL} \to \infty$, as $2a/(r_o + r_i) \to 1$. Hence, annular beams have the advantage of being able to propagate considerably more current than pencil beams. A higher current implies that the device is capable of producing higher power microwaves. The current limit in Eq. (7.1) is fundamentally different than the limit in Eq. (6.13). Essentially, the space-charge current limit is derived for continuous annular beams, which are propagating with an infinite magnetic field. Furthermore, the space-charge current limit completely ignores transverse beam motion, and is only involved with longitudinal motion. However, the limit in Eq. (6.13) is for a transverse bunched beam equilibrium with a finite magnetic field present.

We note that the relativistic factor γ for the beam inside of the conductor is different than γ_{inj} because of space-charge depression. The relativistic factor γ is determined by (see, for example, Davidson, 1990, Ch. 9)

$$(\gamma_{inj} - \gamma)(1 - \gamma^{-2})^{1/2} = \frac{2I_b}{17\,kA} ln\left(\frac{2a}{r_i + r_o}\right). \tag{7.2}$$

However, as we will show later, the difference between γ and γ_{inj} is a few percent for the typical parameters of annular beam high-power microwave experiments. Further, we will show that the RBDB confinement limit in Eq. (6.13), like the RCM confinement limit in Eq. (4.13), is approximately energy invariant for most experiments. Hence, the RBDB model is usually robust to experimental energy variations caused by space-charge depression.

In Section 7.1, we will provide a brief description of each of the three annular beam experiments. In Section 7.2, we will discuss how to apply the self-field parameter limit in Eq. (6.13) to these experiments. Finally, we will provide a discussion of the results in Section 7.3.

7.1 Recent Annular Beam High-Power Experiments

7.1.1 LANL 1.3 GHz Relativistic Klystron Amplifier

One example of a high-power annular beam device is the Los Alamos 1.3 GHz RKA experiment (Fazio, *et al.*, 1994), which has been developed as a directed energy application. This device can produce 500 MW of microwave power for 1 μs. A schematic of the RKA experiment is shown in Figure 7-1. The device is composed of three cavities, the input and output cavities for the microwaves, and a third intermediate (idler) cavity which improves bunching in the beam. All of the important parameters for the LANL RKA experiment are summarized in the first seven rows in Column 1 of Table 7-1.

The motivation for comparing the RKA experiment at LANL with our theory is that this experiment reported microwave pulse shortening, as well as indications of beam loss and anomalous beam halo formation (Fazio, *et al.*, 1994). Figure 7-2 shows a plot of the experimentally measured beam voltage, beam current, and output power as a function of time. Notice that that output microwave power shuts off, while the current is still ramping. In Section 7.3, we will utilize Eq. (6.13) to try to explain the occurrence of the microwave pulse shortening.

In an earlier paper (Carlsten, *et al.*, 1994), the LANL group provided an analysis of a modulated space-charge current limit due to the large potential depression for HPM sources, which they claimed may be responsible for the amount of microwave power which can be extracted in their RKA experiment. However, their current limit does not include the effect of beam confinement by magnetic focusing, and hence, may not explain the beam halo formation or the beam loss often associated with microwave pulse shortening. We will show that the RKA experiment is operating slightly above the effective self-field parameter limit in Eq. (6.13).

7.1.2 AFRL 1.3 GHz Relativistic Klystron Oscillator

Another annular beam high-power microwave source we have analyzed is the Air Force Research laboratory 1.3 GHz Relativistic Klystron Oscillator (RKO) experiment (Hendricks, *et al.*, 1998), which is shown schematically in Figure 7-3. The AFRL RKO is capable of producing over 1 GW of peak power for 300 ns. The important parameters for the AFRL RKO are listed in the second column of Table 7-1. The annular electron

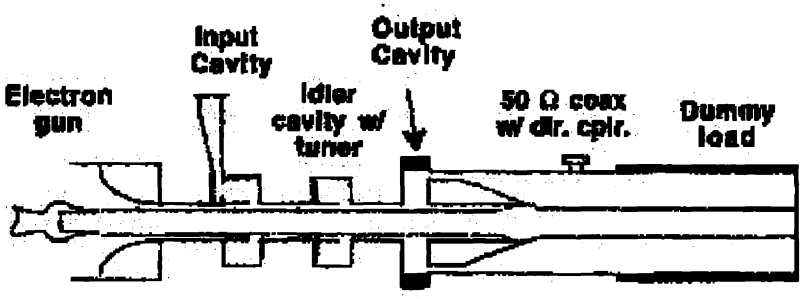

Figure 7-1: Schematic of the LANL RKA experiment (from Fazio, *et al.*, 1994)

Table 7-1: Parameters of Three Annular Beam HPM Devices

PARAMETER	RKA	RKO	BWO
f (GHz)	1.3	1.3	9.4
I_b (kA)	6.0	10.0	3.0
γ_b	2.1	2.0	1.7
B_0 (T)	0.5	0.8	2.0
r_i (cm)	2.70	6.60	0.90
r_o (cm)	3.20	7.10	1.15
a (cm)	3.65	7.65	1.28
α	0.54	1.20	1.83
$\left.\frac{8c^2 I_b}{\omega_c^2 a^2 I_A}\right\|_{exp}$	0.0133	0.0021	0.0045
$\left.\frac{8c^2 I_b}{\omega_c^2 a^2 I_A}\right\|_{cr}$	0.0126	0.016	0.059

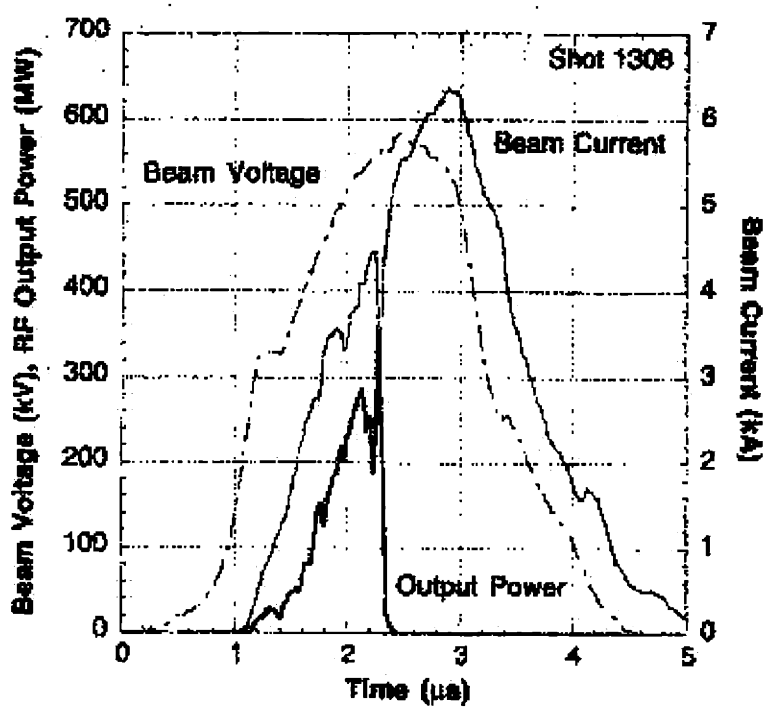

Figure 7-2: Plots of the beam voltage, beam current, and microwave output power as a function of time for LANL RKA experiment (from, Fazio, *et al.*, 1994). Notice that the output microwave power shuts off, while the beam current is still ramping.

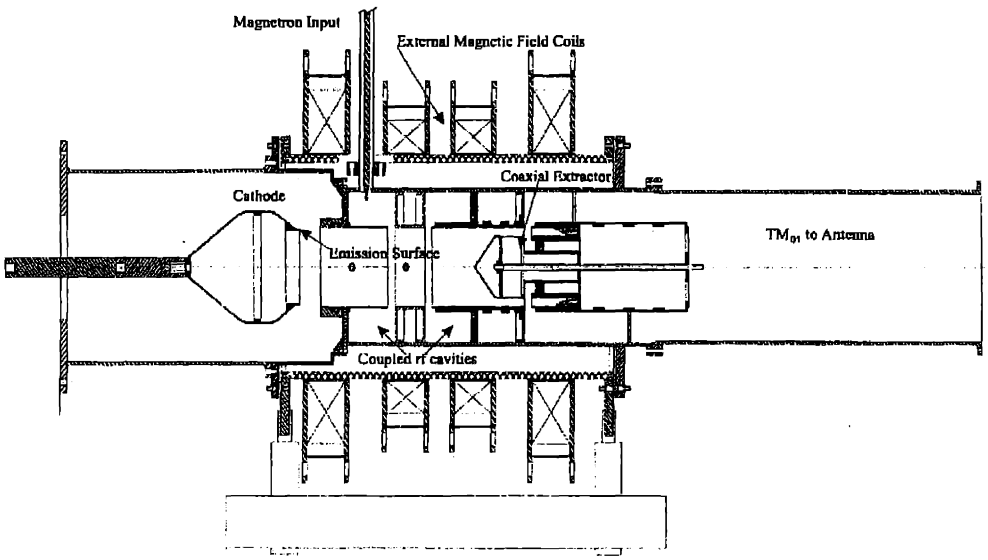

Figure 7-3: Schematic of the 1.3 GHz relativistic klystron oscillator experiment at the Air Force Research Laboratory (from Hendricks *et al.*, 1998).

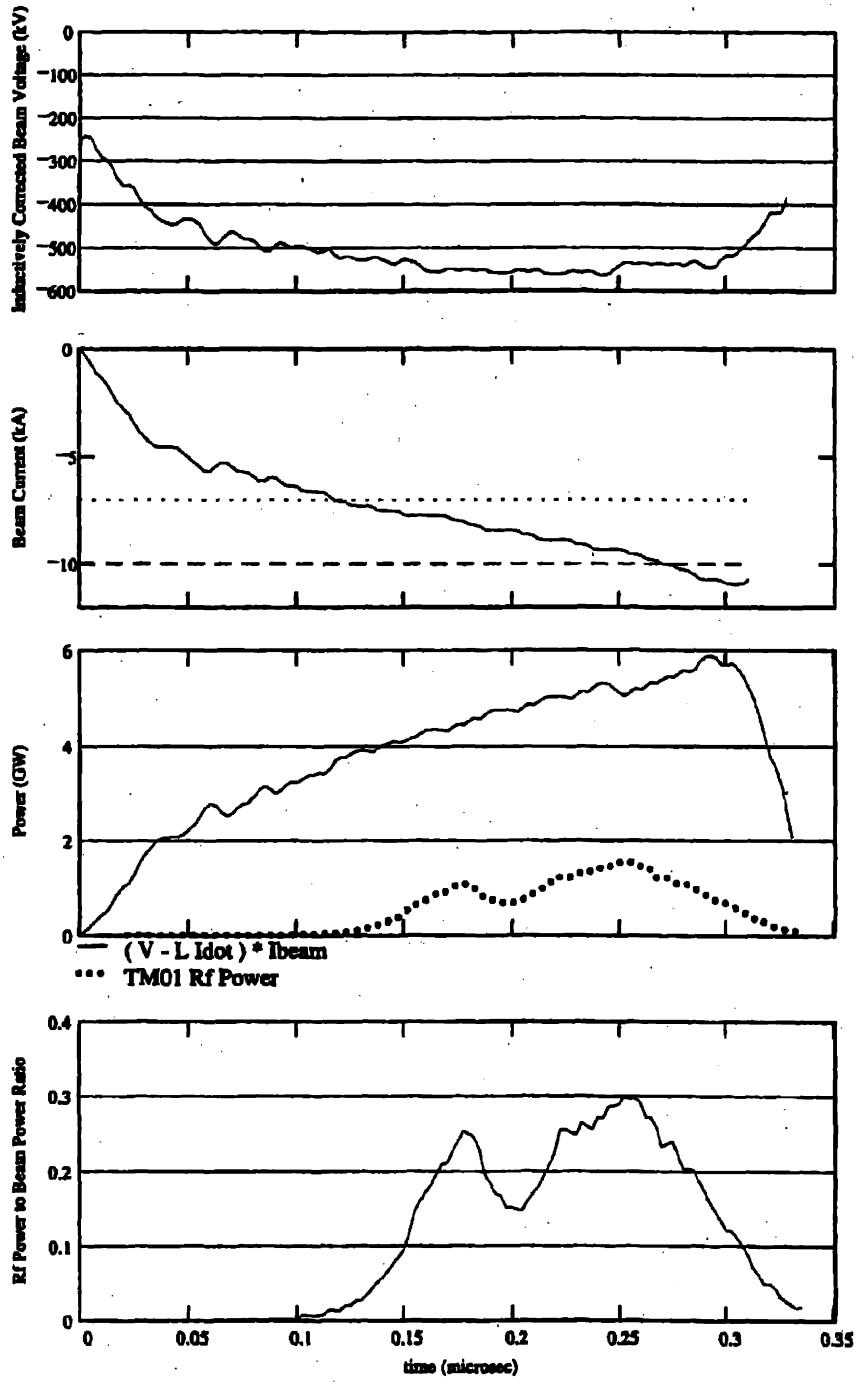

Figure 7-4: Plots of beam voltage, beam current, beam and rf power, and rf power to beam power ratio as functions of time for the 1.3 GHz relativistic klystron oscillator experiment at the Air Force Research Laboratory (from Hendricks *et al.*, 1998).

beam is emitted from the cathode, and then is velocity modulated by two intermediate cavity gaps. A third gap, called the extractor gap, acts as the beam dump and the rf extraction cavity. Figure 7-3 shows an input signal line for a magnetron, which is used to lock the RKO to a particular frequency at startup. The entire beam line is immersed in an axial magnetic focusing field of 0.8 T. Figure 7-4 shows experimental measurements of the beam voltage, beam current, beam and rf power, and rf power to beam power ratio as functions of time. Notice, in particular, that the rf power (third plot) does not shut off during the RKO current ramp, as it did for the LANL RKA experiment shown in Figure 7-2.

While this experiment observed negligible beam loss, it did observe an rf breakdown near the first gap. We anticipated that such an rf breakdown may have been caused by a small amount of beam being lost to the wall, which could stimulate an rf breakdown event. We will show in Section 7.2 that this experiment is operating well below the threshold given in Eq. (6.13). Hence, it is not clear whether the rf breakdown was caused by beam loss or potentially by a local surface breakdown event, which is completely unrelated to beam loss.

7.1.3 UNM 9.4 GHz Backward Wave Oscillator

The last annular beam device we have investigated is the 9.4 GHz Backward Wave Oscillator (BWO) developed at the University of New Mexico (Hegeler, Grabowski, and Schamiloglu, 1998). A schematic of the device is shown in Figure 7-5. Essentially, it consists of an annular electron beam, which is guided by an axial magnetic focusing field through a metal slow-wave structure and into a beam dump. The slow-wave structure is a rippled wall, which causes the beam to bunch. The relevant parameters for this device are listed in the third column of Table 7-1.

The bunched beam is coherently interacting with an backward electromagnetic wave, that is the phase velocity of the wave is in the direction of beam propagation, but its group velocity is opposite to the beam motion. The UNM BWO is designed to produce 1 GW of microwave power, but large beam loss and substantial background plasma formation limit the microwave pulse to under 100 MW. The microwave pulse may shut off, after 50 ns, despite the fact that the cathode is ramping current for around

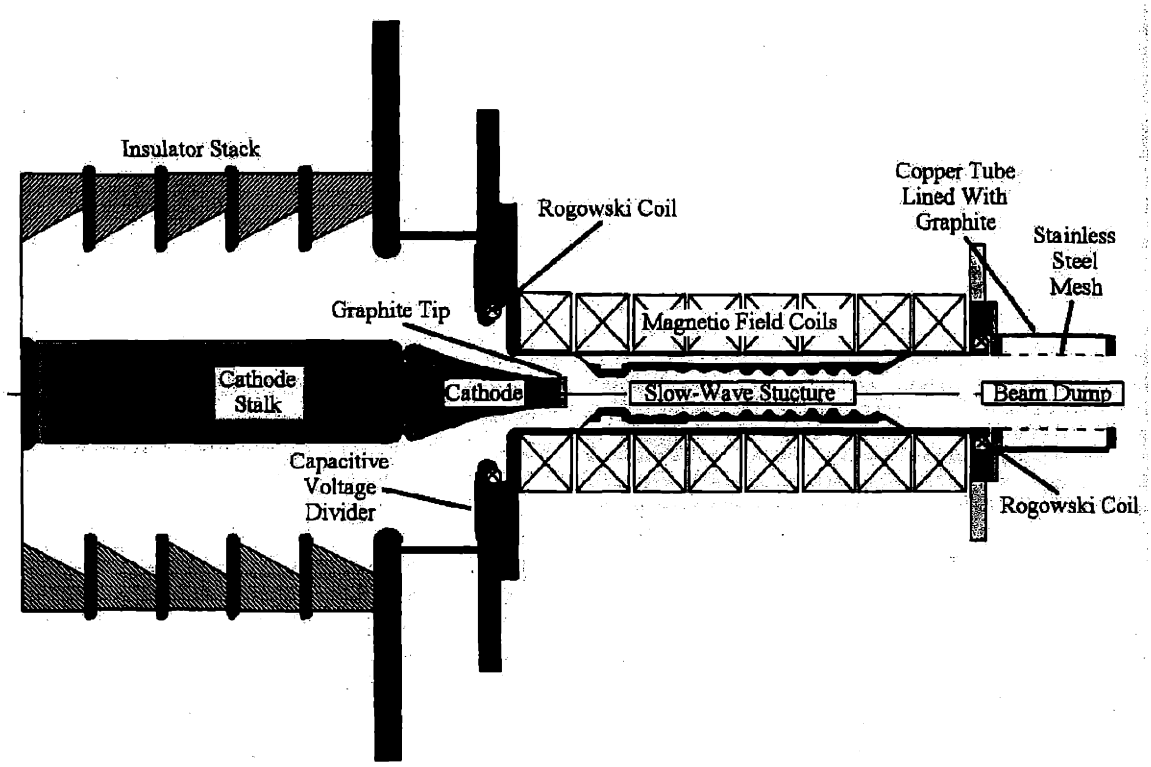

Figure 7-5: Schematic of the 9.4 GHz backward wave oscillator at the University of New Mexico (from Hegeler, Grabowski, and Schamiloglu, 1998).

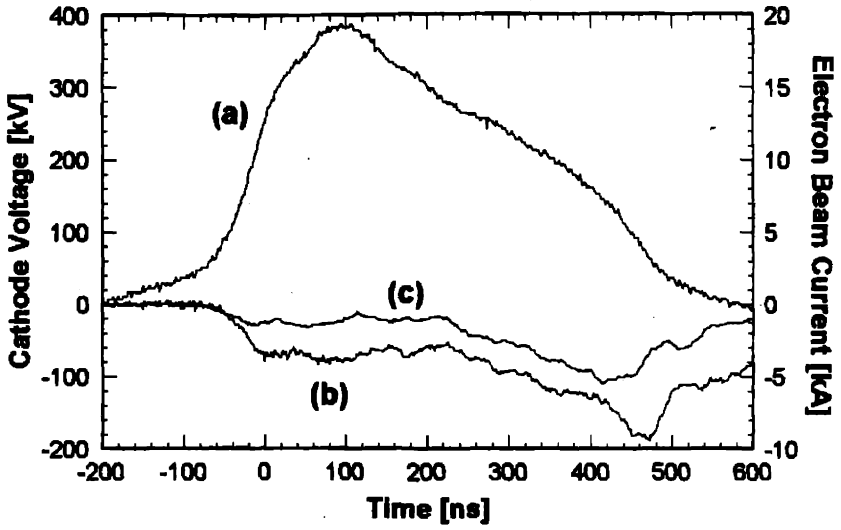

Figure 7-6: Plots of (a) cathode voltage, (b) emitted current, and (c) transmitted current for the 9.4 GHz backward wave oscillator at the University of New Mexico (from Hegeler, Grabowski, and Schamiloglu, 1998).

600 ns. Figure 7-6 shows an experimental plot of the cathode voltage, the transmitted current, and the emitted current as a function of time. Notice that over half of the emitted current has not been transmitted. The UNM group attributes this beam loss to two reasons. First,part of the beam has collected at alternate anode before it reaches the slow-wave structure. Second, another part of the beam has scraped the inner wall of the slow-wave structure. This effect causes an enormous amount of background plasma to be formed, and shorts the microwave pulse.

Although the BWO contains a slow-wave structure instead of a smooth wall as its conducting boundary, we attempted to model this system using the RBDB theory. In general, there will be fully electromagnetic interactions with a non-uniform conductor present. We guessed that an effective electrostatic beam-wall interaction could be approximated in this system by setting a equal to the average radius of the wall in the RBDB model. As we will show in Section 7.3, the RBDB model predicts that the experiment is operating well below the critical confinement limit in Eq. (6.13). Hence, the RBDB model will prove insufficient for predicting beam loss in the UNM BWO.

7.2 Application of RBDB Model to Experiments

In this section, we will apply the bunched annular beam equilibrium theory discussed in Chapter 6 to three experiments, namely, the 1.3 GHz RKA experiment at LANL (Fazio, *et al.*, 1994), the 1.3 GHz RKO experiment at AFRL (Hendricks, *et al.*, 1996), and the 9.4 GHz BWO experiment at the University of New Mexico (Hegeler, Grabowski, and Schamiloglu, 1998). As seen from Table 7-1, all three of these experiments utilize an annular electron beam whose transverse size is comparable to the conductor wall. If the operating parameters of an annular beam experiment are such that Eq. (6.13) is violated, then the beam would not be in equilibrium once the beam is fully bunched during high-power operation of the experiment. Equilibrium could be achieved if the beam reduces space charge by a loss mechanism to the surrounding conducting wall, and such a mechanism is known to be a cause of microwave pulse shortening.

We use the quadratic density function in Eq. (6.15) to approximate the radial density distribution. The space charge limit is then numerically computed by using Eq. (6.13) and the relevant experimental data provided in Table 7-1.

By using similar ideas when applying the RCM model to experiments, the parameters α and $2\omega_p^2/\omega_c^2$ can be further expressed in terms of experimental values, such as the average beam current I_b, the magnetic field B_0, the device frequency f, and the relativistic mass factor of the beam $\gamma_b = (1-\beta_b^2)^{-1/2}$. Since $v_b = fL$ and $I_b = N_b ef$, we can rewrite the dimensionless parameters α and $2\omega_p^2/\omega_c^2$ as $\alpha = 2\pi af/c(\gamma_b^2-1)^{1/2}$ and $2\omega_p^2/\omega_c^2 = 8c^2 I_b/\omega_c^2 a^2 I_A$, where $I_A = (\gamma_b^2-1)^{1/2} m_e c^3/e \approx 17kA(\gamma_b^2-1)^{1/2}$ is the Alfven current.

Using the experimental values from Table 7-1, we compare the self-field parameter, $2\omega_p^2/\omega_c^2$, for each experiment with the critical self-field parameter predicted by the theory for the same value of α. We note that the value of γ_b chosen for modeling each of the experiments corresponds to the injected energy, i.e. $\gamma_b = \gamma_{inj}$, and not the value γ due to space-charge depression [see discussions related to Eq. (7.2)].

From Eq. (7.2) and Table 7-1, we find that for the case of the LANL RKA, the difference between γ_{inj} and γ is approximately 6%. However, the critical result of our theory, namely the effective space-charge density limit in Eq. (6.13), is essentially unaffected by the choice of γ_b in the typical parameter ranges for HPM sources, as we will now demonstrate.

In Eq. (6.13), we note that the left-hand side is proportional to $(\gamma_b^2-1)^{-1/2}$. From Eq. (6.12), we find that $\Gamma(r)$ has a factor of $(\gamma_b^2-1)^{1/2}$ outside of the power series, as well as a nonlinear dependence on $(\gamma_b^2-1)^{1/2}$ in each of the $coth(\pi j_{on}/\alpha)$ functions. As seen from Table 1, a typical range for α is $0.5 < \alpha < 2.0$, and hence $coth(\pi j_{on}/\alpha) \cong 1.0$ to within 0.1%. Therefore, $(\gamma_b^2-1)^{1/2}$ may be factored out of Eq. (6.13) to a very good approximation, and the theory becomes invariant for choice of γ_b.

For the LANL RKA experiment (Fazio, *et al.*, 1994), $\alpha \approx 0.54$ and $2\omega_p^2/\omega_c^2\big|_{exp} \approx 0.0133$ during the maximum current operation of 6 kA, which is close to the maximum current value shown in Figure 7-2. Using Eq. (6.13), we obtain the theoretical space-charge limit of $2\omega_p^2/\omega_c^2\big|_{crit} \approx 0.0126$, which implies that the bunched beam is not in equilibrium. One way for the beam to reach equilibrium is by beam loss to the conductor wall, thereby reducing the value of $2\omega_p^2/\omega_c^2\big|_{exp}$ such that it equals $2\omega_p^2/\omega_c^2\big|_{crit}$. This may be the explanation of the anomalous beam halo and the consequential beam loss, which were both observed in the RKA experiment (Fazio, *et al.*, 1994). Assuming that beam loss corresponds to the beam trying to reach bunched equilibrium as discussed in Chapter 6, a simple estimate on the amount of beam current loss may be made, namely,

$$\%\ \text{beam current loss} = \frac{2\omega_p^2/\omega_c^2\big|_{exp} - 2\omega_p^2/\omega_c^2\big|_{crit}}{2\omega_p^2/\omega_c^2\big|_{exp}}. \tag{7.3}$$

In this case, the predicted percentage of beam current loss would be about 5%. The authors have only used one publication (Fazio, *et al.*, 1994) as a source of information for the RKA experiment. However, a beam current loss measurement was not available in this paper with which to compare the estimate from Eq. (7.3).

We note that according to Figure 7-2, the microwave pulse actually shorts out closer to 5 kA. While the reason for this is unknown, it could potentially be caused by radial or azimuthal instabilities, which would lower the threshold in Eq. (6.13)

For the AFRL RKO experiment (Hendricks, *et al.*, 1996), $\alpha \approx 1.2$ and $2\omega_p^2/\omega_c^2\big|_{exp} \approx 0.0021$. The theoretical space-charge limit for the RKO experiment is given by $2\omega_p^2/\omega_c^2\big|_{crit} \approx 0.0161$, hence this experiment is operating well-below the space charge limit. This result agrees with the fact that no beam loss was observed in the RKO experiment (Hendricks, *et al.*, 1996). The rf breakdown observed at the first gap remains to be investigated.

For the University of New Mexico BWO experiment (Hegeler, Grabowski, and Schamiloglu, 1998), $\alpha \approx 1.83$ and $2\omega_p^2/\omega_c^2\big|_{exp} \approx 0.0045$, whereas the corresponding theoretical limit is given by $2\omega_p^2/\omega_c^2\big|_{crit} \approx 0.059$. This implies that the RBDB equilibrium model cannot account for the observed beam current loss in the BWO experiment (Hegeler, Grabowski, and Schamiloglu, 1998).

In both of the AFRL RKO and the UNM BWO experiments, the experimental values of $2\omega_p^2/\omega_c^2$ are an order of magnitude lower than the corresponding theoretical limits for bunched annular beam confinement. Hence, if the beam were to reach a bunched equilibrium, it will be well below the theoretical space-charge limit for the equilibrium to exist.

7.3 Discussion

We have shown that the parameters for an annular beam experiment (i.e., average beam current, magnetic field strength, etc.) may be used to calculate the relevant parameters in the RBDB model. In doing so, a self-consistent equilibrium fluid model for a bunched annular beam in an experiment may be established. The quadratic function was used to numerically model the annular beams of three high-power microwave experiments, the LANL 1.3 GHz RKA, the AFRL 1.3 GHz RKO, and the University of New Mexico's 9.4 GHz BWO.

The LANL RKA experiment (Fazio, *et al.*, 1994) was found to be operating slightly above the critical space-charge limit for bunched beam equilibrium. Operation above the critical limit may have caused a percentage of the beam current to be lost to the wall, which in turn could lead to microwave pulse shortening. However, as we saw in Figure 7-2, the microwave pulse may have shorted out, at an even earlier point in the current ramp. The reason for this is not known, but could be related to instabilities in the equilibrium model, for which we have not yet analyzed.

The AFRL RKO and University of New Mexico BWO experiments (Hendricks, *et al.*, 1996; Hegeler, Grabowski, and Schamiloglu, 1998) were both found to be operating well below the critical space-charge limit predicted by Eq. (6.13). This result agrees with the successful beam transport in the AFRL RKO experiment, but does not agree with the

observed beam loss and microwave pulse shortening in the UNM BWO experiment. While the bunched annular beam in the BWO experiment is well confined from the viewpoint of an equilibrium theory, the stability of the bunched beam equilibria remains to be determined in order to answer the question of whether or not beam loss occurs in this experiment. This will be an important subject for further investigation.

Chapter 8

Development of the PFB3D Code

In Chapters 2-7, we developed simplified models of bunched beams, i.e., the NRCM, RCM and the RBDB models, and applied them to actual high-power microwave experiments. From these models, we derived fundamental limits on the self-field parameter for the system. The predictions of these limits can be very useful for designing high-power microwave sources, such as klystrons. However, the simplifications made in these models, such as single-particle approximation and cold-fluid theories, prevents us from examining the actual evolution of a bunched beam with many particles. A unique approach to model a bunched beam with many particles is through extensive, self-consistent, numerical simulations. This has led us to develop a new code called PFB3D (**P**eriodic **F**ocused **B**eam in **3-D**), which utilizes the Green's function formulation in Chapter 2 to self-consistently calculate the electric fields between particles in the bunch with the conductor wall present.

In Section 8.1, we provide a brief introduction to the PFB3D code and discuss its current capabilities. Section 8.2 will be a mathematical overview of how the code solves the dynamics of the particles. Section 8.3 we will show a "superconvergent" technique for calculating the electric and magnetic fields inside of the pipe using the Green's funtion. In Section 8.4, we will show initial results for modeling of the LANL RKA (Fazio, *et al.*, 1994) experiment with the PFB3D code. Lastly, in Section 8.5, we will mention what future capabilities we hope to add to the PFB3D code.

8.1 Introduction

The PFB3D code is based on three assumptions about the entire system: (1) the

beam is periodic, with periodic spacing L, (2) the beam may be modeled electrostatically by moving into the rest frame of the beam, and (3) the surrounding conductor wall is cylindrical and perfectly conducting. The electrostatic Green's function theory developed in Chapter 2 is a unique approach to model the system self-consistently when assumptions (2) and (3) are true. Assumption (1) was added since most high-power microwave sources use periodic beams, but it is not a requirement for the code to operate.

As we mentioned previously, the PFB3D code is a many-body code. However, it is obvious that we can not model the total number of particles, $\sim 10^{10}$, in a real beam bunch. Hence, we need to use macroparticles to simulate the dynamics of the electron bunch. Each macroparticle represents N number of electrons in an actual bunch. Figure 8-1 shows a schematic of two periodic macroparticles, labeled i and j, which form periodic bunches inside of a perfectly conducting cylinder. For a typical simulation with 10^3-10^4 macroparticles, N~10^6-10^7.

We will discuss in Section 8.2, how the code calculates exactly the interaction between two macroparticles, i and j. However, we note that for M macroparticles, the number of electric field calculations per time step scales as M^2, which can severely limit the number of macroparticles used in a simulation. Nevertheless, simulation results suggest that for typical parameters of bunched beam experiments, M=10^3-10^4 may be accurate enough to uncover large scale beam dynamics. We will discuss more about the appropriate number of macroparticles in Section 8.3.

The PFB3D code is currently operating with a constant magnetic focusing field present. This can easily be upgraded to handle periodic magnetic focusing, such as PPM focusing. Also, the code is not limited to periodic solenoidal focusing. It can be programmed to incorporate periodic quadrupole magnetic focusing, such as a periodic FODO (Focusing-Off-Defocusing-Off) lattice, which is typically found in particle accelerators (see, for example, Reiser, 1994, Chap. 3-4).

One of the interesting aspects of the PFB3D code is that it allows particles to be lost to the conductor wall. The code keeps an inventory of all of the macroparticles lost and their basic properties, such as kinetic energy and canonical angular momentum. The way

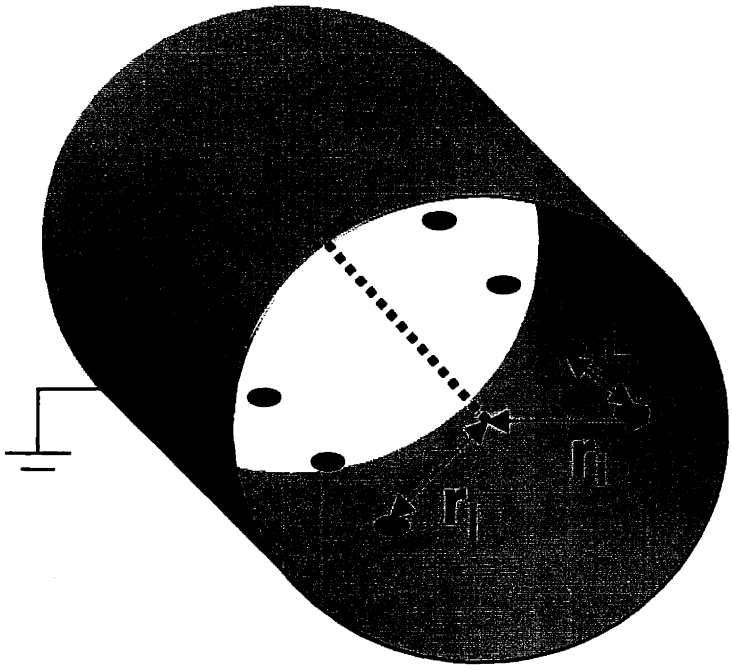

Figure 8-1: Schematic of two periodic macroparticles forming a bunch, with periodic spacing L, labeled i and j inside of a perfectly conducting cylinder. Note that for typical simulations the number of macroparticles is much larger.

the code is currently structured, when a particle hits the wall it is lost for the rest of the simulation. The PFB3D code does not incorporate secondary emission algorithms which calculate the number of new macroparticles generated, when a macroparticle hits the wall. Nevertheless, keeping track of the percentage of beam loss is important in making predictions for experiments.

8.2 Mathematical Formulation

The particle orbits are calculated by integrating the equations of motion in the laboratory frame, which are derived from the many-body Hamiltonian

$$H=\sum_{i=1}^{M}\sqrt{M^2c^4+\left(c\mathbf{P}_i-Q\mathbf{A}^{ext}-Q\mathbf{A}_i\right)^2}+\sum_{i=1}^{M}Q\phi_i\,. \tag{8.1}$$

where M and Q are the mass and charge of each macroparticle, $\mathbf{P}_i$ is the canonical momentum of the i^{th} macroparticle, and $\mathbf{A}^{ext}$ is the external vector potential for focusing. The electric potential acting on the i^{th} macroparticle due to the macroparticles interacting with each other and the wall is self-consistently computed and is given by,

$$\phi_i=\phi_i^{self}\left(\mathbf{r}_i\right)+\sum_{j\neq i}\phi_{ij}^{int}\left(\mathbf{r}_i;\mathbf{r}_j\right), \tag{8.2}$$

where the one particle self-potential is given in Chapter 4 by

$$\phi_i^{self}\left(r_i\right)=\frac{Q}{L}\left[ln\left(\alpha^2-\hat{r}_i^2\right)-2\sum_{n=1}^{\infty}\frac{K_0(n\alpha)I_0^2(n\hat{r}_i)}{I_0(n\alpha)}-4\sum_{n=1}^{\infty}\sum_{l=1}^{\infty}\frac{K_l(n\alpha)I_l^2(n\hat{r}_i)}{I_l(n\alpha)}\right], \tag{8.3}$$

and the two particle interaction potential follows from the theory in Chapter 3 by

$$\begin{aligned}\phi_{ij}^{int}\left(\mathbf{r}_i;\mathbf{r}_j\right)=&\frac{Q}{L}G_{2D}+\frac{4Q}{L}\sum_{n=1}^{\infty}cos\left[n\left(\hat{z}_i-\hat{z}_j\right)\right]\frac{I_0(n\hat{r}_<)}{I_0(n\alpha)}\left[I_0(n\alpha)K_0(n\hat{r}_>)-I_0(n\hat{r}_>)K_0(n\alpha)\right]\\&+\frac{8Q}{L}\sum_{n=1}^{\infty}\sum_{l=1}^{\infty}cos\left[n\left(\hat{z}_i-\hat{z}_j\right)\right]cos\left[l\left(\theta_i-\theta_j\right)\right]\frac{I_l(n\hat{r}_<)}{I_l(n\alpha)}\left[I_l(n\alpha)K_l(n\hat{r}_>)-I_l(n\hat{r}_>)K_l(n\alpha)\right],\end{aligned} \tag{8.4}$$

the "^" denotes the normalization by $2\pi/\gamma_b L$, $\alpha=2\pi a/\gamma_b L$, and

$$G_{2D}=\ln\left[\frac{a^2+\left(r_ir_j/a\right)^2-2r_ir_j\cos\left(\theta_i-\theta_j\right)}{r_i^2+r_j^2-2r_ir_j\cos\left(\theta_i-\theta_j\right)}\right]. \tag{8.5}$$

Using the Lorentz transformation in Chapter 4, we can derive the magnetic vector potentials from the electric potentials by

$$\mathbf{A}_i = \beta_b \phi_i \hat{\mathbf{e}}_z . \tag{8.6}$$

All of the potentials listed above are in keeping with the assumption that the longitudinal energy of the particles is much greater than its transverse energy.

Equation (8.1) combined with Hamilton's Equations,

$$\frac{d\mathbf{r}_i}{dt} = \frac{\partial H}{\partial \mathbf{P}_i}, \tag{8.7a}$$

$$\frac{d\mathbf{P}_i}{dt} = -\frac{\partial H}{\partial \mathbf{r}_i}, \tag{8.7b}$$

yield a closed 6M-dimensional set of nonlinear differential equations, which must be integrated simultaneously, as time evolves.

The PFB3D code is currently programmed to use the Fourth Order Runge Kutta (see, for example, Shampine, Allen, Jr., and Pruess, 1997, Chap. 6) method with fixed time step for integrating Eqs. (8.7a) and (8.7b). In order to ensure convergence, the same initial conditions are typically run with time steps that are varied by an order of magnitude. For a beam corresponding to an actual HPM experiment, time steps of the order $< 0.1\omega_L^{-1}$ are typically necessary to capture the majority of the significant dynamics in the beam.

8.3 Superconvergent Methods

When numerically implementing functions of a few variables which have infinite or even doubly-infinite summations, such as in Eqs. (8.3) and (8.4), optimizing the convergence rates of these functions is of great importance. This is especially true when dealing with sinusoidal expansions, which may have very slow rates of convergence. Trying to evaluate the potentials in Eqs. (8.3) and (8.4) may require thousands or even tens of thousands of terms, depending on where the function is being evaluated In this Section, we will show how to improve convergence of Eqs. (8.3) and (8.4), and discuss how these numerically improved functions are utilized in the PFB3D code.

The convergence problems in Eq. (8.4) are caused by two divergences in $\phi_{ij}^{int}(\mathbf{r}_i;\mathbf{r}_j)$. Since $\phi_{ij}^{int}(\mathbf{r}_i;\mathbf{r}_j)$ physically represents the electrostatic potential at $\mathbf{r}_i$ due to the periodic

macroparticle at $\mathbf{r}_j$ inside of the cylinder, we know that one of the divergences will be of the form $Q/|\mathbf{r}_i - \mathbf{r}_j - nL\hat{\mathbf{e}}_z|$ as $\mathbf{r}_i - \mathbf{r}_j - nL\hat{\mathbf{e}}_z \to 0$.

Another divergence in $\phi_{ij}^{int}(\mathbf{r}_i;\mathbf{r}_j)$, which is less obvious, is due to the presence of the conductor wall. When a macroparticle gets close to the conductor wall, i.e., $|\mathbf{r}_j| \to a$, there will be a large buildup of induced surface charge in that region. While the induced surface charge is spread over the conductor, it will have a very high density in the vicinity of $\mathbf{r}_j$. The induced surface charge behaves like a periodic pseudo-image charge, with a charge equal to $-Q$, and with a location at

$$\mathbf{r}_{pseudo} \cong (2a - r_j)\hat{\mathbf{e}}_{\mathbf{r}_j}. \tag{8.8}$$

The pseudo-image charge effect is illustrated in Figure 8-2. When $\mathbf{r}_i - \mathbf{r}_j - nL\hat{\mathbf{e}}_z \to 0$ as well, $\phi_{ij}^{int}(\mathbf{r}_i;\mathbf{r}_j)$ will be of the form $Q/|\mathbf{r}_i - \mathbf{r}_j - nL\hat{\mathbf{e}}_z| - Q/|\mathbf{r}_i - \mathbf{r}_{pseudo} - nL\hat{\mathbf{e}}_z|$.

The self-potential $\phi_i^{self}(r_i)$ in Eq. (8.3) suffers from the second divergence problem, i.e., $|\mathbf{r}_j| \to a$, since this potential precisely represents the interaction of the beam with the induced image charge, and $\mathbf{r}_i = \mathbf{r}_j - nL\hat{\mathbf{e}}_z$ when calculating $\phi_i^{self}(r_i)$.

The essence of the superconvergent methods is to remove out the divergences in these potentials due to the real and image charges, in such a way as to improve the accuracy and convergence rates of the potentials. We will demonstrate the superconvergent methods on $\phi_{ij}^{int}(\mathbf{r}_i;\mathbf{r}_j)$, and then show how to use them for $\phi_i^{self}(r_i)$.

The superconvergent method begins by implementing the well-known relation (see, for example, Gray and Mathews, 1952, p. 101),

$$\begin{aligned} K_0\left(n|\mathbf{r}_{\perp i} - \mathbf{r}_{\perp j}|\right) &= K_0\left(n\sqrt{\hat{r}_i^2 + \hat{r}_j^2 - 2\hat{r}_i\hat{r}_j\cos(\theta_i - \theta_j)}\right) \\ &= I_0(n\hat{r}_<)K_0(n\hat{r}_>) + 2\sum_{l=1}^{\infty}\cos(\theta_i - \theta_j)I_l(n\hat{r}_<)K_l(n\hat{r}_>), \end{aligned} \tag{8.9}$$

where $\perp$ represents the transverse component of the vector. We can therefore immediately rewrite $\phi_{ij}^{int}(\mathbf{r}_i;\mathbf{r}_j)$ as

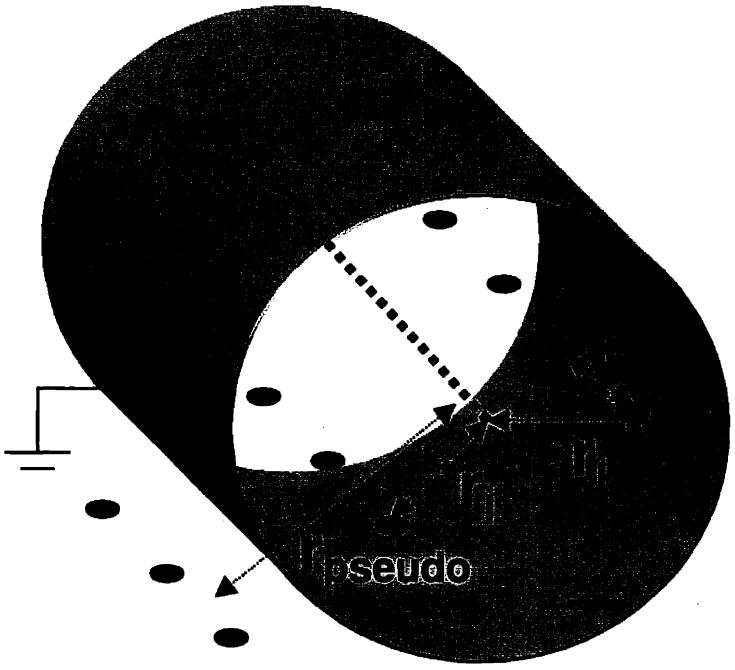

Figure 8-2: Schematic of two periodic macroparticles, i and j, forming a bunch, with periodic spacing L, and a periodic pseudo-image macroparticle which approximates the induced surface charge by macroparticle j.

$$\phi_{ij}^{int}(\mathbf{r}_i;\mathbf{r}_j)=\frac{Q}{L}G_{2D}+\frac{4Q}{L}\sum_{n=1}^{\infty}cos\left[n(\hat{z}_i-\hat{z}_j)\right]\left\{K_0(n|\mathbf{r}_i-\mathbf{r}_j|)\right.$$
$$\left.-\frac{I_0(n\hat{r}_i)I_0(n\hat{r}_j)K_0(n\alpha)}{I_0(n\alpha)}-2\sum_{l=1}^{\infty}cos\left[l(\theta_i-\theta_j)\right]\frac{I_l(n\hat{r}_i)I_l(n\hat{r}_j)K_l(n\alpha)}{I_l(n\alpha)}\right\}. \tag{8.10}$$

Secondly, we utilize another the well-known Bessel function series (see, for example, Gradshteyn and Ryzhik, 1994, p. 992),

$$\sum_{n=1}^{\infty}cos\left[n(\hat{z}_i-\hat{z}_j)\right]K_0(n|\hat{\mathbf{r}}_{\perp i}-\hat{\mathbf{r}}_{\perp j}|)=\frac{C}{2}+ln\left(\frac{|\hat{\mathbf{r}}_{\perp i}-\hat{\mathbf{r}}_{\perp j}|}{4\pi}\right)+\frac{\pi}{2|\hat{\mathbf{r}}_i-\hat{\mathbf{r}}_j|}$$
$$+\sum_{n=1}^{\infty}\left\{\frac{\pi}{2|\hat{\mathbf{r}}_i-\hat{\mathbf{r}}_j-2\pi n\hat{\mathbf{e}}_z|}+\frac{\pi}{2|\hat{\mathbf{r}}_i-\hat{\mathbf{r}}_j+2\pi n\hat{\mathbf{e}}_z|}-\frac{1}{2n}\right\}, \tag{8.11}$$

where $C=0.5772...$ is the Euler-Mascheroni constant.

Therefore, $\phi_{ij}^{int}(\mathbf{r}_i;\mathbf{r}_j)$ can be written in a form which removes out the divergences due to the real charges:

$$\phi_{ij}^{int}(\mathbf{r}_i;\mathbf{r}_j)=\frac{Q}{|\mathbf{r}_i-\mathbf{r}_j|}+\sum_{n=1}^{\infty}\left\{\frac{Q}{|\mathbf{r}_i-\mathbf{r}_j-nL\hat{\mathbf{e}}_z|}+\frac{Q}{|\mathbf{r}_i-\mathbf{r}_j+nL\hat{\mathbf{e}}_z|}-\frac{2Q}{nL}\right\}$$
$$+\frac{2QC}{L}+\frac{2Q}{L}ln\left(\frac{\alpha^2+(r_ir_j/\alpha)^2-2r_ir_jcos(\theta_i-\theta_j)}{16\pi^2}\right) \tag{8.12}$$
$$-\frac{4Q}{L}\sum_{n=1}^{\infty}\sum_{l=-\infty}^{\infty}cos\left[n(\hat{z}_i-\hat{z}_j)\right]cos\left[l(\theta_i-\theta_j)\right]\frac{I_l(n\hat{r}_i)I_l(n\hat{r}_j)K_l(n\alpha)}{I_l(n\alpha)}.$$

The first three terms in Eq. (8.12) represent the free space potential terms. The last term in brackets is necessary for convergence of the second and third free space terms. The second type of divergences, that is the divergences due to the wall, however, are still imbedded in the residual terms of Eq. (8.12). In order to accurately calculate $\phi_{ij}^{int}(\mathbf{r}_i;\mathbf{r}_j)$, these terms must be separated out like the free space terms.

Notice that by using Eqs. (8.10) and (8.11), we were able to effectively "uncover" the free space singularity terms. We can "uncover" the wall singularities due to the pseudo-image charges, as well, by using Eqs. (8.10) and (8.11) in a similar manner. By

specifying the location of the pseudo-image charges at location $\mathbf{r}_{pseudo}$ with charge $-Q$, we can rewrite Eq. (8.12) with the help of Eqs. (8.10) and (8.11) as:

$$\phi_{ij}^{ind}(\mathbf{r}_i;\mathbf{r}_j) = \sum_{n=1}^{\infty}\left\{\frac{Q}{\left|\mathbf{r}_i-\mathbf{r}_j-nL\hat{\mathbf{e}}_z\right|}-\frac{Q}{\left|\mathbf{r}_i-\mathbf{r}_{pseudo}-nL\hat{\mathbf{e}}_z\right|}\right\}$$

$$+\frac{2Q}{L}ln\left(\frac{\alpha^2+\left(r_i r_j/\alpha\right)^2-2r_i r_j cos\left(\theta_i-\theta_j\right)}{\left|\hat{\mathbf{r}}_i-\hat{\mathbf{r}}_{pseudo}\right|}\right) \tag{8.13}$$

$$+\frac{4Q}{L}\sum_{n=1}^{\infty}\sum_{l=-\infty}^{\infty}cos\left[n\left(\hat{z}_i-\hat{z}_j\right)\right]cos\left[l\left(\theta_i-\theta_j\right)\right]I_l\left(n\hat{r}_i\right)\left\{K_l\left(n\hat{r}_{pseudo}\right)-\frac{I_l\left(n\hat{r}_j\right)K_l\left(n\alpha\right)}{I_l\left(n\alpha\right)}\right\}.$$

In (8.13) we have chosen $\theta_{pseudo}=\theta_j$ and $z_{pseudo}=z_j$, since this is the physically sensible choice of angular and longitudinal placement for the pseudo-image relative to the charge which is inducing it.

The second term in brackets in Eq. (8.13) represents the free space potential due to the pseudo-image charge. The extra terms provide the correction due to the curvature of the boundary. This point is obvious since if the conductor was a plane instead of a cylinder, then the only terms present would be the ones in brackets, if the position of the pseudo-image charge is chosen appropriately.

We can perform a similar pseudo-image charge analysis on the self-potential in Eq. (8.3). In this case, it is appropriate to choose $\theta_{pseudo}=\theta_i$ and $z_{pseudo}=z_i$. However, care must be taken in our choice for the magnitude of the pseudo-image charge. Recall, that $Q\phi_i^{self}(r_i)$ represents the electrostatic potential energy evaluated at the macroparticle itself. In other words, taking the radial derivative of $Q\phi_i^{self}(r_i)$ yields the force on the macroparticle due to the wall. If we choose the magnitude of the pseudo-image charge to be $-Q$, then the force on the macroparticle would be twice the correct value. This is a well-known fact (see, for example, Griffiths, 1989, Ch. 3), which has been discussed in classical electrodynamics texts for the simpler case of a real charge in the vicinity of a perfectly conducting plane. The correct choice, in this case, for the pseudo-image charge magnitude is $-Q/2$. Applying a similar analysis using Eqs. (8.10) and (8.11) yields:

$$\phi_i^{self}(r_i) = -\sum_{n=1}^{\infty} \frac{Q}{\left|\mathbf{r}_i - \mathbf{r}_{pseudo} - nL\hat{\mathbf{e}}_z\right|} - \frac{QC}{L} + \frac{Q}{L} ln\left[\frac{16\pi^2\left(\alpha^2 - \hat{r}_i^2\right)}{\left(\hat{r}_{pseudo} - \hat{r}_i\right)^2}\right]$$
$$+ \frac{2Q}{L}\sum_{n=1}^{\infty}\sum_{l=-\infty}^{\infty} I_l(n\hat{r}_i)\left\{K_l(n\hat{r}_{pseudo}) - \frac{I_l(n\hat{r}_j)K_l(n\alpha)}{I_l(n\alpha)}\right\}. \tag{8.14}$$

There is freedom in choosing r_{pseudo}, since Eq. (8.8) must only be satisfied in the limit $r_j \to a$. We should add the caveat that r_{pseudo} must also be chosen such that $r_{pseudo} > a$, since the concept of an image charge is only valid when it exists in the conductor. In general, r_{pseudo} can be any function of r_j which satisfies the above requirements.

We have done preliminary tests with different functions for $\mathbf{r}_{pseudo}$, to check the convergence rates of Eq. (8.13) compared to Eq. (8.12), which does not use the pseudo-image charges. The convergence problem is especially important for the last terms in Eqs. (8.12) and (8.13), which has a doubly-infinite series involving sinusoidal functions and, in general converges very slowly. One possible choice for $\mathbf{r}_{pseudo}$ is to make Eq. (8.8) always true, i.e.,

$$\mathbf{r}_{pseudo} \equiv \left(2a - r_j\right)\hat{\mathbf{e}}_{\mathbf{r}_j}. \tag{8.15}$$

This choice does reduce the number of terms necessary for convergence of the doubly-infinite series in Eqs. (8.13) and (8.14) by at least a factor of three or four compared to their original series in Eqs. (8.12) and (8.11). However, there is an even better choice for $\mathbf{r}_{pseudo}$, which is actually motivated on physical grounds.

We know from electrostatics that for a rod of charge at a radius r inside of a cylinder of radius a, there will be an image rod with equal and opposite charge at a radius a^2/r. Choosing this to be the location of our image-charge, namely,

$$\mathbf{r}_{pseudo} \equiv \left(a^2/r_j\right)\hat{\mathbf{e}}_{\mathbf{r}_j} \tag{8.16}$$

actually results in much higher convergence, possibly a factor of three or four times better than the choice in Eq. (8.15). The PFB3D uses the superconvergent method that we have just discussed. The choice of the pseudo-image charge corresponds to Eq. (8.16).

The code actually evaluates the electric fields produced by Eqs. (8.13) and (8.14), which further reduces the level of inaccuracies from numerical differentiation. The electric fields also have singularities present, which correspond to the singular terms in the potentials. The PFB3D code evaluates the electric field contributions from the singular terms as the code is running. The terms in the electric fields corresponding to the derivatives in Eqs. (8.13) and (8.14), which involve the doubly-infinite series are evaluated on a mesh before the program begins. It is possible to get extremely good accuracies (1 part in 10^7) for the doubly-infinite series, since the series are smooth and, typically, slowly varying everywhere inside of the conductor.

8.4 Preliminary Simulation of the LANL RKA

In this Section, we discuss some results on a simulation of the Los Alamos RKA experiment (Fazio, *et al.*, 1994), which was discussed in Chapter 7. There are certain aspects of the code, such as the integration scheme and the electric field mesher, which are still being validated. Hence, the results presented in this section, are still preliminary.

The simulation was done with the PFB3D code operating in a 2-1/2 dimensional format. That is, we loaded the periodic macroparticles into a bunch with zero longitudinal thickness. All of the macroparticles were given the same longitudinal momentum. This type of setup is a many-particle approach to the RBDB model, which we presented in Chapter 6. We assume that the only longitudinal force acting on a macroparticle, $Qv_r \times B_\theta^{self}/c$, is small since the beam is assumed to non-relativistic in the transverse direction. Hence, the bunch maintains zero thickness throughout the entire simulation.

Since the bunch maintains zero longitudinal thickness, the potentials in Eqs. (8.13) and (8.14), and likewise their corresponding fields, only depend on the three variables, $(r_i, r_j, \theta_i - \theta_j)$. The doubly-infinite series in the field expressions were meshed over $(r_i, r_j, \theta_i - \theta_j)$ space, using a mesh of over 200,000 cells. In the radial direction, the mesh extended from $0.1a$ to $0.97a$. Figure 8-3 illustrates the mesh which was utilized for this simulation. We note that any macroparticle, which wandered outside of $0.97a$, were labeled lost to the wall. In a similar fashion, any macroparticle, which wandered inside

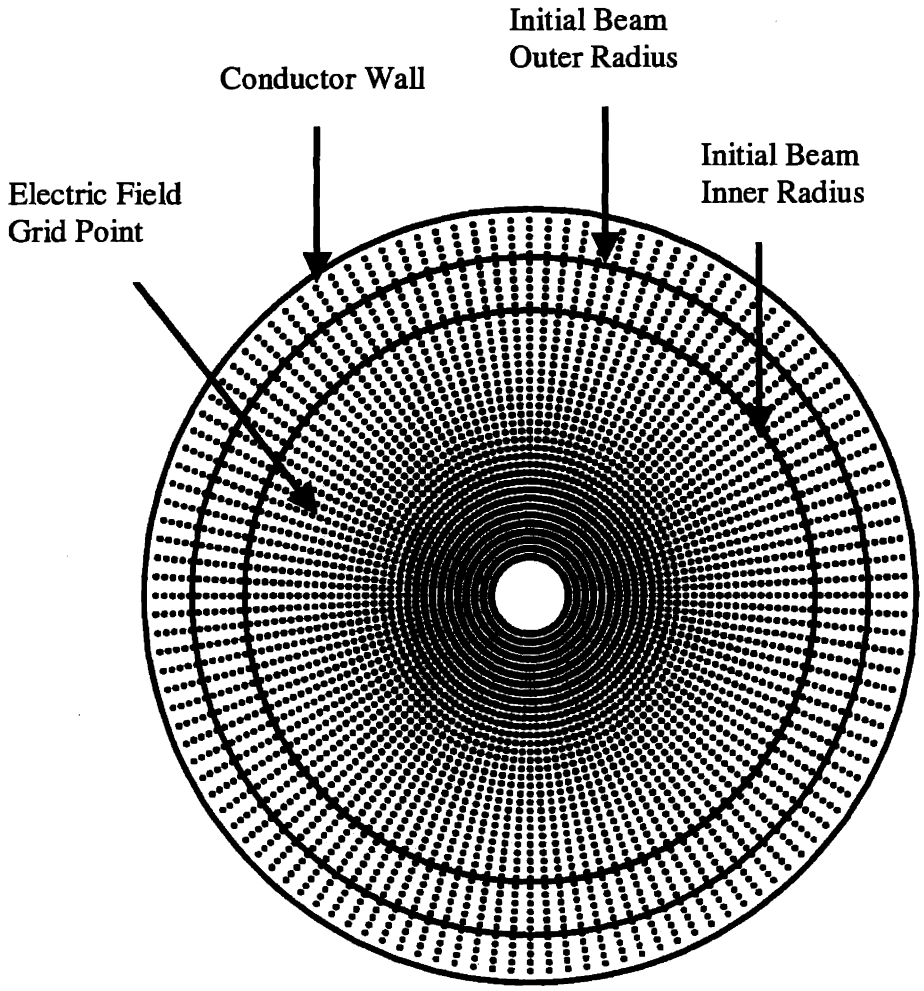

Figure 8-3: Diagram of the electric field grid points chosen for chosen for the LANL RKA simulation. The location of the conductor wall, as well as the initial inner and outer radii for the beam, are labeled in the diagram.

of $0.1a$, were considered lost. While it is not physically possible for a macroparticle to be lost inside of the conductor, it was necessary to cut the mesh off at a certain minimum radius for convergence reasons. We should note that the percentage of macroparticles lost inside of the conductor during the simulation was a few percent, which, as we will see, is considerably smaller than those lost the conductor wall.

We initialize 1000 macroparticles with the parameters corresponding to the LANL experiment which is listed in Table 7-1. The macroparticles are uniformly distributed in the azimuthal direction, and have a radial density distribution corresponding to quadratic density function in Eq. (6.16).

Choosing the correct initial angular and radial momenta is a difficult task, when modeling an actual experiment. In this simulation, we follow along with the fluid equilibrium formalism in the RBDB model. In particular, we initialize all of the particles with zero radial velocity. The angular velocity distribution is chosen to be the slow-wave fluid equilibrium distribution in Eq. (6.14). However, as seen from Table 7-1, the experimental value for the self-field parameter is greater than the critical value predicted from fluid equilibrium. According to Eq. (6.14), no angular rotation would exist since the argument under the square root would be negative.

We circumvent this problem by defining the initial angular velocity to be the fluid equibrium solution when it does exists, and zero otherwise. Figure 8-4 illustrates the initialization of the angular velocity for the macroparticles in the LANL RKA simulation.

Figure 8-5 shows the transverse evolution of the beam, along with the surrounding conducting wall. The time steps between each plot represents an increment of $0.1\gamma_b\omega_L^{-1}$ in time. The total simulation lasts for a time of $\gamma_b\omega_L^{-1}$, which corresponds to approximately 2 cm of beam propagation in the actual RKA device.

Qualitatively, we see that the beam undergos a few initial scattering events, which then lead to an enormous blowup of the beam, possibly due to a collective bunch effect. Approximately 16% of the beam, that is 160 macroparticles, where lost to the wall by the end of the simulation.

Figures 8-6 and 8-7 show the initial azimuthal velocity distribution and the beam evolution for a PFB3D simulation using system parameters identical to the LANL RKA experiment, except that the self-field parameter is reduced to

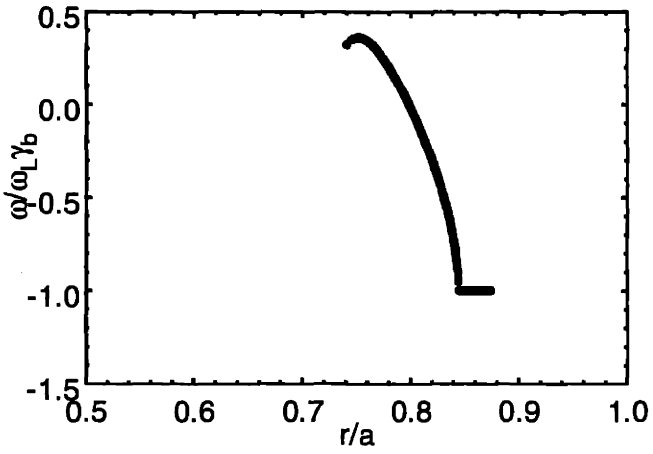

Figure 8-4: Initial angular velocity distribution chosen for the LANL RKA simulation. From the inner radius of the beam up to approximately $r/a = 0.84$, the beam is chosen to have the slow-wave solution of Eq. (6.14). When the solution does not exist, i.e., $r/a > 0.84$, we chose the angular velocity to be zero.

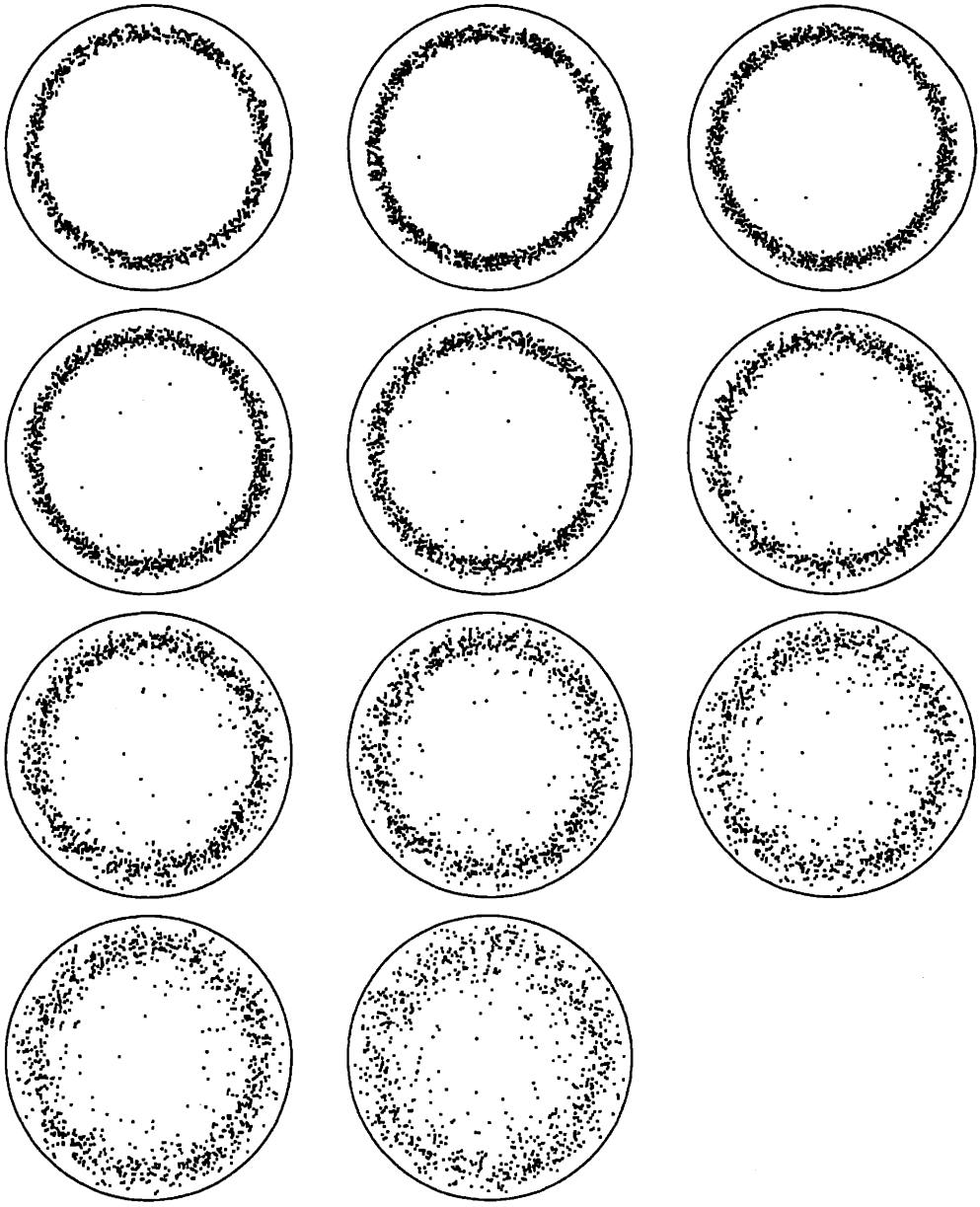

Figure 8-5: Preliminary results for the PFB3D simulation of the LANL RKA experiment using 1000 macroparticles. The first plot is the initial distribution, and each successive plot corresponds to an increment of time equal to $0.1\gamma_b\omega_L^{-1}$. Approximately 16% of the macroparticles were lost to the wall in the final plot corresponding to a time of $1.0\gamma_b\omega_L^{-1}$.

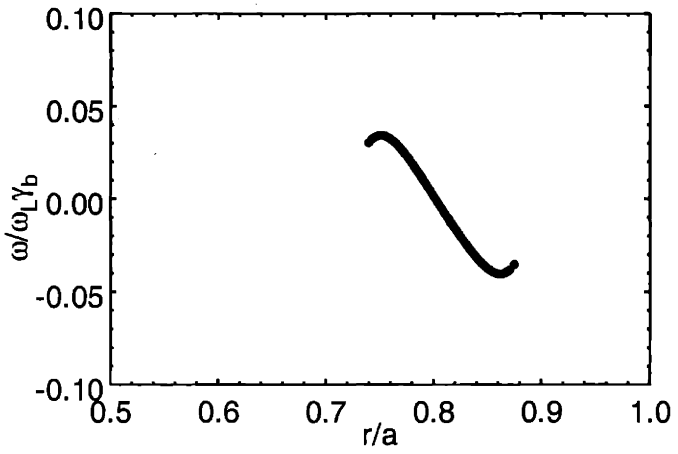

Figure 8-6: Initial angular velocity distribution chosen for the LANL RKA simulation with the self-field parameter reduced to $2\omega_p^2/\omega_c^2 = 0.001$.

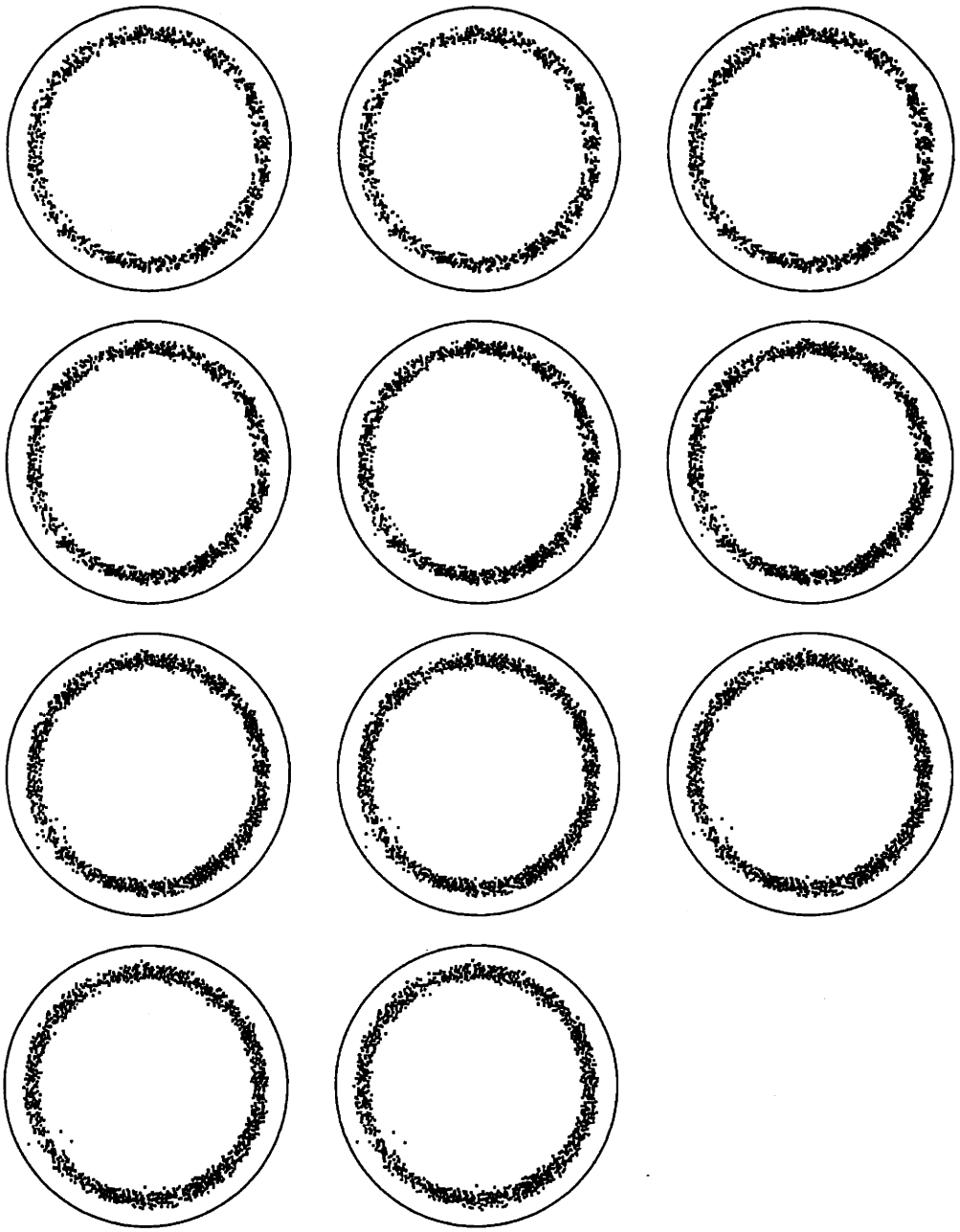

Figure 8-7: Preliminary results for the PFB3D simulation of the LANL RKA experiment with a reduced self-field parameter using 1000 macroparticles. The first plot is the initial distribution, and each successive plot corresponds to an increment of time equal to $0.1\gamma_b\omega_L^{-1}$. Approximately 0.1% of the macroparticles were lost to the wall in the final plot corresponding to a time of $1.0\gamma_b\omega_L^{-1}$.

$2\omega_p^2/\omega_c^2 = 0.001$. This is an order of magnitude lower than the critical self-field parameter $2\omega_p^2/\omega_c^2 = 0.0126$. The simulation shows only a negligible beam loss of 0.1% at the final time of $\gamma_b\omega_L^{-1}$, but the beam density distribution no significant qualitative change.

Similar PFB3D simulations have been performed for the LANL RKA model with self-field parameters reduced by approximately a factor of three (i.e. $2\omega_p^2/\omega_c^2 = 0.004$). In this regime, the RBDB model predicts that an equilibrium exists with no beam loss. However, the PFB3D code still shows moderate beam loss, though much less than for the case corresponding to the LANL RKA experiment. If the PFB3D results are reliable, then this implies that the equilibrium predicted by the RBDB model may not be stable to radial or azimuthal perturbations.

8.5 Discussion

We have outlined the development of the PFB3D code, which is based on the electrostatic Green's function technique. PFB3D simulates the dynamics of charged macroparticles interacting with each other in the presence of a cylindrical conductor wall. We presented preliminary results of a PFB3D simulation, which models the LANL RKA experiment (Fazio, *et al.*, 1994) discussed in Chapter 7.

There are a few issues, which should be addressed concerning the PFB3D code. One obvious issue is how to appropriately initialize the macroparticle distribution. As we mentioned in this Chapter, it not clear how to setup the initial radial and angular velocity distributions for the macroparticles, given that we did not know these distributions from experimental measurements.

The only possible option that we had was to try to form an equilibrium based on the RBDB model, with zero radial velocity and an angular flow distribution given by Eq. (6.14). However, since the RBDB model did not predict an equilibrium for the outside portion of the LANL RKA beam, this forced us to "clamp" the angular velocity to zero where Eq. (6.14) was not defined. The angular velocity distribution was not smooth, and, probably unphysical.

Another issue to discuss is the zero thickness of the beam bunch, which is similar to the RBDB model. The choice of this type of distribution makes the initialization and simulation much easier. Nevertheless, the fields which result due to macroparticle interactions will generally be higher than what would actually occur in an experiment. Hence, the 16% beam loss predicted by the PFB3D code for the LANL RKA experiment could be an overestimate.

The zero thickness bunch approximation did allow us to make some comparisons between the results of the PFB3D code and the RBDB equilibrium theory. One result, which we are still validating, is that the equilibria predicted by the RBDB model may not be stable to perturbations. We came to this conclusion based on the fact that we lowered the self-field parameter for the LANL RKA simulation to about a factor of three below the critical value predicted by the RBDB model, but significant beam-loss still occurred.

Another important issue in the PFB3D code is the number of macroparticles, M, used in the simulation. The LANL RKA simulation used M=1000 macroparticles. Various tests of the code suggests that M=1000 is probably the absolute minimum that should be used for obtaining a reliable simulation. PFB3D simulations using M=100, typically show macroparticle interactions which are far too gritty to seem reliable. The simulations with M=100 are generally dominated by local two body scattering events rather than the many-body collective effects with can come into play with M=1000 simulations.

One final item that we should address concerns the field mesh chosen for the simulation. The mesh shown in Figure 8-3 needs to be restructured to have higher density near the beam rather than in the center. The reason why we chose the mesh in Figure 8-3, which uses constant increment in the radial and azimuthal directions, is because it is the simplest possible mesh to generate. We could have also chosen to mesh the fields on a Cartesian grid rather than a cylindrical grid. This alleviates the problem of putting a "hole" in the grid at the center of the conductor. However, a Cartesian gridding would have to be done in a four-dimensional (x_i, y_i, x_j, y_j) space, and require a longer run time than the three-dimensional $(r_i, r_j, \theta_i - \theta_j)$ cylindrical gridding.

Chapter 9

Conclusions and Future Work

In this thesis, we have presented an analysis of bunched beams using electrostatic Green's functions. The Green's function technique allows one to self-consistently compute the electric and magnetic fields due to the charges inside of the bunch with conductors present. We have developed models of pencil bunched beams (NRCM and RCM) and annular bunched beams (RBDB), which all utilize the Green's function formalism. We then applied our models to actual bunched beam high-power microwave experiments using pencil and annular beams. In addition, we have developed a Green's function based code, called PFB3D, which self-consistently computes the interaction of charged periodic macroparticles in a cylindrical conductor.

In this Chapter, we will present concluding remarks pertaining to each of the models (NRCM, RCM, and RBDB) and the PFB3D code. We will also discuss possible areas for future work in modeling bunched beams with Green's functions.

9.1 NRCM Model

The Non-Relativistic Center-of-Mass model was our starting point for investigating bunched beams with Green's functions. Since the entire bunch was assumed to be a point charge, this model is one of the simplest possible models for a bunched particle beam in a cylindrical conductor with a constant magnetic focusing field present. Despite the simplicity of the model, the powerful bunched beam confinement criterion Eq. (3.31) emerges from the theory. This criterion is dramatically more stringent than the well-known Brillouin density limit (Brillouin, 1945) for unbunched beams.

The NRCM model has drawbacks, such as not incorporating the effect of a finite beam size to calculate the beam-wall interaction. For pencil thin beams, we can typically assume that the transverse size of the beam has little effect on the electric field acting on the center of mass. The longitudinal size of the bunch, however, may contribute significantly to the center of mass force.

One area of possible future work is to revise the NRCM model, such that the periodic bunches can be represented as rigid line segments (with lengths $\leq L$) instead of point charges. A new confinement criterion can be derived for the center of mass motion of the line segment bunches. We would expect that when the length of the bunch equals L, the Brillouin density limit would be recovered. Likewise, when the bunch length goes to zero, we should recover Eq. (3.31). This analysis would provide a confinement limit for a bunches of finite length, and may be applicable for predicting confinement limits on devices which are far from the perfect bunching limit.

The repulsive internal bunch forces, which are completely ignored in the NRCM model, can be very important. In Chapter 3, we tried to estimate the time-scale over which the bunch would be blowing up compared to the time-scale for which a bunch would hit the wall due to the beam-wall interaction. Our estimates showed that both effects would be of the same order in time-scale. Modeling the simultaneous effects of a finite bunch size, longitudinal and transverse, along with the effect of internal bunch forces is much too difficult to perform analytically. The best way to incorporate the fully 3-D effect of the internal forces and bunch size is to perform simulations on a code, such as PFB3D, which could be an area of future research.

9.2 RCM Model

The Relativistic Center-of-Mass model incorporated the relativistic motion of the bunched beam and the effect of a periodic magnetic focusing structure, along with the interaction of the beam and the wall. It allowed us to generalize the bunched beam confinement criterion of Eq. (3.31) to Eq. (4.13), which involves averaging over the longitudinal bunch motion in the periodic magnetic field.

In Chapter 5, we described how to apply the criterion in Eq. (4.13) to three PPM Klystron experiments at SLAC. The 50 MW XL-PPM (Sprehn, *et al.*, 1997; Sprehn, *et*

al., 2000),, the 75 MW XP (Sprehn, *et al.*, 1997; Sprehn, *et al.*, 2000),, and the Klystrino (Scheitrum, 2000; Scheitrum *et al.*, 2000) were all operating very close to the limit predicted by Eq. (4.13). Further, since the 75 MW XP was operating slightly above the limit in Eq. (4.13), we concluded that this was a possible explanation for the observance of significant beam loss and production of X-rays (Sprehn, *et al.*, 2000).

The RCM model has the same drawbacks as the NRCM model, namely the bunches are assumed to be point charges, and the internal space charge forces are ignored. However, this model has another problem, in that we assume a Lorentz transformation can made to the beam's rest frame can be made. In fact, HPM experiments may have significant energy spreads in the beam, which would imply that there is no electrostatic frame to which we can Lorentz transform.

A bunched beam with significant energy spread would have bunch particles interacting electromagnetically, not electrostatically. This fact seems to invalidate our usage of the electrostatic Green's function to compute the interactions of the particles. An electromagnetic Green's function, from which the electric and magnetic fields can be calculated, would seem more appropriate in predicting the interactions between particles. However, we believe that in the case of a tightly bunched beam with finite beam energy spread, the electrostatic interaction is the "zeroth" order effect in the overall electromagnetic interaction.

Like the problem of finite beam bunch size, it is probably not possibly to form a simple analytical model, like the RCM model, with finite beam spread using electromagnetic Green's functions. In order to understand the internal electromagnetic interactions between particles and the conductor, a significantly more advanced code than PFB3D would be necessary. One possible area of future work is to develop this code using electromagnetic Green's functions, however, such a task is enormously challenging. Nevertheless, it may prove to be enormously useful in modeling bunches in HPMs and accelerating structures.

9.3 RBDB Model

The Relativistic Bunched Disk Beam model incorporates the effect of the finite transverse bunch size, but maintains the zero longitudinal thickness approximation for the

beam bunch. This model is one step closer to a model of a three-dimensional bunch of finite size compared to the NRCM and the RCM. However, the simplification of zero longitudinal thickness gives the RBDB model the added power that it can be used as a numerical tool without having to perform a full 3-D simulation.

We restricted the model to only radially symmetric equilibrium transverse distributions, which would probably be the most important for an actual HPM experiment. An area of future work would be to extend the RBDB model to include transverse distributions that are not radially symmetric but have an azimuthal mode number. The self-consistent electric fields calculated from the electrostatic Green's function, in this case, would be more complicated, and numerical implementation of these new fields to find an azimuthally dependent equilibrium could be considerably more difficult.

We should note that the self-field parameter limit Eq. (6.14) predicted by the RBDB model, is only useful for determining if an equilibrium exists. A stability calculation for the RBDB model is a possible area of future work, which would probably show that the self-field parameter limit should be even lower for a stable equilibrium to exists. The self-field parameter limits predicted by the NRCM and the RCM models, were actually based on a stability calculation since the beam bunch is assumed to be at least slightly offset from the axis of the conductor.

Within the framework of the RBDB model, we developed the theory of the bunched rigid-rotor equilibrium. As mentioned before, this equilibrium has been of theoretical and experimental interest in recent years (see, for example, Davidson, 1990, Chap. 3). Possible future work could involve solving the general bunched rigid-rotor problem for arbitrary beam radius and periodicity, which would correspond to solving Eq. (6.23). This type of equilibrium may be applicable to bunched pencil beam devices. However, the fact that the transverse bunch size is always greater than the longitudinal bunch size in the RBDB model may make the estimate for the self-field parameter to small than the actual experiment.

In Chapter 7, we applied the RBDB model to three annular beam HPM experiments, 1.3 GHz LANL RKA (Fazio, *et al.*, 1994), 1.3 GHz AFRL RKO (Hendricks, *et al.*, 1996), and the 9.4 GHz UNM BWO (Hegeler, Grabowski, and Schamiloglu, 1998). We

discovered that the RKO and BWO experiments were operating well-below the self-field parameter limit in Eq. (6.13), while the RKA experiment was operating slightly above the limit. These results imply that the RKA experiment is not in equilibrium, and may be the reason for the observed beam loss (Fazio, *et al.*, 1994). The RBDB model can not account for the observed beam loss in the BWO experiment (Hegeler, Grabowski, and Schamiloglu, 1998), but is in agreement with the successful operation of the RKO experiment (Hendricks, *et al.*, 1996). We looked specifically at the parameters for one experimental shot, Figure 7-2, for the LANL RKA. Since the LANL RKA experiment was operating close to the equilibrium limit during this shot, it is worth analyzing more shots of data.

9.4 PFB3D Code

In Chapter 8, we described the development of the Periodic Focused Beam in 3-D code, which can simulate the dynamics of charged macroparticles in a perfectly conducting cylinder using electrostatic Green's functions. The PFB3D code, in its full version, would enable the user to model relativistic bunches of charge of arbitrary size and shape, and includes the self-consistent electrostatic forces between the particles in the presence of the wall.

There are several improvements that should be made to the code. One of which is that a Windows based user interface should be added to make the operation of the code simpler. The interface would contain options for plotting the beam cross-section, as well as the beam phase space. Currently, the PFB3D code is operating from an MS-DOS command.

The code is currently running in a 2-½ configuration, where the bunches have zero thickness. We chose this configuration in order to make the preliminary results of the code and the electric field mesh simpler, and also to check the stability of the RBDB model. However, another improvement of the PFB3D code would be to modify the electric field mesh for modeling full 3-D bunches. This would require extending the mesher to four dimensions, $(r_i, r_j, \theta_i - \theta_j, z_i - z_j)$, instead of just three dimensions, $(r_i, r_j, \theta_i - \theta_j)$.

Another possible improvement in the PFB3D code would be to modify the fixed time step Fourth Order Runge-Kutta integrator to a new scheme, which would be more relevant to many-particle dynamics. One alternative integration scheme would be a variable time-step Runge Kutta method, which would estimate the best time step by intermittently testing the dynamics of the particles. Optimized versions of this method could prove to be faster than the current fixed time step method.

We presented the preliminary results of a simulation for the LANL RKA experiment. We found that the beam was unstable, and a large amount of beam, 16%, was lost to the wall after only 2 cm of beam propagation. This is much larger than the beam loss amount predicted by the RBDB model, which is approximately 5%. If the PFB3D code results are correct, then this result may imply that the RBDB equilibrium was not stable for the LANL RKA parameters. The results of the PFB3D code are encouraging, but more tests and improvements are necessary to have confidence in its validity.

Bibliography

Allen, C. K. and Reiser, M., 1997, Phys. Rev. E **55**, p. 7591.

Arfken, G. B., and Weber, H. J., 1995, *Mathematical Methods for Physicists*, 4th Ed., (Academic Press, San Diego).

Barnard, J. J. and Lund, S. M., 1997, in *Proceedings of the Particle Accelerator Conference*, edited by M. Comyn (Institute of Electrical and Electronics Engineers, Piscataway, NJ), p. 1929.

Barton, G., 1995, *Elements of Green's Function and Propagation*, (Oxford University Press, New York, NY)

Benford, J. and Swegle, J., 1992, *High Power Microwaves* (Artech, Boston, MA).

Brahme, A. and Lind, B. K., 2001, in *International Nuclear Physics Conference*, edited by E. Norman, *et al.*, AIP Proc. 610, (American Institute of Physics, Melville, New York), p. 315.

Brinkmann, R., 1999, in *Proceedings of the Particle Accelerator Conference*, edited by A. Luccio and W. Mackay (Institute of Electrical and Electronics Engineers, Piscataway, NJ), p. 16.

Brillouin, L., 1945, Phys. Rev. **67**, 260.

Chacon-Golcher, E., Baca, D., and Kwan, J. W., 2002, Rev. Sci. Instrum. **73**, 1036.

Chao, A. W., 1993, *Physics of Collective Beam Instabilities in High Energy Accelerators* (John Wiley & Sons, New York, NY).

Chen, C. and Pakter, R., 1999, in *Intense Microwave Pulses VI*, SPIE Proc. 3702, edited by H. E. Brandt (SPIE, Bellingham, WA), p. 21.

Chen, C. and Pakter, R., 2000, Phys. Plasmas **5**, 2203.

Chin, Y. H., 2001, *Proceedings of the Particle Accelerator Conference*, edited by P. Lucas and S. Webber (Institute of Electrical and Electronics Engineers, Piscataway, NJ), p. 415.

Davidson, R. C., 1990, *Physics of Nonneutral Plasmas*, (Addison-Wesley, Reading).

Dearnaley, G., 1988, in *Ion Implantation and Plasma Assisted Processes*, edited by R. F. Hochman, H. Solnick-Legg, and K. O. Legg, (ASM International, Metals Park, Ohio), p. 63.

Dougall, J., 1900, in *Proceedings of the Edinburgh Mathematical Society*, Vol. 18, edited by (Williams & Norgate, Edinburgh), p. 33.

Douglas, D. *et al.*, 2001, in *Proceedings of the Particle Accelerator Conference*, edited by P. W. Lucas and S. Webber (Institute of Electrical and Electronics Engineers, Piscataway, NJ), p. 2644.

Driscoll, C. F., Malmberg, J. H., Fine, K. S., 1988, Phys. Rev. Lett. **60**, 1290.

Dugan, G., 1999, in *Proceedings of the Particle Accelerator Conference*, edited by A. Luccio and W. Mackay (Institute of Electrical and Electronics Engineers, Piscataway, NJ), p. 48.

Evans, L. R., 1999, in *Proceedings of the Particle Accelerator Conference*, edited by A. Luccio and W. Mackay (Institute of Electrical and Electronics Engineers, Piscataway, NJ), p. 21.

Fazio, M. V., Haynes, W. B., Carlsten, B. E., and Stringfield, R. M., 1994, IEEE Trans. Plasma Sci. **22**, 740.

Gilmour, Jr., A. S., 1986, *Microwave Tubes*, (Artech House, Dedham, MA).

Gluckstern, R. L., Fedotov, A. V., Kurennoy, S., and Ryne, R., 1998, Phys. Rev. E, **58**, 4977.

Gold, S. H. and Nusinovich, G. S., 1997, Rev. Sci. Instrum. **68**, p. 3945.

Gradshteyn, I. S. and Ryzhik, I. M., 1994, *Table of Integrals, Series, and Products*, 5th Ed. (Academic, London).

Gray, A., and Mathews, G. B., 1952, *A Treatise on Bessel Functions and Their Applications to Physics*, (Macmillan and Co., London).

Griffiths, D. J., 1989, *Introduction to Electrodynamics*, 2nd Ed., (Prentice Hall, Upper Saddle River, NJ)

Haberer, T., 2001, in International Nuclear Physics Conference, edited by E. Norman, *et al.*, AIP Proc. 610, (American Institute of Physics, Melville, New York), p. 157.

Hegeler, F., Grabowski, C., and Schamiloglu, E., 1998, IEEE Trans. Plasma Sci. **26**, 275.

Hendricks, K. J., *et al.*, 1998, IEEE Trans. Plasma Sci., **26**, 320.

Hess, M. and Chen, C., 2000, Phys. Plasmas **7**, 5206.

Hess, M. and Chen, C., 2002(a), Phys. Lett. A, (in press).

Hess, M. and Chen, C., 2002(b), Phys. Plasmas **9**, 1422.

Holmes, S. D., 1999, in *Proceedings of the Particle Accelerator Conference*, edited by A. Luccio and W. Mackay (Institute of Electrical and Electronics Engineers, Piscataway, NJ), p. 43.

Humphries, Jr., S., 1986, *Principles of Charged Particle Acceleration*, (John Wiley & Sons, New York, NY).

Humphries, Jr., S., 1990, *Charge Particle Beams*, (John Wiley & Sons, New York, NY).

Jackson, J. D., 1975, *Classical Electrodynamics*, 2nd Ed., (John Wiley & Sons, New York, NY).

Kaesmaier, R. and Loschner H., 2000, in *Emerging Lithographic Technologies IV*, SPIE Proc. 3997, edited by E. A. Dobisz (SPIE, Bellingham, WA), p. 19.

Kapchinsky, I. M. and Vladimirsky, V. V., 1959, in *Proceedings of the International Conference on High-Energy Accelerators and Instrumentation*, (CERN Scientific Information Service, Geneva), p. 274.

Kyhl, R. L. and Webster, H. F., 1956, IRE Trans. Electron Devices, **3**, 172.

Liu, F., *et al.*, 1998, Rev. Sci. Instrum. **69**, 819.

Livingston, M. S. and Blewett, J. P., 1962, *Particle Accelerators*, (McGraw-Hill, New York, NY).

Mangulis, V. , 1965, *Handbook of Series for Scientists and Engineers*, (Academic, New York, NY).

Nastasi, M., Moller, W., and Ensinger, W., 2000, in *Handbook of Plasma Immersion Ion Implantation and Deposition*, edited by A. Anders (John Wiley & Sons, New York), Chap. 3.

Neil, G. R. *et al.*, 2000, Phys. Rev. Lett. **84**, 662.

Pakter, R. and Chen, C. 2000, IEEE Trans. Plasma Sci. **28**, 502.

Pfeiffer, H. C., 2000, in *Emerging Lithographic Technologies IV*, SPIE Proc. 3997, edited by E. A. Dobisz (SPIE, Bellingham, WA), p. 206.

Pierce, J. R., 1950, *Traveling-Wave Tubes*, (Van Nostrand, New York).

Reitz, J. R., Milford, F. J., and Christy, R. W., 1993, *Foundations of Electromagnetic Theory*, 4th Ed., (Addison-Wesley, Reading).

Raubenheimer, T. O., 1999, in *Proceedings of the Particle Accelerator Conference*, edited by A. Luccio and W. Mackay (Institute of Electrical and Electronics Engineers, Piscataway, NJ), p. 240.

Reiser, M., 1994, *Theory and Design of Charged Particle Beams*, (John Wiley & Sons, New York, NY).

Roberson, C. W. and Sprangle, P., 1989, Phys. Fluids B **1**, 3.

Sacherer, F. J., 1971, IEEE Trans. Nucl. Sci. **NS-18**, 1105.

Schachter, L., 1996, *Beam-Wave Interaction in Periodic and Quasi-Periodic Structures*, (Springer-Verlag, Berlin).

Scheitrum, G., 2000, private communication.

Scheitrum, G. *et al.*, 2000, in *Abstracts: International Vacuum Electronics Conference 2000*, (Institute of Electrical and Electronics Engineers, Piscataway, NJ), Session 1.5.

Schiffler, D., Nation, J. A., Schachter, L., Ivers, J. D., and Kerslick, G. S., 1991, J. Appl. Phys. **70**, 106.

Schwarz, H. R., 1988, *Finite Element Methods*, (Academic Press, San Diego).

Shampine, L. F., Allen, Jr., R. C., Pruess, S., 1997, *Fundamentals of Numerical Computing*, (John Wiley & Sons, New York, NY).

Sprehn, D., Caryotakis, G., Jongewaard, E., and Phillips, R. M., 1997, in *Proceedings of 19th International Linac Conference*, Argonne National Laboratory Report ANL-98/28.

Sprehn, D., Caryotakis, G., Jongewaard, E., Phillips, R. M., and Vlieks, A., 2000 in *Intense Microwave Pulses VII*, SPIE Proc. 4301, edited by H. E. Brandt (SPIE, Bellingham, WA), p. 132.

Tenenbaum, P, 2000, Int. Jour. Mod. Phys. A **15** p. 2461

Wang, P., *et al.*, 1999, Appl. Phys. Lett. **75**, 2506.

Watson, G. N., 1980, *A Treatise on the Theory of Bessel Functions*, 2nd Ed., (Cambridge University, Cambridge).

Appendix A

Calculation of the Electrostatic Self-Field for the NRCM Model

When calculating the self-field force, we may assume that $\theta' = \hat{z}' = 0$, without loss of generality, and express $\mathbf{r}' = \frac{L}{2\pi}\hat{r}'\hat{\mathbf{e}}_{x'}$ and $\mathbf{r}_s = \frac{L\alpha\cos\theta}{2\pi}\hat{\mathbf{e}}_x + \frac{L\alpha\sin\theta}{2\pi}\hat{\mathbf{e}}_y + \frac{L\hat{z}}{2\pi}\hat{\mathbf{e}}_z$. Since $E_z(\mathbf{r}') = E_\theta(\mathbf{r}') = 0$ by the symmetries of the system in the longitudinal and azimuthal directions, we need only consider the force along the direction of $\hat{\mathbf{e}}_{x'} = \hat{\mathbf{e}}_{y'}$. Making use of the expressions,

$$\frac{(\mathbf{r}'-\mathbf{r}_s)\cdot\hat{\mathbf{e}}_x}{|\mathbf{r}'-\mathbf{r}_s|^3} = -\left(\frac{2\pi}{\alpha L}\right)^2 \frac{\cos\theta - \dfrac{\hat{r}'}{\alpha}}{\left(1+\dfrac{\hat{r}'^2}{\alpha^2}+\dfrac{\hat{z}^2}{\alpha^2}-2\dfrac{\hat{r}'}{\alpha}\cos\theta\right)^{3/2}},$$

and $dS = a\,dz\,d\theta = \left(\frac{L}{2\pi}\right)^2 \alpha\,d\hat{z}\,d\theta$, we may express Eq. (3.9) as

$$E^{self} = -4\int_0^\infty d\eta \int_0^\pi \frac{(\cos\theta - \beta)\sigma\,d\theta}{(1+\beta^2+\eta^2-2\beta\cos\theta)^{3/2}} \qquad \text{(A1)}$$

where $\eta = \hat{z}/\alpha$ and $\beta = \hat{r}'/\alpha$, and we have also used the longitudinal and azimuthal symmetries to change the limits of integration.

Substituting Eq. (3.7) into Eq. (A1), we find that the self-electric field produced by the 2-D induced surface charge at the line charge is

$$E_{2D}^{self} = \frac{4(1-\beta^2)\lambda}{L\alpha}\int_0^{\pi}\frac{(\cos\theta-\beta)d\theta}{(1+\beta^2-2\beta\cos\theta)^{3/2}}\int_0^{\infty}\frac{d\eta}{(1+\beta^2+\eta^2-2\beta\cos\theta)^{3/2}}$$
$$= \frac{4\pi\lambda}{L}\frac{\hat{r}'}{\alpha^2-\hat{r}'^2} \qquad \text{(A2)}$$

which is identical to Eq. (3.10). This result can also be obtained easily using the method of images (Barton, 1995, pp. 415-416).

Of course, the first term in Eq. (3.11) corresponds to the 2-D component, which we have just derived. Substituting Eq. (3.8) into Eq. (A1), we can express the self-electric field produced by the 3-D induced surface charge at the point charge as,

$$E_{3D}^{self} = \frac{4\pi Q}{L}\frac{\hat{r}'}{\alpha^2-\hat{r}'^2} + \frac{8Q}{\alpha L^2}\sum_{n=1}^{\infty}\frac{I_0(n\hat{r}')\Theta_{n0}}{I_0(n\alpha)} + \frac{16Q}{\alpha L^2}\sum_{n=1}^{\infty}\sum_{l=1}^{\infty}\frac{I_l(n\hat{r}')\Theta_{nl}}{I_l(n\alpha)} \qquad \text{(A3)}$$

where

$$\Theta_{nl} = \int_0^{\infty}\int_0^{\pi}\frac{\cos(n\alpha\eta)\cos(l\theta)(\cos\theta-\beta)d\eta d\theta}{(1+\beta^2+\eta^2-2\beta\cos\theta)^{3/2}}$$
$$= \frac{\partial}{\partial\beta}\int_0^{\infty}\int_0^{\pi}\frac{\cos(n\alpha\eta)\cos(l\theta)d\eta d\theta}{(1+\beta^2+\eta^2-2\beta\cos\theta)^{1/2}}$$
$$= \frac{\partial}{\partial\beta}\int_0^{\infty}\int_0^{\pi}K_0\left(n\alpha\sqrt{1+\beta^2-2\beta\cos\theta}\right)\cos(l\theta)d\theta$$
$$= \frac{\partial}{\partial\beta}\int_0^{\infty}\int_0^{\pi}\left[I_0(n\alpha\beta)K_0(n\alpha)+2\sum_{p=1}^{\infty}I_p(n\alpha\beta)K_p(n\alpha)\cos(p\theta)\right]\cos(l\theta)d\theta$$
$$= \pi K_l(n\alpha)\frac{\partial}{\partial\beta}I_l(n\alpha\beta)$$
$$= \pi K_l(n\alpha)I_l'(n\hat{r}') \qquad \text{(A4)}$$

In the third step in Eq. (A4), we made use of the relation (Gradshteyn and Ryzhik, 1994, p. 464),

$$\int_0^{\infty}\frac{\cos(ax)dx}{\sqrt{x^2+b^2}} = K_0(ab),$$

while in step 4 we used the formula (Gray and Mathews, 1952, p. 74),

$$K_0\left(\sqrt{a^2+b^2-2ab\cos\theta}\right) = I_0(a)K_0(b)+2\sum_{p=1}^{\infty}I_p(a)K_p(b)\cos(p\theta), \quad 0\le a\le b.$$

Substituting Eq. (A4) into Eq. (A3) yields Eq. (3.11).

Appendix B

Derivation of the Self-Fields for the RBDB Model

The equilibrium self-electric and self-magnetic fields, $E^{self}(r)\hat{\mathbf{e}}_r$ and $B^{self}(r)\hat{\mathbf{e}}_\theta$, are found by calculating them in the rest frame of the beam and then performing a Lorentz transformation back to the laboratory frame. The advantage of this approach is that in the beam rest frame, the self-magnetic field is negligibly small. Therefore, it is sufficient to calculate only the self-electric field of the beam including the full effect of induced charge on the conducting cylinder. Indeed, by introducing the scalar and vector potentials, $\phi^{self}(r)$ and $A^{self}(r)\hat{\mathbf{e}}_z$ in the laboratory frame, and correspondingly $\phi^{self}_{rest}(r)$ and $\mathbf{A}^{self}_{rest}(r)$ in the rest frame, it is readily shown from the Lorentz transformation that

$$\phi^{self}(r) \cong \gamma_b \phi^{self}_{rest}(r) \tag{B1}$$

and

$$A^{self}(r)\hat{\mathbf{e}}_z \cong \gamma_b \beta_b \phi^{self}_{rest}(r)\hat{\mathbf{e}}_z \tag{B2}$$

where $\beta_b = V_z/c$ and use has been made of the approximation $\mathbf{A}^{self}_{rest}(r) = 0$. From the definitions for the scalar and vector potentials, the self-electric and self-magnetic fields are given by

$$\mathbf{E}^{self}(r) = -\hat{\mathbf{e}}_r \gamma_b \frac{\partial \phi^{self}_{rest}(r)}{\partial r} = \gamma_b E^{self}_{rest}(r)\hat{\mathbf{e}}_r \tag{B3}$$

$$\mathbf{B}^{self}(r) = -\hat{\mathbf{e}}_\theta \gamma_b \beta_b \frac{\partial \phi^{self}_{rest}(r)}{\partial r} = -\gamma_b \beta_b E^{self}_{rest}(r)\hat{\mathbf{e}}_\theta \tag{B4}$$

The electrostatic Green's function technique, which is developed in Chapter 2, is used to calculate the scalar potential $\phi_{rest}^{self}(r)$ and self-electric field $E_{rest}^{self}(r)\hat{\mathbf{e}}_r$ in the rest frame of the beam. By utilizing the electrostatic Green's function Eq. (2.16), the electrostatic potential relation Eq. (2.7), and the density distribution defined by Eq. (6.2), we find that the electrostatic potential in the plane of the beam, i.e., $\phi_{rest}^{self}(r) = \phi_{rest}^{self}(\mathbf{r})\big|_{z=z'=0}$, can be expressed as

$$\phi_{rest}^{self}(r) = -N_b e \lim_{\Delta r \to 0} \int_0^{2\pi} d\theta' \left[\int_0^{r-\Delta r} dr' r' \sigma(r') \tilde{\phi}(\mathbf{r};\mathbf{r}') + \int_{r+\Delta r}^{a} dr' r' \sigma(r') \tilde{\phi}(\mathbf{r};\mathbf{r}') \right], \tag{B5}$$

where

$$\begin{aligned} \tilde{\phi}(\mathbf{r};\mathbf{r}') = & \frac{1}{L_{rest}} ln\left[\frac{a^2 + r_>^2 r_<^2 / a^2 - 2 r_> r_< cos[\theta - \theta']}{r_>^2 + r_<^2 - 2 r_> r_< cos[\theta - \theta']} \right] \\ & + \frac{4}{L_{rest}} \sum_{l=-\infty}^{\infty} \sum_{k=1}^{\infty} cos[l(\theta - \theta')] \frac{I_l(k\hat{r}_<)}{I_l(k\alpha)} [I_l(k\alpha) K_l(k\hat{r}_>) - K_l(k\alpha) I_l(k\hat{r}_>)] \end{aligned} \tag{B6}$$

In Eq. (B5), the radial integral must be split into two parts, namely $r' < r$ and $r' > r$, in order to ensure convergence of $\phi_{rest}^{self}(r)$. In mathematical formalism, $\phi_{rest}^{self}(r)$ is obtained by taking the principal integral of $r'\sigma(r')\tilde{\phi}(\mathbf{r};\mathbf{r}')$ in the radial direction. Using the azimuthal symmetry assumption and the relation, $\int_0^{2\pi} d\theta' \ln\left[x^2 + y^2 - 2xy\cos(\theta - \theta')\right] = 4\pi \ln x$ for $0 \le y < x$ (Gradshteyn and Ryzhik, 1994, p. 560), we find,

$$\phi_{rest}^{self}(r) = -N_b e \lim_{\Delta r \to 0} \left[\int_0^{r-\Delta r} dr' r' \sigma(r') F(r;r') + \int_{r+\Delta r}^{a} dr' r' \sigma(r') F(r;r') \right], \tag{B7}$$

where

$$F(r;r') = \frac{4\pi}{L_{rest}} \ln\left[\frac{a}{r_>}\right] + \frac{8\pi}{L_{rest}} \sum_{k=1}^{\infty} \frac{I_0(k\hat{r}_<)}{I_0(k\alpha)} [I_0(k\alpha) K_0(k\hat{r}_>) - K_0(k\alpha) I_0(k\hat{r}_>)]. \tag{B8}$$

Notice that all of the azimuthally dependent terms ($l > 0$) vanished in Eq. (B8), since we assumed that $n(\mathbf{r}')$ is radially symmetric. The higher-order l terms would appear if we assumed that $n(\mathbf{r}')$ varied azimuthally. Hence,

$$E^{self}(r)=-\frac{4\pi N_b\gamma_b e}{L_{rest}}\left[\frac{1}{r}\int_0^r dr'r'\sigma(r')+\frac{4\pi}{L_{rest}}\sum_{k=1}^{\infty}\frac{kI_1(k\hat{r})K_0(k\alpha)}{I_0(k\alpha)}\int_0^a dr'r'\sigma(r')I_0(k\hat{r}')\right.$$
$$\left.+\frac{4\pi}{L_{rest}}\lim_{\Delta r\to 0}\left\{\sum_{k=1}^{\infty}kK_1(k\hat{r})\int_0^{r-\Delta r}dr'r'\sigma(r')I_0(k\hat{r}')-\sum_{k=1}^{\infty}kI_1(k\hat{r})\int_{r+\Delta r}^{a}dr'r'\sigma(r')K_0(k\hat{r}')\right\}\right] \tag{B9}$$

Note that the first term on the right hand side of Eq. (B9) represents the electric field due to a longitudinally uniform beam and the other three terms are the corrections due to the longitudinal bunching of the beam. Utilizing the density expansion given in Eq. (6.3), the following Bessel function integrals (see, for example, Watson, 1980, p. 132-134),

$$\int_0^1 dxxJ_0(yx)=y^{-1}J_1(y),$$

$$\int_0^1 dxxJ_0(yx)I_0(zx)=\left(y^2+z^2\right)^{-1}\left[zJ_0(y)I_1(z)+yJ_1(y)I_0(z)\right],$$

$$\int_w^1 dxxJ_0(yx)K_0(zx)=\left(y^2+z^2\right)^{-1}\left[yJ_1(y)K_0(z)-zJ_0(y)K_1(z)\right.$$
$$\left.+zwJ_0(yw)K_1(zw)-ywJ_1(yw)K_0(zw)\right], \tag{B10}$$

and the Wronskian relation, $I_0(x)K_1(x)+I_1(x)K_0(x)=1/x$, we obtain the following form for the electric self-field

$$E^{self}(r)=-\frac{4\pi N_b ea}{L}\left[\sum_{m=1}^{\infty}\frac{\sigma_m}{j_{0m}}J_1(j_{0m}r/a)+2\sum_{m=1}^{\infty}\sum_{k=1}^{\infty}\frac{\sigma_m j_{0m}}{j_{0m}^2+k^2\alpha^2}J_1(j_{0m}r/a)\right]. \tag{B11}$$

A further simplification is made by employing the relation (Mangulis, 1965, p. 26) $\sum_{k=1}^{\infty}\left(y^2+k^2x^2\right)^{-1}=\pi\coth(\pi y/x)/2yx-1/2y^2$, which yields

$$E^{self}(r)=-2\pi N_b e\gamma_b\sum_{m=1}^{\infty}\sigma_m J_1(j_{0m}r/a)coth(j_{0m}\gamma_b L/2a). \tag{B12}$$

This concludes the derivation of Eq. (6.7) and Eq. (6.8) in Section 6-2.